Università degli Studi di Firenze
Scuola di Ingegneria
DIEF - Department of Industrial Engineering of Florence

PhD School: *Energetica e Tecnologie Industriali ed Ambientali Innovative*
Scientific Area: ING-IND/08 - *Macchine a Fluido*

High-fidelity prediction of metal temperature in gas turbine combustors using a loosely coupled multiphysics approach

PhD Candidate: Ing. Davide Bertini

Tutor: Prof. Ing. Bruno Facchini
Academic Supervisor: Dr. Ing. Antonio Andreini
PhD School Coordinator: Prof. Ing. Maurizio De Lucia

XXXI PhD School Cycle - 2015-2018

To my parents,
as who I am today is the result of their love.

Someone's sitting in the shade today because
someone planted a tree a long time ago.
(Warren Buffet)

Acknowledgements

Finalmente è giunto il momento di fermarsi un attimo per fare un bilancio degli ultimi tre anni senza pensare a cosa succederà domani. Ricordarmi chi ero e guardare chi sono diventato può aiutare molto in questo senso ma non può prescindere da alcuni doverosi ringraziamenti.
Il primo e sincero ringraziamento va a chi ha messo a disposizione le risorse per consentirmi di raggiungere questo traguardo, ovvero il Prof. Facchini. La naturalezza con cui parla delle turbine a gas è stato decisivo per farmi appassionare a queste tematiche. Il gruppo di colleghi (ma preferisco definirlo di amici) che ha creato è sicuramente frutto del suo impegno nella didattica.
Se c'è una persona a cui devo essere riconoscente per avermi indirizzato, nell'ormai lontano 2014, verso quello che poi è diventato il tema specifico del mio dottorato è senza ombra di dubbio Antonio. La sua esperienza è stata utilissima nel corso di questi anni ed i confronti con lui sono stati spesso fondamentali per superare le difficoltà e crescere professionalmente.
Se ci sarà qualcosa di cui avrò nostalgia negli anni a venire sarà sicuramente lavorare in gruppo con chi più di ogni altro è stato un amico e compagno di "avventure" ancora prima di un collega. Mi sto riferendo ovviamente a Lorenzo e Stefano. I ricordi sono veramente tanti e tutti belli, la loro compagnia ha permesso di affrontare con il giusto spirito ogni divergenza, SIGSEV e scadenza per il Turbo Expo. Con la passione contagiosa che mettono in quello che fanno sono stati un continuo esempio da imitare ed anche per questo motivo c'è molto di loro in questa tesi.
Per elencare le qualità di Lorenzo ci vorrebbe un capitolo dedicato della tesi. La sua conoscenza e curiosità, nonchè la serietà, la capacità critica ed organizzativa che mette in quello che fa sono assolutamente invidiabili. Il confronto quotidiano e il suo aiuto sono risulati fondamentali per la qualità del lavoro. Ma l'aiuto di Lorenzo va ben oltre quello tecnico perchè nelle difficoltà degli ultimi mesi è stato una valida spalla.
Per quanto riguarda Stefano mi sento onorato di essere stato il suo "primo"

tesista. Lavorando in team con lui ho avuto modo di apprezzare la sua capacità nell'andare sempre oltre il semplice risultato. Anche dalla Francia non mi ha mai fatto mancare il suo supporto morale.
A loro due poi si aggiungono ovviamente tutti gli altri ragazzi passati dall'HTC Group (e non solo) che voglio almeno nominare, ovvero Ale, LoreW, TommyF, Ema, Leopoldo, Sabri, Dani, LoreC, Gama, Domi, Asif, Palo, Simo, Matte, Carlo, Pier, Langa, TommyD e Francesco. Anche grazie a loro questi tre anni sono passati senza diventare un peso.
Uscendo dalla sfera lavorativa, anche qui i ringraziamenti non mancano. Il più doveroso e importante è indubbiamente quello alla mia famiglia. Il loro supporto, soprattutto nei momenti di difficoltà, non è mai mancato. I risultati che ho ottenuto sono anche frutto della serenità con cui mi hanno permesso di affrontare il mio percorso di studi e di questo gli sarò sempre grato.
Ci sono stati ovviamente, come deve essere, anche momenti di svago in cui è venuto fuori il "Pomino 2.0". Il merito di questi momenti, che porterò sempre con me, va al Giuse, il Poggi, il Borso, il Fabbri, Elena ed il Samba. Grazie a tutti per avermi ricordato che non esiste solo lo studio ed il lavoro.
Ad una persona per me speciale però voglio dedicare quest'ultimo paragrafo, ovvero Federica, la quale mi ha sempre ribadito quanto valessi e che con il suo affetto e sorriso ha reso gli ultimi due anni unici. Se non fossi rimasto a Firenze non l'avrei mai conosciuta ed è quindi la ragione principale per la quale non potrò mai vedere il dottorato un traguardo come tutti gli altri.

Abstract

Aeroengine industry is being largely affected by the mid- and long-term targets of civil aviation, that is searching for increasingly efficient low-emission engines and new opportunities as in the segment of small aircraft. The dynamically evolving market requires prompt solutions for the combustor that cannot be easily provided by experiments because of technical issues and expensive campaigns. On the other hand, the progressive developments in the field of massively parallel computing is making Computational Fluid Dynamics the most effective tool for a deep insight of combustion chambers. Indeed, high-fidelity investigations on this component is a multiphysics problem requiring to model the interactions between turbulence, combustion, radiation and heat transfer. Thermal design is a key task in the development loop of novel combustors, being stressed by lower coolant availability and higher power density. For this purpose, CFD-based models are required to properly account for the 3-D heat load distribution. Nevertheless, the limits of standard RANS approaches in accurately modelling highly-turbulent reacting flow is well-known and nowadays scale-resolving methods, as Large-Eddy Simulation (LES), Detached Eddy Simulation (DES) and Scale Adaptive Simulation (SAS), are the most promising ones; the latter, in particular, is emerged as a valid trade-off for industrial applications.
In the present work a multiphysics tool, called U-THERM3D, is proposed as potential approach for the prediction of metal temperature in the context of scale-resolving simulations. The tool is validated on predictable solutions and applied to two burners, the DLR model aero-engine combustor and the LEMCOTEC combustor. The former is a laboratory sooting flame simulated using LES and the focus is on the tool capabilities in modelling the involved interacting phenomena. The latter is an effusion cooled lean-burn aeroengine combustor investigated from different perspectives using SAS to predict exit profile temperature, emissions and metal temperature. To the author's knowledge no works can be found in

literature on multiphysics simulations of lean burn combustors relying on Scale Adaptive Simulation. For this reason the present work aims to be a reference for high-fidelity final design as well as a starting point for future activities. The results in both the burners are compared against steady THERM3D simulations and experiments emphasizing the detrimental effects of the swirling flow on the wall temperature, that acts increasing the heat transfer coefficient and reducing the film cooling coverage. The improved prediction of metal temperature obtained by U-THERM3D shows the potential of this tool as a framework for the high-fidelity design of gas turbine combustors. Obviously, the accuracy of the coupled simulation can benefit from the improvement in the different involved models and further research efforts should be focused on this task.

Contents

List of Figures

List of Tables

Nomenclature

A	Area	$[m^2]$
B_M	Mass Spalding number	$[-]$
c	Progress Variable	$[-]$
D	Diffusivity	$[m^2\ s^{-1}]$
d	Droplet diameter	$[m]$
f	Fanning friction factor	$[-]$
HTC	Heat transfer coefficient	$[W\ m^{-2}\ K^{-1}]$
h	Coupling relaxation parameter	$[W\ m^{-2} K^{-1}]$
k	Turbulence kinetic energy	$[J\ kg^{-1}]$
l	Length of the hole	$[m]$
L	Length scale	$[m]$
$\dot{m}$	Mass flow rate	$[kg\ s^{-1}]$
Nu	Nusselt number $\frac{HTC\ d_h}{k_{air}}$	$[-]$
P	Pressure	$[Pa]$
$P30$	Compressor outlet pressure	$[bar]$
Pr	Prandtl number	$[-]$
P/T	Pilot to Total fuel flow rate	$[\%]$
Q	Heat power	$[W]$
q''	Heat flux	$[W\ m^{-2}]$
Re	Reynolds number	$[-]$
r	Radius	$[m]$
S_h	Sherwood number	$[-]$
S_r	Source of radiative energy	$[W\ m^{-3}]$
SMD	Sauter Mean Diameter	$[m]$
$\hat{s}$	Curvilinear abscissa	$[m]$
T	Temperature	$[K]$
$T30$	Compressor outlet temperature	$[K]$
V	Velocity	$[m\ s^{-1}]$
x	Stream-wise direction	$[m]$
y	Orthogonal to plate direction	$[m]$
y^+	Dimensionless wall distance	$[-]$
We	Weber number	$[-]$
Y	Species mass fraction	$[-]$
z	Span-wise direction	$[m]$
Z	Mixture fraction	$[-]$

Acronyms

ACARE	Advisory Council for Aeronautics Research in Europe
CAEP	Committee on Aviation Environmental Protection
CFD	Computational Fluid Dynamics
CHT	Conjugate Heat Transfer
CIAM	Central Institute of Aviation Motors
CS	Cold Side
DES	Detached Eddy Simulation
DLR	Deutsches Zentrum für Luft- und Raumfahrt
DOM	Discrete Ordinate Method
EFF	EFFusion
FAR	Fuel Air Ratio
FGM	Flamelet Generated Manifold
GSSC	Generic Single Sector Combustor
HE	Heat Equation
HS	Hot Side
IATA	International Air Transport Association
ICAO	International Civil Aviation Organization
LES	Large Eddy Simulation
LII	Laser-Induced Incandescence
NEWAC	NEW Aero engine core Concepts
NSEs	Navier Stokes Equations
OPR	Overall Pressure Ratio
OTDF	Overall Temperature Distributon Fucntion
PDF	Probability Density Function
PERM	Partial Evaporation and Rapid Mixing
PIV	Particle Image Velocimetry
RANS	Reynolds Averaged Navier Stokes
RTDF	Radial Temperature Distribution Function
RTE	Radiative Transfer Equation
SAFE	Source bAsed eFfusion modEl
SAS	Scale Adaptive Simulation
SN	Swirl Number
SRS	Scale-Resolving Simulation
SST	Shear Stress Transport
SV-CARS	Shifted Vibrational Coherent Anti-stokes Raman Scattering
TIT	Turbine Inlet Temperature
UDF	User Defined Function
URANS	Unsteady RANS
WALE	Wall Adapting Local Eddy

Greeks

Θ	Angle	$[deg]$
ρ	Density	$[kg\ m^{-3}]$
μ	Dynamic viscosity	$[Pa\ s]$
ϕ	Equivalence ratio	$[-]$
ψ	Generic variable	$[-]$
κ	von Karman constant	$[s^{-1}]$

Subscripts

air	Air
eff	Effective
eq	Equilibrium
fuel	Fuel
g	Gas phase
l	Liner
c	Progress variable
rad	Radiation
30	Referred to Plane 30 (compressor discharge)
40	Referred to Plane 40 (combustor exit)
s	Subgrid-scale
t	Turbulent
vK	von Karman
w	Wall

Introduction

Aviation is increasingly gaining a key role in mid- long-range transportation of people. The improvement in safety and the cost reduction of air travel have lead to the growth of passenger demand over the past 20 years and this trend will continue in the next future. Recent ICAO forecasts [1] estimated an average growth per year of about 4.0% in air traffic for the 2020-2040 period, mainly driven by Asia and Middle East. The economic relevance of this sector, expected in 1% of world GDP to be spent on air transport in 2018 [2], has attracted the attention of the institutions and made available funds for several research programmes concerning the different aspects of a civil aircraft, from the airframe to aeroengine. Nowadays, the people sensibility to environmental issues is deeply affecting the aeroengine industry that have to face the pressing demands for engine with lower pollutant emissions. In Europe these and other needs were well-known as early as January 2001 when the "European Aeronautics: A vision for 2020" report [3] was published, immediately followed by the establishment of the Advisory Council for Aeronautics Research in Europe (ACARE) aiming to develop and main-

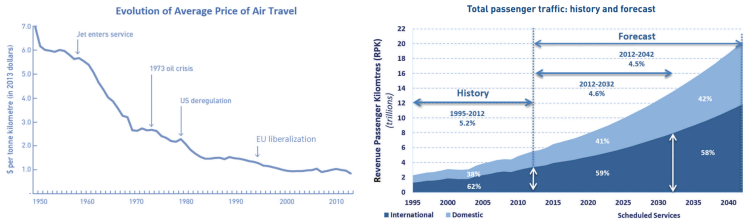

Figure 1: Evolution of the average price of air travel (left) and total passenger traffic (right) [1].

tain a roadmap that would help achieving the goals of Vision 2020 and so stimulating all European steakeholders in the planning of research programmes. Nevertheless, the evolving technologies and international scenario have recently called into question the sufficiency of the existing Vision 2020. For example, as a result of the ICAO-CAEP/6 meeting held in 2004, a -60% reduction of NOx emission by 2026 in respect to CAEP/6 levels at an Overall Pressure Ratio (OPR) of 30 was expected for long-range civil aircraft (i.e. turbofan/turbojet engines with rated thrust $> 26.7kN$). Moreover, at the ICAO-CAEP/10 meeting held in 2016 [4], completely new stringent standards for the CO_2 and $nvPM$ emissions were recommended and will apply to engine manufactured from 2020. As a consequence, the Vision 2020 goals were revised and their horizon was extended towards 2050 with the Fligthpath 2050, released in 2011. The Strategic Research and Innovation Agenda (SRIA) [5] developed by ACARE has the aim of achieving the Fligthpath 2050 goals while maintaining the global leadership of Europe in a safe, more efficient and "green" air transport. The short-term (2020), medium-term (2035) and long-term (2050) objectives proposed by SRIA will require to address five key challenges:

1. Meeting societal and market needs;
2. Maintaining and extending industrial leadership;
3. Protecting the environment and the energy supply;
4. Ensuring safety and security;
5. Prioritising research, testing capability and education.

European Union is funding the research on aeronautical field by the late 1987 through European Commission Framework Programmes for R&D, contributing to technology development up to TRL 6. One of the most important EU programme was proposed in the 2007 by the Clean Sky Joint Undertaking, a collaboration between public and private entities, for the development of environmentally friendly technologies related to the aircraft system. The success of this programme led to a more ambitious one in 2014, i.e. Clean Sky 2 [6], that is actually ongoing and aims to investigate novel aircraft, including small air transport, and further break down NOx, CO_2 and noise of $20 - 30\%$ by 2024, so contributing to the achievement of Flightpath 2050 objectives as shown in Fig. 2.
In this context, great research effort is devoted to improve the performance of the propulsive system, i.e. the gas turbine. The CO_2 emission are trivially reduced acting on the overall efficiency of the engine, which

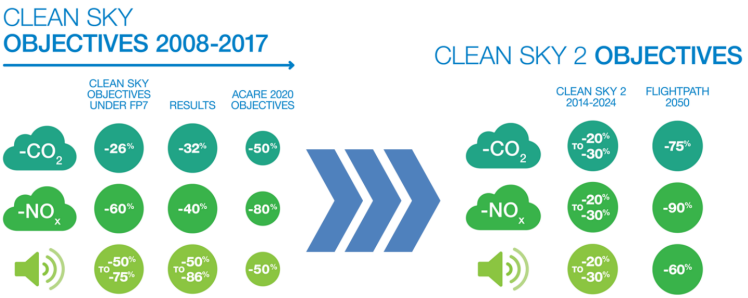

Figure 2: Evolution of the Clean Sky objectives [6].

can mean increasing the propulsive efficiency or the thermal efficiency. The former action has in the Ultra-High Bypass Ratio turbofan the most promising solution but it is not enough to meet the goal for 2050. Therefore, novel thermodynamic cycles are under investigation as well as a further increase of Turbine Inlet Temperature (TIT) and OPR. However, all the hot path components, that are the combustor and turbine, undergo stronger thermal stresses that could lead to dangerous engine damages and failures. To avoid this, a re-design of the aforementioned components is required, especially concerning the adopted materials and the cooling system; nowadays, this revolution is aided by the onset of new technologies, as the Additive Manufacturing (AM), that are stimulating the exploration of innovative cooling architectures, such as shaped holes, microchannels etc. On the other hand, the future trend of TIT and OPR lead to higher flame temperature, acting against the achievement of low NOx emissions because of the exponential dependency by temperature of the formation rate of Thermal NOx (i.e. Zeldovich mechanism), that is the dominant contribution in gas turbine applications; then, the reduction of stoichiometric regions, where the highest temperatures are observed, together with the minimization of residence time on the same zones is helpful to limit the NOx emission.
From its introduction in the middle of 1990s, the RQL (Rich burn-Quick mix-Lean burn) technology became the standard for low emission aeronautical burners thanks to its ability in keeping a stable combustion and therefore a safe operability of the engine during all the flight operations. Indeed, a small amount of air is sent to the swirler in order to have a rich primary zone, as shown in Fig. 3. The remaining air is mainly devoted to the dilution holes, acting to quench the flame and create a lean

environment in the downstream region. Thus, the flow split is strongly unbalanced towards dilution air which has a key role to limit pollutant emissions and control temperature profile at combustor exit (i.e. Pattern Factor), as required by the turbine designer. Despite their wide use, the RQL combustors have almost approached an asymptote in terms of reduction in pollutant emissions, especially concerning NO_x. It is related to the difficulties in a precise control of the combustion process and gas temperature because of the rapid non-ideal mixing with the dilution jets. For this reason it will be unable to respect the future limits for NOx, CO and soot emissions set by ICAO and ACARE Flight Path 2050 goals.
The technology challenge of these last decades regarding the emission abatement on aeroengine for civil market is leading to deep modifications in the concept design of aeroengine combustors, as depicted in Fig. 3. Nonetheless, the ideal condition of lean premixed flame is impractica-

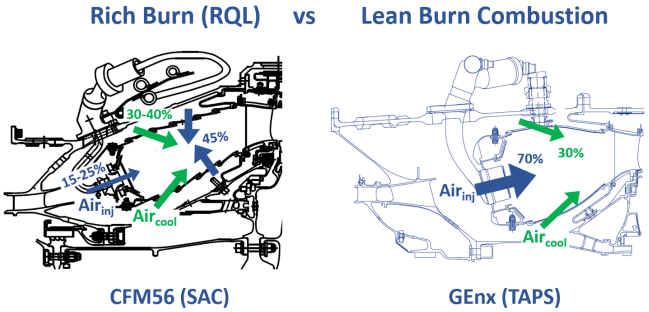

Figure 3: Comparison of size and flow split of RQL (left) and Lean Burn (right) combustors of General Electric manufacturer. Adapted from [7].

ble for aeronautical purpose because of the liquid fuel that makes the mixture preparation difficult and the occurring of blow-out, flashback and thermo-acoustic phenomena which affect the safety operability of the combustor. To overcome these issues the engine manufactures have focused the research efforts on Lean Direct Injection (LDI) technology, featuring a partially-premixed combustion that ensures a more stable behavior in all the operating conditions. In this new burning concept the injector design becomes crucial because a quick evaporation and mixing of fuel droplets with the oxidizer is required to have an homogeneous temperature field and an efficient combustion process. As a result, the Lean-burn injector is more complex than the RQL one, where almost all

the air coming from the compressor (i.e. about 70% of the total inflow) is delivered to the primary zone in order to have a lean mixture and lower temperature peaks [8].
Indipendently by combustor architecture, the requirements for control of exit gas temperature, emissions and metal temperature generate an intense competition for utilization of combustor airflow [9]. The flow split is mainly chosen according to design requirements about profile temperature and pollutant emissions and only the excess air is demanded to keep liner temperature below alloy melting point and avoid high metal temperature gradients. Moreover the higher the P30, the lower the cooling potential of air and the cooling system can be strongly stressed in both the above mentioned configurations. In RQL systems, as the major part of air provided by the compressor is delivered to dilution holes, insufficient coolant could be available. Despite a less critical thermal load, this issue is more relevant in Lean-burn devices where a large fraction of compressor efflux passes through the injector. Hence, never as now, the goal of improving the cooling effectiveness must be pursued. Moreover, the increasingly attention for Small Air Transport supported by Clean Sky 2 is rebooting the segment of small gas turbines in the aero-engine manufactures. The high power density of such engines is reflected in a high surface to volume ratio of the combustion chamber and, in turn, to strong thermal load on the liner, where the development of innovative cooling systems will be a necessary step in the design process.
In this context highly-effective cooling strategies are required and, as a results, research effort on combustors is widely focused on the investigation of advanced cooling techniques, such as effusion cooling, double-wall configurations, thermal barrier coating, matrix cooling and traspiration cooling [10]. In particular, during past years, multi-perforated liners are gaining a key role thanks to its double benefit: film coverage that protects the liner from hot gases and heat sink within holes due to the passage of coolant [11]. The definition of new hole patterns and geometries (i.e. shaped holes) as well as the prediction of their effects on adiabatic effectiveness and metal temperature are the object of many experimental and numerical studies [11, 12, 13, 14]. However, all these research activities investigated test rigs far from real aeroengine combustors in terms of geometry, flow field and operating conditions. More recently the attention was focused on the interaction between swirling flows and effusion cooling. Many experimental studies on representative test cases (i.e. effusion cooled lean-burn injectors at non-reactive conditions) pointed out the interaction between swirling flow and film coverage [15, 16, 17, 18, 19, 20, 21, 22].
The considerable cost and time associated to experimental campaigns

make such an approach unsuitable during the preliminary stages of combustor design, increasing the attractiveness of numerical simulations. The complex interaction between turbulence, combustion, radiation and heat conduction leads the prediction of wall temperatures challenging and multiphysics approaches are required. Tools combining 0D and 1D approaches [23, 24] based on the procedure described by Lefebvre [25] are able to quickly solve Conjugate Heat Transfer (CHT) problems with acceptable accuracy on simple geometries but lack of predicting capabilities when applied on complex geometries and reacting flow field as in practical combustors. One of the common numerical methods to deal with such geometries is Computational Fluid Dynamics (CFD), which can provide high fidelity results and, if compared with experiments, a deep insight on the involved phenomena. These investigation can be performed at different levels of detail. RANS approaches, i.e. the standard tool in industrial framework, are useful to obtain thermal design tips with an affordable computational cost but they are not always suitable to catch the strong interactions between turbulence, chemistry and spray of swirling reacting flows as well as the turbulent wall heat fluxes and Scale-Resolving Simulations (SRSs) should be recommended [26, 27, 28]. The intrinsically unsteady characteristic of these last approaches, unlike steady RANS, requires to handle a wide range of time scales for the involved phenomena. The solution of such a multiphysics problem have to deal with the need of huge computational resources and cannot be efficiently faced in a fully-coupled manner, where the entire set of equations is solved together for all the iterations. Alternatively, loosely-coupled methods have dedicated simulations for each physics and exchange only some quantities at a given frequency at the interface between two coupled domains, so minimizing the CPU cost. For this reason, several applications can be found in literature, both for RANS [29] and SRS [30, 31, 32] models. In addition, loose coupling increases the feasibility of simulations on multiperforated liners, taking advantage of the many approaches [33, 34, 35] with reduced computational effort proposed to model the film cooling injection and the heat sink effect.

Aim of the work

The issues associated to the solution of a multiphysics problem within a combustion chamber led to the development in ANSYS CFX framework of the THERM3D in-house procedure [35], employing three steady simulations for fluid, solid and radiation. This procedure replaces effusion holes with inlet/outlet patches that ensure mass and energy conservation

with lower computational cost. During the present research work the THERM3D was implemented in ANSYS Fluent to exploit a wider choice of numerical models and schemes.
The main aim of this study was the development of an unsteady multiphysics tool, both in steady and unsteady framework, for the aero-thermal design of aeronautical combustors. In particular, the focus was on the CHT modelling in the context of scale-resolving simulations to have a high-fidelity computationally-effective method for the final design that can support experimental campaigns as well as minimize failures during the component tests, reducing the overall cost for the development. Starting from THERM3D, the U-THERM3D (Unsteady-THERM3D) procedure was set up and validated to several test cases in order to assess the predictive capabilities of the methodology. Even though the present application is restricted to CHT problems, the tool aims to be a framework where loosely coupled problems can be efficiently solved.

Thesis outline

During this research activity the different phenomena involved in the investigated multiphysics problem and their mutual interactions were analysed from a numerical perspective. Several aspects related to heat transfer, combustion and radiation modelling as well as to the numerical treatment of the cooling system must be taken into account and, therefore, a special effort was devoted to review the state of the art on CHT studies. This necessary stage has called the attention on the importance of an optimization of the procedure for a CPU expensive simulation as the multiphysics one. The final application of the unsteady tool on a real aeroengine burner was anticipated by the assessment on increasingly complex test cases to isolate a lower order of modelling aspects and have a deep insight on each of them.
The manuscript will be organized as follows.

Chapter 1: The most important aspects of Conjugate Heat Transfer are here reviewed from a multiphysics perspective. The main governing equations are reported to emphasize the huge differences in terms of time and space scales. In addition, the methodologies available in literature to solve unsteady heat transfer problems are presented, with a focus on stability and main limitations.

Chapter 2: In this chapter the U-THERM3D procedure is described and the need of a loose coupling as well as a proper load balancing is pointed

out to minimize the computational cost. Lastly, the tool is validated on predictable simple problems whereas a further assessment of spray flame modelling is carried out for high pressure applications.

Chapter 3: The present approach is applied in the multiphysics simulation of a swirl-stabilized sooting flame where radiation has a key role in the redistribution of energy and in the soot emissions. Quartz window temperature is computed and compared against THERM3D results and experimental data to appreciate the huge improvement in a scale-resolving context.

Chapter 4: This chapter is devoted to a complete investigation of the parameters affecting an high-fidelity design of a novel combustion chamber. An effusion-cooled lean burn aeroengine combustor is simulated at different levels of complexity with a focus, once again, on the liner temperature. The results show the main advantages of a scale-resolving modelling in the prediction on the aero-thermal field, emissions and metal temperature.

In the last chapter, a summary of the main achievements of this research is given together with conclusions and recommendations for future works.

Chapter 1

Multiphysics and multiscale characteristics of CHT modelling

The constrain on metal temperature is one of the main requirements during the design of modern gas turbine. Steep thermal gradients, heat load cycles, fast transient warm up and hot spots can promote creep, oxidation, hot corrosion and fatigue failures of hot section components, affecting their durability, efficiency and, then, the overall operating cost of the engine. The progress in material technology, in any case remarkable during the last decades, will not be able to keep up the rise of Turbine Inlet Temperature, as shown in Fig. 1.1 for turbine blades. The introduction of cooled components added a degree of freedom in the design of turbine blades, partially freeing the developing trend in thermal efficiency and materials. The design of cooling systems in rotor blades gets complicated by the rotating framework that generates centrifugal forces and coriolis effect on the coolant flow.
The trend of Fig. 1.1 remains still valid as far as the combustor liner is concerned but the thermal design can become even more challenging. Indeed, it experiences a severe environment with the highest pressure and temperature of the engine as well as complex phenomena, such as combustion and radiation. Under such conditions, the prediction of metal temperature is in all respects considered a multiphysics problem. In a typical configuration, the liner is two-side cooled and wall temperature at the solid-fluid interfaces depends on heat transfer through the liner that, in turn, depends on wall and gas temperatures. However, the external heat transfer must be equal to the internal conduction that is a function of the temperature at the two wall interfaces. This coupled problem is also referred as Conjugate Heat Transfer (CHT).

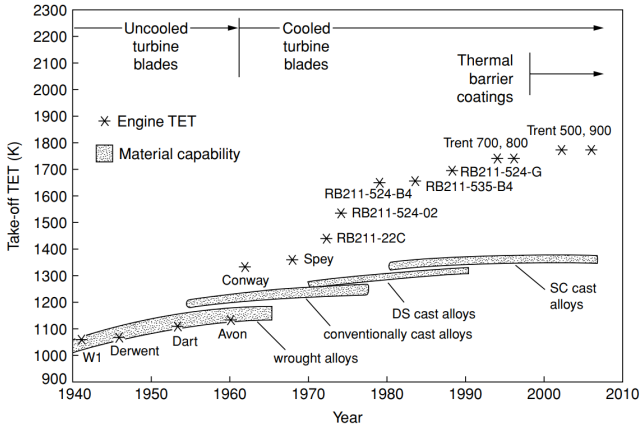

Figure 1.1: Historical trend for Turbine Entry Temperature of Rolls Royce engines and material capability [36].

The complexity of this matter makes the numerical modelling of CHT very challenging. Fig. 1.2 shows an overview of the thermal design tools available in literature. Low-order approaches, as 0D and 1D ones [23, 24], are based on procedures similar to that described by Lefebvre [25] and provide a prompt solution. 0D tools return a unique value for the metal temperature, that must be considered as a spatially-averaged quantity given by reference values for properties and geometry. A 1D temperature distribution in the streamwise direction can be provided considering the axial variations of the inputs to the model that always occur in a combustor chamber. Correlations are employed to close the problem but they are usually developed using simplified hypothesis and geometry. Even if a tuning can extend their applicability range, correlations lack in accuracy when applied to complex 3D flow fields as in a combustor. In this case, inhomogeneities in the liner temperature can be numerically predicted only using CFD. Nowadays steady-state simulations exploiting RANS models are the standard in industrial applications as the improvement in CPU speed allows to perform calculations with a reasonable computational time. Nevertheless, turbulence has a strong influence on the aerothermal field and can benefit of unsteady simulations in a Scale Resolving framework that ensure a better resolution of turbulence spectrum despite a higher computational cost. Even though the increasingly performing hardware for Computer-Aided Engineering (CAE) makes Scale-Resolving Simulations

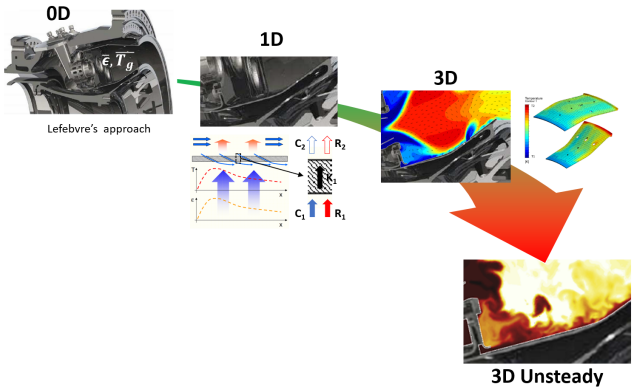

Figure 1.2: Main classification of thermal design tools (contributions from [37]).

less time-demanding, difficulties arise because of the different domains and time scales involved in the present multiphysics problem. All these aspects will be here generically addressed from a theoretical and numerical perspective and, more specifically, in the context of aeroengine combustors.

1.1 Classification of CHT approaches

The first grouping of CHT methods was already depicted in Fig. 1.2 based on the geometrical resolution. While in 0D and 1D approaches other classifications are of poor interest, in a 3D discretisation they are useful because characterized by differences in computational cost, accuracy as well as in the algorithm of resolution and the complexity of its implementation.
The three thermal phenomena involved in aeroengine combustors, that are convection, conduction and radiation, require the continuity of energy-related quantities. In the follow the term "coupling interface" will be used to identify the region where two distinct physics show their coupling. At the fluid/solid coupling interface, i.e. the walls, heat fluxes and temperatures must equal on the two sides. At the fluid/radiation coupling interface, corresponding to the fluid domain, source/sink of energy due to radiation as well as pressure, temperature and chemical species are the

same. Last but not least, analogous considerations are valid for radiative heat fluxes and solid temperatures at the radiation/solid coupling interface, but also for energy source/sink when solid material has semi-transparency properties.
The main classification in CFD context relies on the solution strategy, so that a CHT approach can be:

- Strongly coupled;
- Loosely coupled.

Strongly (or fully) coupled methods solve all the equations of the multiphysics problem at each iteration. The solver goes to the next iteration when convergence is reached for the variables at the coupling interfaces. A loose coupling, instead, satisfies the convergence criteria only at the end of simulation. Equations of the different phenomena are solved in a segregated manner, meaning that they are coupled only at specific iterations where interface variables are updated relying on information of the previous coupling.
Depending on the objective of the CHT simulation the approaches can be distinguished, as mentioned in Fig. 1.2, in:

- Steady coupled;
- Unsteady coupled.

Steady coupling is exploited when the mean metal temperature is desired. On the other hand, if the interest is on the transient evolution of wall temperature or its fluctuations over time, unsteady coupled solvers are needed.
If a loosely coupled approach is chosen, the iteration/time-step advancement is another question that is worth an answer. The possibilities are:

- Sequential (or staggered) coupling;
- Parallel coupling.

In a sequentially coupled approach the solvers run one at a time: each solver gets information from the previous one and provides data to the next one. Using a parallel coupling, instead, the solvers run simultaneously and exchange quantities at the same time at a given frequency. In literature, steady coupled methods are usually solved in a sequential manner while unsteady coupling is efficiently employed with a parallel algorithm.

1.2 Multiphysics heat transfer problem

The Conjugate Heat Transfer in aeroengine combustors requires the knowledge of all the actors playing in this process and how they interact each other. Fig. 1.3 shows the main phenomena involved in the determination of the liner heat load, that are:

- convection;
- combustion;
- radiation;
- conduction.

In addition, other phenomena can be added to the list, i.e. spray evolution, that could affect the prediction of flow field quantities and, as a result, of metal temperature but also increase the complexity of the investigated problem. The use of "multiphysics" term in this context is related to

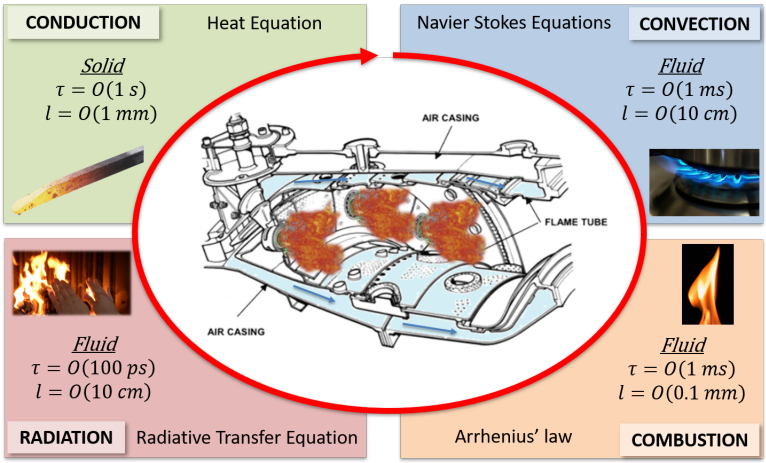

Figure 1.3: Summary description of the main phenomena involved in a combustor, with emphasis on the characteristic scales and the governing equations.

the different nature of the above mentioned physics, which are governed by their own transport equations and can take place on distinct physical

domains. The main consequence is the extension of characteristic time and space scales from very small to large orders of magnitude. This wide range unavoidably adds modelling difficulties that will be illustrated in the follow. In the present section, instead, each phenomena will be investigated from a theoretical perspective to estimate the order of magnitude of these scales.

1.2.1 Conduction

When a solid, liquid or gas is observed at a microscopic level, differences of kinetic energy between two molecules coming into contact by means of vibration (solid) or collision (fluid), lead to a transfer of energy from the more to less energized particle [38]. At a macroscopic level, instead, the same phenomenon is named conduction and consists of heat transfer from higher temperature regions to lower ones following the Fourier's law, that is:

$$q'' = -\lambda(T)\frac{dT}{dx} \tag{1.1}$$

where $\lambda(T)$ is a transport property of the material known as thermal conductivity and function of temperature. Even if conduction can be observed in all states of matter, in the following it will be referred only to the solid domain, where it represents the governing heat transfer mode. In this case, the conservation equation, obtained by an energy balance on a control volume, is the Heat Equation:

$$\rho_s \frac{\partial c_v T}{\partial t} = -\sum_{i=1}^{3} \frac{\partial}{\partial x_i}(\lambda \frac{\partial T}{\partial x_i}) + \dot{\omega}_T \tag{1.2}$$

where ρ_s is the solid density, c_v is the specific heat at constant volume and $\dot{\omega}_T$ is the energy source/sink term.
Eq. 1.2 can be solved if one or more of the following boundary conditions are defined:

$$-\lambda \frac{\partial T}{\partial n}\bigg|_{y=y_w} = q''_w \tag{1.3a}$$

$$T\big|_{y=y_w} = T_w \tag{1.3b}$$

representing fixed heat flux (Eq. 1.3a) and temperature (Eq. 1.3b) at wall.
With the hypothesis of constant properties and negligible source term,

Eq. 1.2 can be rewritten in the following dimensionless form [38]:

$$\frac{\partial T^*}{\partial t^*} = -\frac{\alpha\tau}{L^2}\sum_{i=1}^{3}\frac{\partial^2 T^*}{\partial x_i^{*2}} \tag{1.4}$$

where $\alpha = \lambda/(\rho c_v)$ is the thermal diffusivity of the material while T^*, t^* and x_i^* are respectively dimensionless temperature, time and space coordinates defined as:

$$T^* = \frac{T}{\Delta T}, \quad t^* = \frac{t}{\tau}, \quad x_i^* = \frac{x_i}{L} \tag{1.5}$$

In these fractions, the denominator terms are characteristic temperature, time and length of the investigated problem. Choosing $\tau = L^2/\alpha$ the non-dimensional time corresponds to the Fourier number Fo:

$$t^* = \mathrm{Fo} = \frac{\alpha t}{L^2} = \frac{\text{heat conduction rate}}{\text{thermal energy storage}} \tag{1.6}$$

In a transient conduction problem thermal diffusivity plays a key role for the temperature evolution of the solid. Similar solutions in the $(\mathrm{Fo}, T^*, x_i^*)$ space can provide different results in the physical one depending on α; high values are usually associated to fast transient while lower ones lead to quasi-steady problems.

1.2.2 Convection

Convection is an heat transfer mechanism that is associated to mass transport and, then, to a fluid in motion. More specifically, it is not heat that is convected but internal energy [38].
In fluid dynamics the system of Navier-Stokes Equations (NSEs) is the more complete model to represent the continuum regime of a flow field. Conservation equations for mass, momentum, species and sensible enthalpy of a gaseous reactive mixture are:

$$\frac{D\rho}{Dt} = \dot{\Omega}_{mass} \tag{1.7a}$$

$$\rho\frac{Du_i}{Dt} = -\frac{\partial p}{\partial x_i} + \frac{\partial \tau_{ij}}{\partial x_j} + \rho g_i + \dot{\Omega}_{mom} \tag{1.7b}$$

$$\rho\frac{DY_k}{Dt} = \frac{\partial \rho J_{Y,j}}{\partial x_j} + \dot{\Omega}_{Y,k} + \dot{\omega}_k \tag{1.7c}$$

$$\rho\frac{Dh_s}{Dt} = \frac{Dp}{Dt} + \frac{\partial \rho J_{h,j}}{\partial x_j} + \tau_{ij}\frac{\partial u_i}{\partial x_j} + \rho\sum_{k=1}^{N} Y_k f_{k,i} V_{k,i} + \dot{\Omega}_{vap} + \dot{\Omega}_h + \dot{\omega}_T \quad (1.7d)$$

where ρ, u_i, p, Y_k, V_k and h_s are the gas density, i-th velocity component, static pressure, k-th species mass fraction, diffusion velocity of k-th species and sensible enthalpy, respectively. Newton's law, Fick's law and Fourier's law are commonly used to model respectively momentum, species and energy diffusion fluxes (i.e. J_ϕ) while other phenomena, such as Dufour and Soret effects, are neglected for most industrial applications. Momentum diffusion fluxes are usually rewritten in the form of a stress tensor τ_{ij}. Species diffusion $J_{Y,j}$ can redistribute the energy with two mechanism: volume forces $f_{k,i}$ and differences in species sensible enthalpy. While the former can be neglected, the latter becomes important in combustion processes as a result of the strong gradients of species concentration that increase $J_{Y,j}$. Hence, the general form of $J_{h,j}$ in Eq. 1.7d is:

$$J_{h,j} = -\lambda\frac{\partial T}{\partial x_j} + \rho\sum_{k=1}^{N} h_k Y_k V_{k,j} \quad (1.8)$$

where the first right-hand term represents conduction.
In the previous system a key role is played by the source/sink contributions: terms $\bar{\dot{\Omega}}_{mass}$, $\bar{\dot{\Omega}}_{mom}$, $\bar{\dot{\Omega}}_{Y,k}$ and $\bar{\dot{\Omega}}_{vap}$ are related to the interactions with a liquid phase within the computational domain while $\bar{\dot{\Omega}}_h$ includes other phenomena, such as radiation. Moreover, source terms related to combustion are specified with ($\bar{\dot{\omega}}_\psi$) and its specific modelling will be discussed in Section 1.2.3. This PDEs system must be accompanied by proper boundary conditions for its closure and numerical solution. In particular, concerning wall boundaries, energy equation requires fixed heat flux or wall temperature condition, similarly to Eqs. 1.3.
If the problem involves a non-reacting incompressible flow with a single phase and component, Eq. 1.7d can be simplified and with the additional hypothesis of constant properties and absence of source terms it becomes:

$$\rho c_p\frac{DT}{Dt} = -\lambda\sum_{i=1}^{i=3}\frac{\partial^2 T}{\partial x_i^2} + \tau_{ij}\frac{\partial u_i}{\partial x_j} \quad (1.9)$$

As in Section 1.2.1, this last equation can be rewritten in a dimensionless form introducing, in addition to the variables defined in Eq. 1.5, the dimensionless velocities:

$$u_i^* = \frac{u_i}{U} \quad (1.10)$$

where U is the characteristic velocity. Considering for a fluid flow the characteristic time $\tau = U/L$, Eq. 1.9 becomes [38]:

$$\frac{DT^*}{Dt^*} = -\frac{1}{\mathrm{RePr}} \sum_{i=1}^{i=3} \frac{\partial^2 T^*}{\partial x_i^{*2}} + \frac{2\mathrm{Ec}}{\mathrm{Re}} \Phi^* \tag{1.11}$$

Here, Φ^* is the dimensionless form of the viscous dissipation function:

$$\Phi = \frac{1}{\mu} \tau_{ij} \frac{\partial u_i}{\partial x_j} \tag{1.12}$$

Three dimensionless groups appear in Eq. 1.11, that are the Reynolds number Re, the Prandtl number Pr and the Eckert number Ec:

$$\mathrm{Re} = \frac{\text{inertia forces}}{\text{viscous forces}} = \frac{\rho U L}{\mu} \tag{1.13a}$$

$$\mathrm{Pr} = \frac{\text{molecular momentum diffusivity}}{\text{thermal diffusivity}} = \frac{\mu c_p}{k} = \frac{\nu}{\alpha} \tag{1.13b}$$

$$\mathrm{Ec} = \frac{\text{kinetic energy of the flow}}{\text{enthalpy difference of boundary layer}} = \frac{U^2}{c_p \Delta T} \tag{1.13c}$$

The magnitudes of these numbers affect the relative contribution of the different heat transfer mechanisms to the temperature field. However, the term related to viscous dissipation is often neglected. In laminar flows, characterized by low Re, steep temperature gradients can promote heat transfer by conduction. On the other hand, high Re flows as the turbulent ones, simplify Eq. 1.11 in:

$$\frac{DT^*}{Dt^*} \approx 0 \tag{1.14}$$

highlighting the prevalence of convective motions in the energy distribution of turbulent flows. If the fluid flow is dominated by buoyancy effects the process is called natural convection. If the inertia forces drive flow motion forced convection occurs, that in the present applications is definitely the dominant process.
Independently by the flow regime, approaching a wall the flow velocity tends to zero and the surface is covered by a stagnant fluid layer, where conduction occurs:

$$q''_{cond,w} = -\lambda_f \left. \frac{\partial T}{\partial n} \right|_{y=y_w} \tag{1.15}$$

Here, λ_f is the thermal conductivity of fluid and at equilibrium $q''_{cond,w}$ must be equal to the convective heat transfer. However, in Eq. 1.15

the near-wall temperature gradient depends on the above flow where convection prevails. Consequently, the Newton's law of cooling is used to model convection:

$$q''_{conv,w} = h(T_w - T_f) \tag{1.16}$$

where h is the heat transfer coefficient and T_f is a reference fluid temperature, often set to the far-field temperature. Unlike λ_f, h is not a fluid property because it takes into account of the flow field characteristics. Indeed, making equal Eqs. 1.15 and 1.16 and making dimensionless the temperature gradient, the heat transfer coefficient can be expressed as:

$$h = \frac{\lambda_f}{L} \frac{\partial T^*}{\partial n^*}\bigg|_{y^*=0} \tag{1.17}$$

or, in its dimensionless form:

$$\mathrm{Nu} = \frac{hL}{\lambda_f} = \frac{\partial T^*}{\partial n^*}\bigg|_{y^*=0} = f(\mathrm{Re}, \mathrm{Pr}, \mathrm{Ec}) \tag{1.18}$$

where Nu is the Nusselt number that in general terms, according to Eq. 1.11, depends on the Re, Pr and Ec numbers.

Turbulence

Turbulence is the natural state of a fluid flow and occurs when the Reynolds number exceeds a critical value. In this case inertia of the flow (convection contribution) is higher than viscous forces (diffusion contribution) and the flow becomes irregular and chaotic, increasing the transport phenomena, such as diffusion of mass, heat and momentum.
In turbulent regime, the flow is characterized by small coherent vortices, the eddies. These three-dimensional turbulent structures, that born random, are responsible for stochastic velocity fluctuations $u'_i(t)$ and for their correlation between two points closer than a certain distance named integral length scale l_0. These turbulent structures are superimposed in space, with larger ones that contain the smaller ones, as shown in Fig. 1.4. The size of smallest vortices depends strongly on Reynolds number and since eddies evolve in all directions the phenomenon is intrinsically three-dimensional.
Turbulence can be represented with the so-called Reynolds decomposition:

$$u_i(\mathbf{x}, t) = \bar{u}_i(\mathbf{x}) + u'_i(\mathbf{x}, t) \tag{1.19}$$

where $\bar{u}_i$ is the mean value, while the fluctuating component can be viewed as a statistical population with its probability distribution and, accord-

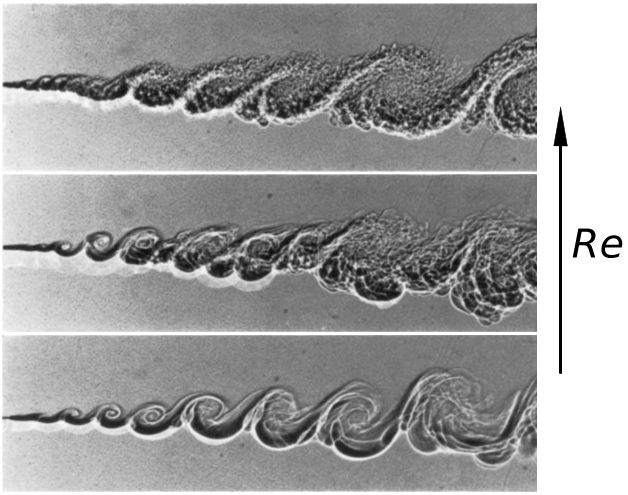

Figure 1.4: Effect of Reynolds number on the turbulent structures in a mixing layer (adapted by Brown and Roshko [39])

ingly, standard deviation $u_{i,rms}$. Such quantity is related to turbulent kinetic energy (TKE) k, reflecting the level of unsteadiness and expressed as:

$$k = \frac{1}{2}(u_{x,rms}^2 + u_{y,rms}^2 + u_{z,rms}^2) = \frac{3}{2}u_{rms}^2 \tag{1.20}$$

In a turbulent flow, eddies can be found in a wide range of spatial, temporal and velocity scales. Each one has a specific role in the so-called Energy Cascade process, which explains how the flow dissipates the turbulent kinetic energy: biggest anisotropic scales (energy containing range), that have a characteristic length similar to the domain dimension, introduce this energy in the cascade process whereas the smallest isotropic ones work to dissipate it (dissipation range). Between these scales there is the inertial sub-range that transports k towards smaller scales. This transfer process occurs because eddies disrupt and become ever smaller and more isotropic. In some cases backscattering phenomena can also occur, where the energy flux between the scales is inverse respect the cascade process. The energy distribution between the eddies of different scales is represented by the energy spectrum $E(\kappa)$ (Fig. 1.5), such that:

$$E(\kappa)d\kappa = dk \tag{1.21}$$

where $\kappa = 2\pi/l$ is the wave number related to eddies of size l. From the

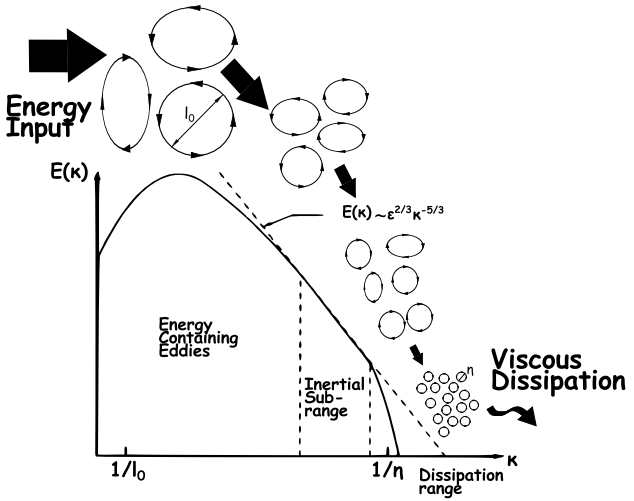

Figure 1.5: Energy spectrum with representation of the Energy Cascade process

shape of $E(\kappa)$ in the inertial subrange shown in Fig. 1.5, a more general expression of the energy spectrum may be determined as:

$$E(\kappa) = C\epsilon^{2/3}\kappa^{-5/3} f_L f_\eta \tag{1.22}$$

where f_L and f_η are empirical functions that must be introduced to model the energy containing range and the dissipation range, respectively.
As already reported, the largest eddies have scales, called integral scales (l_o,u_0,τ_0), with dimensions of the same order of characteristic scales of the flow ($l_0 = o(L)$ and $u_0 = o(u_{rms}) = o(\bar{u})$) and therefore influenced by boundary conditions. As a results, such turbulent structures do not shown universal features and have the most part of energy and anisotropy of the flow. On the other hand smallest scales, i.e. the Kolmogorov scales, are responsible of the dissipation process and present viscous forces comparable to the inertial ones ($Re_\eta = u_\eta \eta/\nu \approx 1$). In equilibrium condition the energy transfer equals the energy dissipation and this last term depends only on the integral scales. Thus an useful parameter, specified as turbulent dissipation rate ϵ, can be defined through of a

dimensional analysis as:

$$\epsilon \approx \frac{u_0^3}{l_0} \approx \frac{u_0^2}{\tau_0} \tag{1.23}$$

It is worth noting that such quantity is independent from cinematic viscosity ν and that equilibrium hypothesis is especially valid for the small eddies which promptly adapt themselves on large scales dynamics.
Combining Equation 1.23 with $k \approx u_0^2$ the integral turbulent length scale can be rewritten as:

$$l_0 \propto \frac{k^{1.5}}{\epsilon} \tag{1.24}$$

The remaining scales may be calculated for high Re flows using the well-known three Kolmogorov hypothesis [40]:

1. In turbulent flows exist a length scale $l_{E1} << l_0$ below which the turbulent scales are statistically isotropic. These are the Kolmogorov scales.

2. These isotropic scales and their statistics have an universal shape only determined by ν and ϵ. Thus, by means of a dimensional analysis, those quantities can be estimated as:

$$\eta = \left(\frac{\nu^3}{\epsilon}\right)^{0.25} , \quad u_\eta = (\epsilon\nu)^{0.25} , \quad \tau_\eta = \left(\frac{\nu}{\epsilon}\right)^{0.5} \tag{1.25}$$

3. Statistics of intermediate scales, such that $l_0 >> l >> \eta$ (i.e. corresponding to the inertial subrange), have an universal shape which depends only on ϵ. In this range, for a given length scale l, velocity and time scales are estimated as:

$$u(l) \approx (\epsilon l)^{1/3} \approx u_0 (l/l_0)^{1/3} , \quad \tau(l) \approx (l^2/\epsilon)^{1/3} \approx \tau_0 (l/l_0)^{2/3} \tag{1.26}$$

Hence, it is clear that in this range smaller eddies have also smaller characteristic velocity ($\approx u(l)$) and "lifetime" ($\approx \tau(l)$).

1.2.3 Combustion

Combustion is an oxidation reaction highly exothermic in which, for aeroengine applications, oxidant species is oxygen O_2 and fuel species is an Hydrocarbon ($C_x H_y$). The reaction mechanism is usually extremely complex, involving hundreds of species and thousands of elementary reactions, each of them taking place in gaseous state, where molecular mixing is achieved and the elementary reaction occurs; thus, liquid fuels

need to evaporate before oxidize. The process includes chain branching reactions, a series of consecutive reaction steps with a globally net positive production of highly reactive intermediate species causing the self-acceleration of fuel consumption. These species, said chain carriers, are atoms or free radicals (i.e. components having unpaired electrons) in small concentration and with a short lifetime. As the residence time of species is not normally sufficient to reach equilibrium state in practical conditions, combustion is dealt with chemical kinetics.
Considering a simple reaction as follows:

$$n_A A + n_B B \rightarrow n_C C + n_D D \tag{1.27}$$

the reaction rate RR can be expressed with the law of mass action as:

$$RR = K(T) C_A^{\alpha} C_B^{\beta} \tag{1.28}$$

where K is the specific reaction rate constant, depending on temperature. This law, with experimental basis, states that RR is a strict function of the reactants concentrations C_i. The exponents α and β correspond to the stoichiometric coefficients for elementary reactions or to experimentally-fitted values for global reactions.
In order to evaluate K the Arrhenius model is usually chosen:

$$K(T) = A_f T^{\beta} e^{-\frac{E_a}{RT}} \tag{1.29}$$

where A_f and T^{β} $(0 \leq \beta \leq 1)$ are, respectively, the collision frequency and the Boltzmann factor. This last specifies the fraction of collisions that have energy level greater than the activation energy E_a, defined as the energy barrier that reactants must overcome to initiate the reaction. Afterwards, when combustion takes place, E_a is supplied by heat generated from reaction process.
Eq. 1.28 highlights that combustion is strongly influenced by species concentration. As the reactions occur only when stoichiometric conditions are reached at a molecular level, mixing plays a key role to the success of the entire process. In laminar flames, mixing is only driven by molecular diffusion with unavoidable low reaction rates. On the other hand, turbulence can increase the burning rate because of the interaction between flame and eddies. Indeed, flame front is stretched by vortices resulting in higher flame surface and gradients while the enhanced mixing promotes the addition of fresh reactants into the reaction zone: these properties make turbulent flames more interesting from an industrial point of view.
A key parameter for premixed flames is the laminar flame speed s_L, that is the speed at which the flame front moves with respect to the fresh

gases [41]. It takes small values that depend on thermal diffusion and, above all, on reaction rate. The flame brush, defined as the envelope of the instantaneous flame front that still moves at a flame speed s_L locally normal to the flame front, can be identified by experiments. However, due to the turbulence, a wrinkling of the flame front occurs, causing an increase in flame surface A_T and consumption of reactants, as shown in Fig. 1.6. This increased reaction rate is justified with a turbulent flame

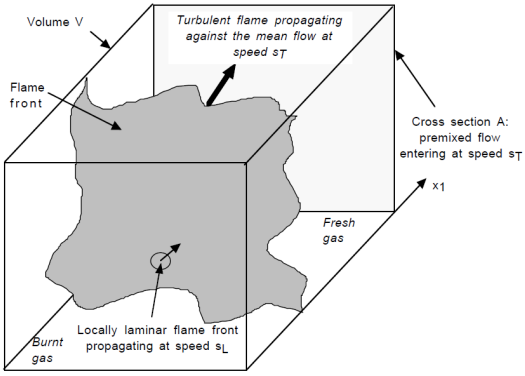

Figure 1.6: Effects of turbulence on a premixed flame front [41]

speed, higher than s_L. Referring to Fig. 1.6, s_T can be expressed as [42, 43]:

$$\frac{s_T}{s_L} = \frac{A_T}{A} \approx 1 + \frac{u'}{s_L} \tag{1.30}$$

that shows the direct link with turbulence by means velocity fluctuations. Different regimes can be found in turbulent premixed flames that are summarized in the Borghi Diagram [44] shown in Fig. 1.7, as a function of the Damkohler number Da and the Karlovitz number Ka:

$$\mathrm{Da} = \frac{\text{turbulent mixing}}{\text{chemistry}} = \frac{L_T s_L}{\delta_L u'} \tag{1.31a}$$

$$\mathrm{Ka} = \frac{\text{chemistry}}{\text{turbulent micromixing}} = (\frac{\delta_L}{L_k})^2 \tag{1.31b}$$

which represent a comparison between turbulence and chemical scales. Damkohler number is defined for the largest eddies and corresponds to the ratio of the integral time scale to the chemical time scale, whereas Karlovitz number corresponds to the inverse of a Damkohler number

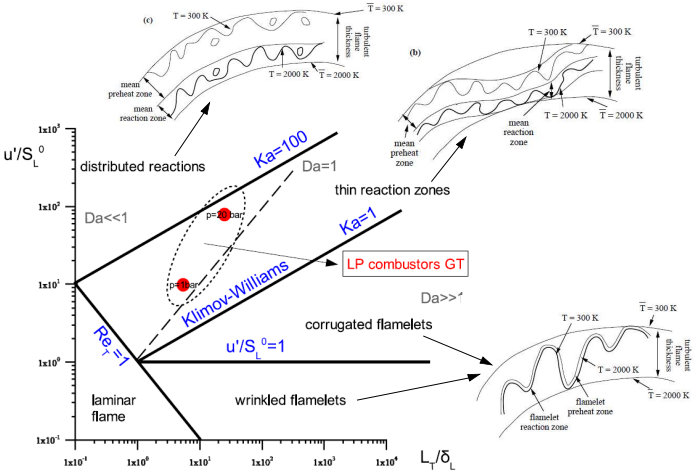

Figure 1.7: Borghi diagram for turbulent premixed flames[45]

computed for the smallest eddies, i.e. is the ratio of the chemical time scale to the Kolmogorov time scale.
When $Ka < 1$, the chemical time scale is shorter than any turbulent time scales and the flame front is thin, with thickness smaller than the Kolmogorov scale. The inner structure of the flame is close to a laminar one and this regime is identified as flamelet regime.
When $1 < Ka < 100$ a thickened wrinkled flamelet is observed because the smallest eddies are able to modify the preheat zone while the reaction zone, smaller than η is kept laminar. This regime, called thin reaction zone, is typical of gas turbine combustors.
As Ka further increasing, ($Ka > 100$, $Da < 1$) turbulent motions have shorter characteristic times than the chemical reaction time and reactive phenomenon is limited by chemistry. Here, both preheat and reaction zone are affected by turbulent motions and no laminar structure could be longer identified (distributed reaction regime).

1.2.4 Radiation

Unlike conduction and convection, radiative heat transfer occurs independently by the presence of a material medium. All the bodies with a temperature above 0 K emits thermal radiation in the form of electro-

magnetic waves. A strongly non-linear relation links radiative heat flux emitted by any body with its temperature:

$$E = \sigma_0 \epsilon T^4 \tag{1.32}$$

where $\sigma_0 = 5.67 \cdot 10^{-8} [W/(m^2 K^4)]$ is the Stefan-Boltzmann constant and ϵ is a material property called emissivity with $0 \leq \epsilon \leq 1$ ($\epsilon = 1$ only for blackbody). Eq. 1.32 represents the generalization of Stefan-Boltzmann's law for real surfaces and quantifies the energy emitted by a surface per unit time and per unit area in the whole wavelength spectrum. The emissive power per unit wavelength E_λ, called monochromatic emissive power, is well-known for a blackbody by the Planck's law, that shows the distribution of E_λ among the wavelengths for a certain temperature. In real surfaces, instead, the emissivity becomes dependent on wavelength as well as the emissive power itself and a graybody approximation is commonly applied, as depicted in Fig. 1.8, where the emissivity is set equals to a constant average value.

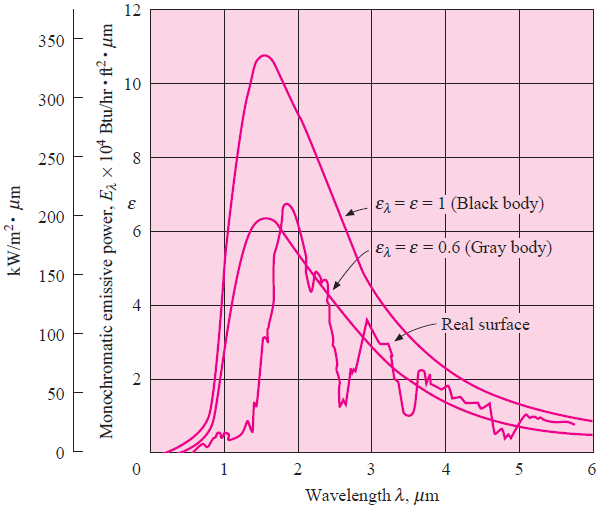

Figure 1.8: Radiation spectra from a blackbody at 3000 °F, an ideal gray body and a real surface [46]

In addition to emissivity, a generic material shows radiative properties also regarding the incident radiation on its surface. Given the total upcoming energy, a fraction r will be reflected, a fraction a will be absorbed and

the remaining part t will be transmitted across the matter, so that:

$$r + a + t = 1 \tag{1.33}$$

These three parameters, that are the reflectivity (r), the absorptivity (a) and the transmissivity (t), are once again a function of wavelength and influence the behaviour of a surface towards incident rays; for example, if $t = 0$ the material is opaque but when $t = 1$ it becomes transparent. The absorptivity is always equal to the emissivity for each wavelength as stated by Kirchhoff's identity. The reflectivity can be affected by surface finishing. Ideally, an incident beam can be reflected uniformly in all directions (diffuse reflection) or with an angle equal to the incident ones (specular reflection). Even if no real surface is either diffuse or specular, the former behaviour is typical of a rough surface while the latter can be observed in polished surfaces.
When two bodies, respectively at temperature T_1 and T_2, exchange energy each other in vacuum, the net heat flux on the surface of body 1 is:

$$Q = \sigma_0 A_1 F_{12} (T_1^4 - T_2^4) \tag{1.34}$$

Here, A_1 is the surface area of body 1 and F_{12} is a factor depending on both the geometric view factor and the emissivity of the surfaces. However, in real applications the radiative heat transfer problem is quite complex. It can involve many surfaces at different non-uniform temperatures that radiate each other with their mutual view factor through a participating media. Materials are far from both a blackbody and graybody. The participating media itself, as the name suggest, can emit and absorb radiation for certain wavelengths as well as can be transparent for others. Moreover, emissivity is not only a function of wavelength and temperature but also of direction. As a result, the radiation beams are characterized more effectively in terms of spectral intensity of radiation $I_\lambda(\theta, \phi)$. It represents, in a spherical coordinate system, the thermal radiation power emitted at the wavelength λ per unit solid angle centered around the direction (θ, ϕ) by a surface of unit area normal to this direction. In addition to $I(\theta, \phi)$, the spectral irradiation G_λ is widely exploited in radiative problems to compute the incident radiation from all the directions and it is defined as:

$$G_\lambda = \int_0^{2\pi} \int_0^{\pi/2} I_\lambda^i(\theta, \phi, \lambda) cos\theta sen\theta d\theta d\phi \tag{1.35}$$

where $I_\lambda^i(\theta, \phi, \lambda)$ is the incident intensity of radiation for a given wavelength per unit area of a surface normal to the direction (θ, ϕ) per unit

solid angle about the same direction.
Dealing with a participating medium, the intensity of radiation of a beam can be attenuated or extinguished travelling along the direction $\vec{\Omega} = (\theta, \phi)$. The decrease of $I_\lambda(\vec{\Omega})$ in an infinitesimal length ds is proportional to the intensity itself, or:

$$dI_\lambda(\vec{\Omega}) = -\beta_\lambda I_\lambda(\vec{\Omega})ds \tag{1.36}$$

The proportionality constant β_λ is the extinction coefficient and represents the energy lost per unit length by the beam. It can be rewritten in the following form:

$$\beta_\lambda = \kappa_\lambda + \sigma_\lambda \tag{1.37}$$

emphasizing the main attenuating mechanisms, that are absorption (κ_λ) and scattering (σ_λ). Even if they can be grouped in Eq. 1.36, these two phenomena lead to different fates for the incoming radiation. Indeed, while absorbed beam energy is converted into internal energy, scattering results in a change of beam direction.
The contributions to the conservation of radiant energy are depicted in Fig. 1.9 for a pencil of radiation with direction $\vec{\Omega}$, length ds and volume dV. The incoming radiation I_λ is intensified by the energy emitted in

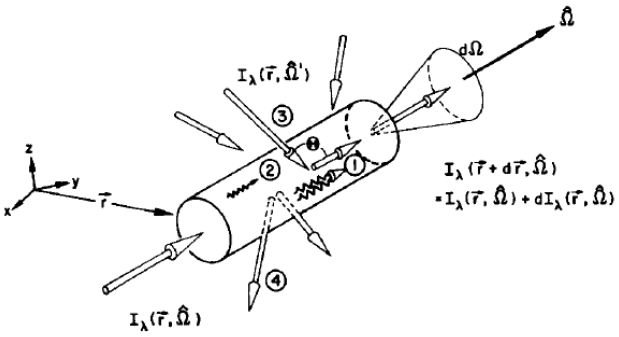

Figure 1.9: Conservation of radiant energy principle [38]

the volume (1) and reduced by the absorbed one (2). Concerning the scattering, beams coming from all the directions can be scattered in the direction $\vec{\Omega}$ increasing I_λ (3). On the contrary, the beam along $\vec{\Omega}$ can change its direction (4), coming out of the I_λ budget. All these four terms act as source/sink terms in the conservation equation for the spectral intensity of radiation $I_\lambda(\vec{r}, \vec{\Omega}, t)$ along a given direction $\vec{\Omega}$, that is the

Radiative Transfer Equation (RTE):

$$\frac{1}{c}\frac{\partial I_\lambda}{\partial t} + \vec{\nabla}\cdot\vec{\Omega} I_\lambda + \beta_\lambda I_\lambda = \kappa_\lambda I_{b\lambda}(T) + \frac{\sigma_\lambda}{4\pi}\int_{\Omega'=4\pi} \psi_\lambda(\vec{\Omega}', \vec{\Omega}) I_\lambda(\vec{\Omega}') d\Omega' \tag{1.38}$$

where the operator $\vec{\nabla}\cdot\vec{\Omega}$ is to denote the projection of divergence operator on the direction $\vec{\Omega}$ and $I_{b\lambda}(T)$ is the blackbody radiation at temperature T. The integral term on the right-hand side represents the scattering from all the directions to $\vec{\Omega}$ and it depends on the phase function $\psi_\lambda(\vec{\Omega}', \vec{\Omega})$, which returns the fraction of energy scattered from $\vec{\Omega}'$ in $\vec{\Omega}$. As the changes in time of I_λ are small for the applications discussed in the present manuscript and the time derivative is divided by the speed of light c, the transient term of Eq. 1.38 can be omitted. To close the problem emissivity and reflectivity properties must be provided at the boundary surfaces.
The RTE is coupled with energy equation through the temperature. Hence, source/sink term of energy in dV due to radiation can be computed in the domain starting from a distribution of I_λ as follow:

$$\dot{\omega}_{rad} = \int_0^\infty \kappa_\lambda [4\pi I_{b\lambda}(T) - G_\lambda] d\lambda \tag{1.39}$$

Here, $\dot{\omega}_{rad}$ is an integral value over the entire solid angle and the spectrum.

1.3 Time scale analysis

In the previous section governing equations of the main phenomena that can be involved in a CHT problem were presented, highlighting the various mechanisms by which thermal energy is generated and transported. The transport properties of the materials as well as the processes themselves determine the thermal response time of the system, leading to a wide range of time scales.
Convection is strongly affected by turbulence in real applications. Eddies have sizes ranging from the Kolmogorov length to the integral length. Each vortex structure transports mass and heat by convection with its own velocity. As a result, at wall the convective heat fluxes fluctuate in the whole turbulence spectrum. The smallest time scales related to the Kolmogorov scale have a key role in the cascade process, influencing the turbulent diffusion of heat in the fluid flow. However, the effects of these scales on metal temperature distribution are moderate. On the other hand, time scales as the integral ones cause the largest temperature fluctuations in the fluid, gaining importance in the transient evolution of

wall temperature. As the integral scales depend on the inlet conditions and geometry of the problem, the characteristic convective time scale can be expressed as:

$$\tau_{conv} = \frac{L}{U} \tag{1.40}$$

where L and U are a reference length and velocity, respectively. In aeroengine burners L is the combustor length and U is the bulk velocity within the flametube. Considering typical order of magnitude for these quantities, that are $L = o(0.1m)$ and $U = o(100m/s)$, τ_{conv} is of the order of 1 ms.
In Section 1.2.1 the dependency of conduction on thermal diffusivity α was emphasized. Unlike convection, now, having to deal with a solid, this transport property determines the speed of heat propagation through the material that is α/L. Using the solid thickness t as reference length, the characteristic conductive time scale is:

$$\tau_{cond} = \frac{t^2}{\alpha} \tag{1.41}$$

Here, reference values for a combustor (i.e. $t = o(1mm)$ and $\alpha = o(10^{-6}m^2/s)$) give τ_{cond} of the order of 1 s. This value is at least two order of magnitude higher than the fluid convective time scale τ_{conv}.
Radiation is an electromagnetic phenomenon, then the beams travel to the speed of light c independently by their wavelength, as shown in Eq. 1.38. Occurring mostly in fluid, the radiative heat transfer is characterized by the same reference length of convective processes. With this assumption, the characteristic radiative time scale is easily expressed as:

$$\tau_{rad} = \frac{L}{c} \tag{1.42}$$

As the speed of light is about $3 \cdot 10^8 m/s$, τ_{rad} is of the order of 1 ps, widely below the Kolmogorov scale of turbulence. If compared with the others heat transfer mechanisms, radiation occurs instantaneously and can be treated as a steady-state process.
Chemical time scales governing a reacting flow differ by many orders of magnitude because combustion involves both slow ($o(1s)$) and fast ($o(10^{-9}s)$) reactions, the former limiting the global speed of the process. In aeroengine combustion regime is identified by $\mathrm{Da} = o(10) - o(10^3)$ and $\mathrm{Ka} = o(10^{-1}) - o(10)$ [47]. A characteristic time scale for combustion can be estimated using the laminar flame speed s_L as reference velocity and

the laminar flame thickness δ_L as characteristic length:

$$\tau_{chem} = \frac{\delta_L}{s_L} \tag{1.43}$$

While $s_L = o(10^{-1}) - o(1)\ m/s$ for aviation fuels, δ_L can be approximated using the mass diffusivity D by the ratio D/s_L and is of the order of $o(10^{-5}) - o(10^{-4})\ m$. Hence, replacing these order of magnitudes in Eq. 1.43 gives a range for combustion time scales of $o(10^{-5}) - o(10^{-3})\ s$ that is smaller than both conduction and convective scales.

1.4 Stability of coupling interface

The physical interface between fluid and solid is characterized by the continuity of energy equation. As heat fluxes and temperature are continuous at the interface, these are the natural quantities to share between the domains. In strong coupling the interface condition is automatically set by the heat balance on control volumes including the interface itself. In loosely coupled approaches, these information must be exchanged between the solvers and applied as boundary conditions, as shown in Fig. 1.10. The choice of strong or loose coupling is not straightforward and it is

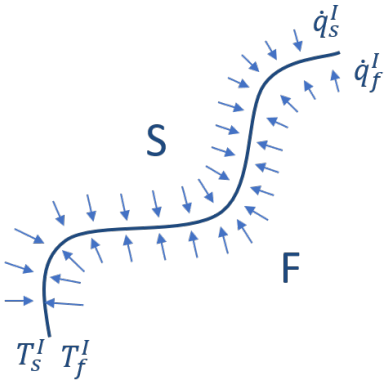

Figure 1.10: Interface quantities in a fluid-solid interaction

worth a deeper discussion.

1.4.1 Strong vs Loose coupling

In the context of Conjugate Heat Transfer problems involved in the present work, conduction is a phenomenon having a weak interaction with the aerothermal field of the flametube core. A direct effect of metal temperature on the gas phase is found only in the near-wall region, where convective heat transfer occurs. This is particularly true dealing with liner walls but in other cases, however, wall temperature can affect the stabilization mechanism of the flame and, then, the combustion process. For instance, in bluff-body stabilized flames the temperature of flame holder can determine flame front positions [48, 49] as well as contribute to blow-off phenomena [50]. Similar effects was found for swirling flames, where the wall heat transfer can modify the flame structure [51, 52], flame dynamics [53] and emissions [54]. On the other hand, radiation has a huge dependency by the aerothermal field but a limited impact on the flow field. Small effects are only due to the redistribution of energy that, however, results in temperature changes of 200 K at most [54, 55].
From a physical and numerical point of view modifications in these phenomena can require several iterations to significantly adjust the different field quantities of the multiphysics problem. For this reason an iteration-by-iteration coupling, as in the strongly coupled approach, could not make sense in many applications and requires a useless computational effort to reach the converged solution of metal temperature. Alternatively, reaching the same final result, the variables can be exchanged every a certain number of iterations to reduce CPU hours: this is the main idea behind loosely coupled methods. Nonetheless, the gain in computational cost is not always justified by the higher complexity, mainly related to the exploitation of a dedicated solver for each physics and a specific procedure, or even code, to couple them.
In addition to considerations about CPU time and the complexity of implementation, a comparison between the methods highlights also differences in the numerical stability. For this purpose, the main finding of the stability analysis carried out by Giles [56] on a simple 1D unsteady thermal diffusion problem are here reported. The governing equation is:

$$\rho c(x)\frac{\partial T}{\partial t} = -\frac{\partial q''}{\partial x} \tag{1.44}$$

where $c(x)$ is the specific heat and q'' is the heat flux, which in absence of convection follows the Fourier's law 1.1. The heat transfer process in a combustor liner is definitely more complex for the presence of different phenomena, as widely explained in Chapter 1. However, in the absence of radiation the wall heat transfer is dominated by diffusive phenomena

not only in the solid but also in the fluid as far as the viscous sublayer is concerned. Eq. 1.44 can be rewritten in the integral from:

$$\frac{d}{dt}\int_{x_1}^{x_2} \rho c T dx = -[q'']_{x_1}^{x_2} \tag{1.45}$$

to solve it similarly to a finite volume method. Considering the conjugate heat transfer between two different materials (i.e. a solid and fluid) with constant properties and the grid depicted in Fig. 1.11 the numerical Fourier number for the generic material d can be defined as:

$$Fo^d = \frac{\lambda_d}{\rho_d c_{pd}} \frac{\Delta t}{\Delta x_d^2} \tag{1.46}$$

where Δt and Δx_d are, respectively, the time-step and mesh element size. In the present problem, Δx_d is uniform in each domain but different sizing can be used in solid and fluid. Eq. 1.45 is discretized using a forward Euler

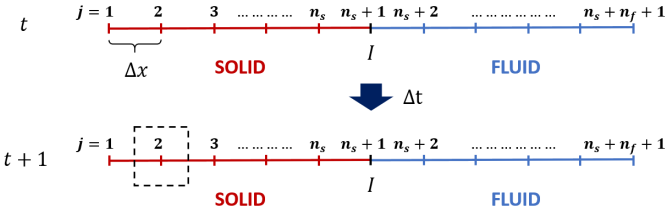

Figure 1.11: Computational grid and time advancement of the domains for the 1D diffusion problem investigated in [56].

scheme in time and a conservative spatial scheme in space, consisting in a heat balance on the length element connecting two neighbouring centroids of the grid elements. As a result the temperature in the j-th interior node is:

$$T_j^{t+1} = bT_{j-1}^t + (1-a-b)T_j^t + aT_{j+1}^t \tag{1.47}$$

At the nodes within each domain the coefficients a and b are:

$$a = b = Fo^d \tag{1.48}$$

At the interface node, instead, these two parameters are:

$$a = \frac{2Fo^f r}{1+r} \quad , \quad b = \frac{2Fo^s}{1+r} \tag{1.49}$$

where r is the ratio of the heat capacities of the computational cells on either side of the interface:

$$r = \frac{\rho_f c_{pf} \Delta x_f}{\rho_s c_{ps} \Delta x_s} \tag{1.50}$$

Following Eq. 1.47 the coefficients on the interior nodes of each domain can be grouped in band square matrices $[(n^d - 1) \times (n^d - 1)]$:

$$M_{ij}^d = \begin{cases} Fo^d & \text{for} \quad j = i - 1 \\ 1 - 2Fo^d & \text{for} \quad j = i \\ Fo^d & \text{for} \quad j = i + 1 \end{cases} \tag{1.51}$$

In addition, interface condition at the node joining the two domain can be represented by a row vector I respecting Eqs. 1.47 and 1.49. Lastly, boundary conditions must be imposed on the first and last grid node (i.e. $j = 1$ and $j = n_s + n_f + 1$ in Fig. 1.11). For fixed temperature or zero heat flux the boundary condition results in a row matrix as:

$$BC_j^d = \begin{cases} [1 \quad 0] \quad \text{that is} \quad T_0^s = T_{bc}^s \quad or \quad q_{bc}^{''f} = 0 \\ [0 \quad 1] \quad \text{that is} \quad T_0^f = T_{bc}^f \quad q_{bc}^{''s} = 0 \end{cases} \tag{1.52}$$

The above defined matrices can be grouped into a unique band square matrix $[(n^s + n^f + 1) \times (n^s + n^f + 1)]$:

$$M_{cht} = \begin{bmatrix} [BC^s] & & 0 \\ [M^s] & & 0 \\ 0 & [I] & 0 \\ 0 & & [M^f] \\ 0 & & [BC^f] \end{bmatrix} \tag{1.53}$$

This matrix depends only on constant parameters as the grid element size, time step size, material properties and boundary conditions. The temperature evolution over time in each point can be solved simply as a matrix product between $[M_{cht}]$ and the temperature vector $[T]^n$ at time step t:

$$[T]^{t+1} = [M_{cht}][T]^t \tag{1.54}$$

The stability in the computation of $[T]^{n+1}$ is driven by the spectral radius $\rho([M_{cht}])$ of $[M_{cht}]$. A stable numerical scheme must satisfy the following constraint:

$$\rho([M_{cht}]) \leq 1 \tag{1.55}$$

As demonstrated in [56] the fully coupled approach is stable if $Fo^d \leq 0.5$, that is the Fourier stability condition related to the time discretization

scheme.
Moving to a loosely coupled approach Eq. 1.47 is still valid for the interior grid nodes of solid and fluid domains. However, at the interface a different condition is required because two separate overlapped nodes are formally used, one for the solid and the other for the fluid. For this reason, Eq. 1.45 at the interface is discretized on a control volume of width $\Delta x^d/2$. In the solid domain the equation becomes:

$$\frac{\rho_s c_{ps} \Delta x_s}{2\Delta t}(T_I^{t+1} - T_I^t) = -q''_w - \frac{\lambda_s}{\Delta x_s}(T_I^t - T_{n_s}^t) \tag{1.56}$$

The heat flux q''_w, specified as interface boundary condition, is computed from the fluid domain as:

$$q''_w = -\frac{\lambda_f}{\Delta x_f}(T_{n_s+2}^t - T_I^t) \tag{1.57}$$

It is worth mentioning that fluid solution can affect the solid temperature by means q''_w, which is the only data coming from the fluid domain. In turn Eq. 1.56 computes the temperature T_I^{t+1} used by the fluid as interface boundary condition for Eq. 1.47. Hence, distinct solvers can be employed for the solution of the two halves, that can run in parallel exchanging q''_w and T_I^{t+1} at the end of the timestep. As shown in Eq. 1.56, the interface temperature is computed by an heat balance on a control volume half the width of the one used in a fully coupled approach, so including only the solid part. Although the form of Eq. 1.47 still represents the row vector I, the a and b parameters must account for the different discretisation and can be expressed as:

$$a = 2Fo^f r \quad , \quad b = 2Fo^s \tag{1.58}$$

Comparing these parameters with Eq. 1.49, in a loosely coupled approach $[M_{cht}]$ tends to the corresponding matrix of a strong coupling if $r << 1$. Indeed, in a strongly coupled algorithm heat capacity of the control volume through the interface becomes influenced mostly by the solid contribution. The numerical stability of the loose coupling scheme is ensured when $Fo^d < 0.5$.
This analysis highlights that the parameter r has a key role in the definition of the requirements for coupling stability. A detailed analysis of this algorithm was reported in [56] using asymptotic solutions and, here, it is summarized for the sake of brevity. When $Fo^d << 1$ the condition $r < 1/Fo^f$ must be satisfied. However, when $r << 1$ the Fourier stability ensures also the coupling stability. On the other hand, when $r >> 1$ the loosely coupled system is unstable. The value of r for which instability

begins is:

$$r_{lim} = \frac{\sqrt{1 - 2Fo^s}}{1 - \sqrt{1 - 2Fo^f}} \tag{1.59}$$

The previous analysis was conducted hypothesizing at the interface a Neumann boundary condition for the solid (i.e. q''_w) and a Dirichlet boundary condition for the fluid (i.e. T_I). Making this choice, the loose coupling will be always stable because the heat capacity of solid is largely higher than the fluid one. Reversing the two BCs, which is equivalent to interchange solid and fluid domain in Fig. 1.11 (i.e. the "f" and "s" subscripts/superscripts in the previous equations), the numerical solution becomes unstable because $r >> 1$. In this case, stability can be recovered using an extremely small time-step in fluid solver such that $Fo^f \leq 1/r$, largely below the needed for Fourier stability.
Time discretization can be explicit or implicit. In the previous analysis the performance of an explicit algorithm were investigated. However, implicit algorithms have interesting stability properties. In [56] a backward Euler discretization is applied on both the strongly and loosely coupled approaches. The former shows an unconditionally stable behaviour related to the absence of Fourier stability limits in implicit algorithms. Once again, the loose coupling is stable if $r << 1$, independently by the Fo^d values, while it is unstable for $r >> 1$. However, large timestep size are allowed by the implicit assumption and $Fo^d >> 1$. Under these conditions, the stability limit is:

$$r < \sqrt{\frac{Fo^s}{Fo^f}} \tag{1.60}$$

or:

$$\frac{(\rho_f c_{pf})^3 \Delta x_f^4}{\lambda_f} < \frac{(\rho_s c_{ps})^3 \Delta x_s^4}{\lambda_s} \tag{1.61}$$

Concerning the choice of boundary conditions, comments similar to explicit time discretisation can be made and the Neumann type for solid and Dirichlet type for fluid are preferred for stability reasons.

1.4.2 Synchronization of the solvers

In the context of unsteady loosely coupled approaches one of the main problems to be addressed is the time-advancement of the involved solvers. In the stability analysis reported in [56] (see Section 1.4.1) the solvers are kept synchronized in time or, in other words, communication occurs at the end of time-step, whose size is the same in solid and fluid domains. In CFD applications this solution strategy is infeasible because of the

different time scales and the CPU time required to solve the fluid flow. An effective technique is to desynchronise the solvers [31] as shown in Fig. 1.12 that, however, strongly modifies all the terms in Eq. 1.54 and, in turn, the stability properties of the loose coupling.

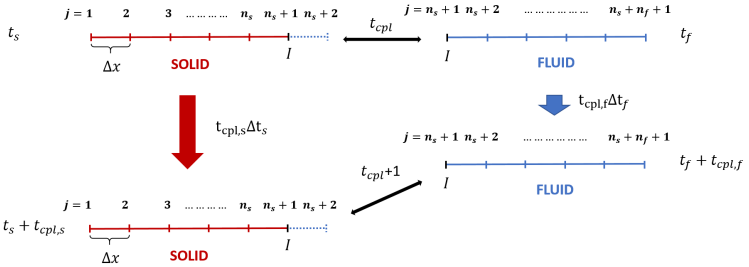

Figure 1.12: Computational grid and time advancement of the domains for the 1D diffusion problem with desynchronization of time steps.

The time advancement in the interior nodes is still governed by Eq. 1.47, where t_s and t_f are used in place of t, representing the time step of solid or fluid respectively. Hence, the two solvers run in a segregated manner solving the following system:

$$[T_d]^{t_d+1} = [M^d_{ht}][T_d]^{t_d} \tag{1.62}$$

where $[M^d_{ht}]$ is the matrix representing heat transfer within the domain "d" and $[T_d]$ is the vector of temperature at the grid nodes. At interface in solid domain Eq. 1.56 is slightly different:

$$T^{t_s+1}_{I,s} = T^{t_s}_{I,s} - 2Fo^s(T^{t_s}_{I,s} - T^{t_s}_{n_s}) + 2\frac{\Delta t_s}{\Delta t_f} rFo^f(\tilde{T}^{t_{cpl}}_{n_s+2} - \tilde{T}^{t_{cpl}}_{I,f}) \tag{1.63}$$

In addition to the temperatures at solid nodes, the $[T_s]$ vector must contain $\tilde{T}$, which is kept constant during the solid computation and updated by the fluid solver at the coupling iteration t_{cpl} such that:

$$T_s = \begin{bmatrix} T_0 & T_1 & ..... & T_{I,s} & \tilde{T}_{I,f} & \tilde{T}_{n_s+2} \end{bmatrix} \tag{1.64}$$

The segregated computation of this new domain including the solid and a thin fluid layer is therefore characterized by a constant heat flux imposed

by the temperatures $\tilde{T}$. The resulting $[M^s_{ht}]$ is:

$$M^s_{ht} = \begin{bmatrix} [BC^s] & 0 & \\ [M^s] & 0 & \\ 0 & [I_s] & \\ 0 & 1 & 0 \\ 0 & & 1 \end{bmatrix} \tag{1.65}$$

where the interface row vector $[I_s]$ can be derived from Eq. 1.63. In the fluid domain Eq. 1.47 is valid for all the interior nodes while at the interface node a fixed temperature boundary condition is applied, whose value is kept constant during the fluid coupling iteration, or:

$$T^{n_f+1}_{I,f} = \tilde{T}^{n_{cpl}}_{I_f} \tag{1.66}$$

Now, for the fluid, the vector $[T_f]$ of temperatures and the matrix $[M^f_{ht}]$ of the heat transfer are, respectively:

$$T_f = \begin{bmatrix} \tilde{T}_{I,f} & T_{n_s+2} & ..... & T_{n_s+n_f+1} & T_{n_s+n_f+2} \end{bmatrix} \tag{1.67}$$

and:

$$M^f_{ht} = \begin{bmatrix} 1 & 0 \\ [M^f] & 0 \\ 0 & [BC^f] \end{bmatrix} \tag{1.68}$$

The application of $[M^d_{ht}]$ on $[T_d]^{t_d}$ (i.e. Eq. 1.62) must be repeat for the number of inter-coupling iterations, that is $t_{cpl,d}$ times. The powered matrices can be assembled in a unique matrix M_{ass} as:

$$M_{ass} = \begin{bmatrix} [M^s]^{t_{cpl,s}} & 0 \\ 0 & [M^f]^{t_{cpl,f}} \end{bmatrix} \tag{1.69}$$

A new matrix M_{cpl}, however, is required to update the boundary temperatures and heat flux at the interface side of the halves, so restoring the coupling. This matrix is defined as:

$$M_{cpl} = \begin{bmatrix} [1]_s & 0 & 0 \\ 0 & [U] & 0 \\ 0 & & [1]_f \end{bmatrix} \tag{1.70}$$

The identity matrices $[1]_s$ and $[1]_f$ are of $(n_s \times n_s)$ and $(n_f \times n_f)$ size, respectively. The matrix $[U]$ of (3×5) size is devoted to the updating of the temperatures $\tilde{T}$.
The solution of a 1D CHT problem using a loosely coupled approach

with separate timesteps for solid and fluid is summarized by the following matrix form:

$$\begin{bmatrix}[T_s]\\[T_f]\end{bmatrix}^{t_{cpl}+1} = [M_{cpl}][M_{ass}] \begin{bmatrix}[T_s]\\[T_f]\end{bmatrix}^{t_{cpl}} \tag{1.71}$$

This equation is similar to Eq. 1.54 but now the temperature array advances at the coupled timestep. Moreover, in Eq. 1.71 $[M_{cht}] = [M_{cpl}][M_{ass}]$ depends on the number of sub-iterations $t_{cpl,s}$ and $t_{cpl,f}$ which, therefore, can affect the numerical stability.
It is worth emphasizing from Eq. 1.63 that the desynchronisation technique is practically equivalent to a scaling of solid heat capacity $\rho_s c_{ps}$ by a factor $f = \Delta t_s/\Delta t_f$ in the synchronised case because the matrix coefficients do not change.

1.4.3 Interface boundary conditions

Three types of boundary conditions are commonly employed in CHT simulations, that are:

- Dirichlet condition

$$T_I = T_{bc} \tag{1.72}$$

- Neumann condition

$$q''_I = -\lambda \left.\frac{\partial T}{\partial n}\right|_I = q''_{bc} \tag{1.73}$$

- Robin condition

$$q''_I + \alpha T = Q_{bc} \tag{1.74}$$

The Robin boundary condition is a linear combination of the others and can be regarded a generalization of Eqs. 1.72 and 1.73. The positive weighting coefficient α $[Wm^{-2}K^{-1}]$ is the coupling relaxation parameter that has a key role on the stability of coupling and convergence rate. On the fluid side Eq. 1.74 becomes:

$$q''_f = -q''_s + \alpha_s(T_f - T_s) \tag{1.75}$$

and similarly for the solid side:

$$q''_s = -q''_f + \alpha_f(T_s - T_f) \tag{1.76}$$

When $\alpha = 0$ Eq. 1.73 is obtained whereas Eq. 1.72 can be derived setting $\alpha = \infty$.
In terms of boundary pair at interface the mixed boundary conditions are usually preferred for CHT computations. However, the combinations are not all stable. The solid Dirichlet/fluid Neumann pair is unstable because does not satisfy the Giles' condition [56], as shown in Section 1.4.1.
Most CFD codes provide the convective heat transfer boundary condition:

$$q_s^{''I} = HTC(T_{ref}^I - T_s^I) \tag{1.77}$$

where T_{ref}^I is a reference temperature at interface and T_s^I is the interface temperature on the solid domain. Eq. 1.77 is a particular case of the Robin boundary condition [57] with:

$$HTC = \alpha_f \quad , \quad T_{ref}^I = -\frac{q_f^{''I}}{\alpha_f} + T_f^I \tag{1.78}$$

For this reason, here the focus is on the solid Robin/fluid Dirichlet pair. The parameter α_f affects stability of the CHT algorithm, both in steady and transient simulations. In a steady approach the convergence rate of interface temperature on fluid side is related to the chosen α_f as [58]:

$$T_f^{I,n} = T_f^{\infty} + \left[\frac{\tilde{B}i - Bi}{\tilde{B}i + 1}\right]^n \Delta T_0 \tag{1.79}$$

Here, the physical Biot number Bi and the numerical Biot number $\tilde{B}i$ are defined, respectively, as:

$$Bi = \frac{hL}{\lambda_s} \tag{1.80}$$

and:

$$\tilde{B}i = \frac{\alpha_f L}{\lambda_s} \tag{1.81}$$

whereas temperature difference ΔT_0 represents the initialization error. Eq. 1.79 highlights that stability can be ensured if:

$$\left|\frac{\tilde{B}i - Bi}{\tilde{B}i + 1}\right| < 1 \tag{1.82}$$

corresponding to the blue areas in Fig. 1.13. A value of this function close to zero can speed up the convergence of a CHT problem. However,

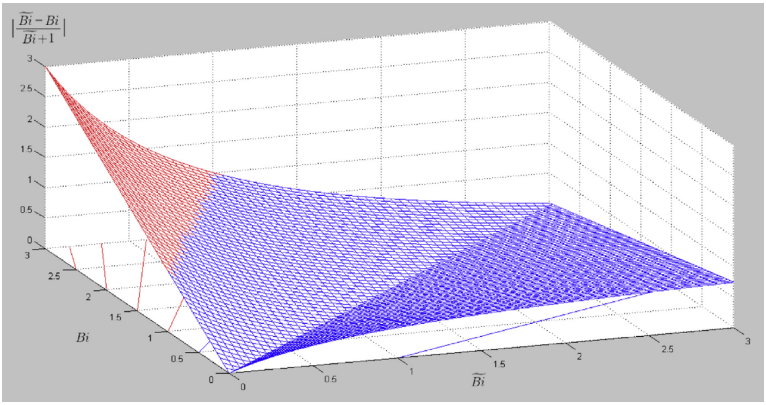

Figure 1.13: Stability domain in the steady CHT as function of Bi and $\tilde{Bi}$ [57]

according to Eq. 1.81 the coupling relaxation parameter must satisfy:

$$\alpha_f > \frac{h}{2} - \frac{\lambda_s}{2L} \tag{1.83}$$

Hence, the choice of α_f is not arbitrary and depends on the solid characteristics (λ_s and L) as well as the flow field (h). For the convective boundary condition the lower the α_f, the lower changes in temperature during one iteration because it acts relaxing the heat flux computed by the fluid, as shown in Eq. 1.76.
Stability analysis of the convective boundary condition on unsteady calculation was carried out in [59] for the 1D Giles' problem. The interface row vector $[I_s]$ of matrix M^s_{ht} in Eq. 1.65 must satisfy the convective formulation, including the parameters α_f and T_{ref} that are introduced as follow:

$$\left[Fo_s \quad 1 - Fo_s(1 + \tilde{Bi}_{\Delta x}) \quad Fo_s\tilde{Bi}_{\Delta x} \quad \frac{Fo_s\tilde{Bi}_{\Delta x}}{\alpha_f}\right] \tag{1.84}$$

where $\tilde{Bi}_{\Delta x}$ is the numerical Biot number based on the element size Δx_s. The vector of temperatures $[T_s]$ is modified according to the new boundary condition and the $\tilde{T}$ values are replaced by the variables q''_f and T_f of Eq. 1.76. The stability region of matrix $[M^s_{ht}]$ and, therefore, of solid computation depends on the choice of both Fo_s and $\tilde{Bi}_{\Delta x}$. Fig. 1.14 shows the stability region of $\tilde{Bi}_{\Delta x}$ as function of the Fo_s using an

explicit algorithm. Hence, chosen Fo_s the $\tilde{Bi}_{\Delta x}$ must be kept below a

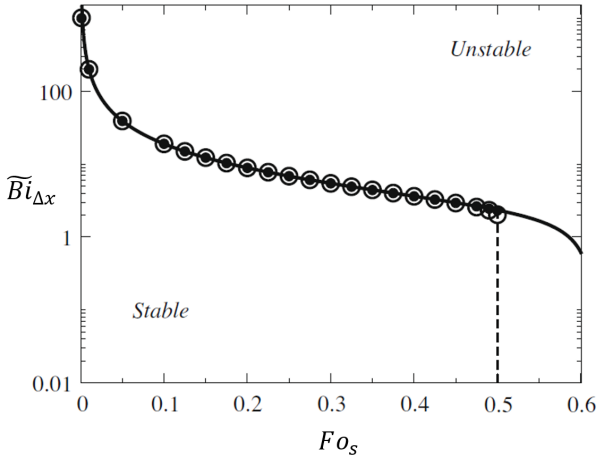

Figure 1.14: Stability region of matrix $[M^s_{ht}]$ as a function of the numerical Biot number $\tilde{Bi}_{\Delta x}$ and the Fourier number Fo_s [59].

threshold value. The curve suggests that a reduction in time step size allows higher values for the coupling relaxation parameter. Indeed, even if higher changes in solid temperature would be permitted by the boundary condition, these are limited by the smaller time step in any case. Even if intrinsic stability of M^f_{ht} does not change from Section 1.4.2 because of the same interface condition, the stability of M_{ass} is affected by α_f as well as $t_{cpl,s}$ and $t_{cpl,f}$ (see Eq. 1.69). Given the timescale τ_d and the time-step Δt_d for each domain d, if the number of iterations is expressed as:

$$t_d = \alpha_t \frac{\tau_d}{\Delta t_d} \tag{1.85}$$

the M_{ass} becomes a function of α_f and α_t, where α_t is the coupling synchronization time parameter that is equal for both the domains. Making this assumption, stability region for the coupling procedure can be depicted as in Fig. 1.15. Two stability limits are established for the numerical Biot number: a constant upper limit and a lower limit depending on the α_t value. For definitely small coupling synchronization time parameter, only the upper limit is present and the $\tilde{Bi}_{\Delta x}$ can be lowered. Indeed, a small α_t leads to a more frequent coupling that improves stability range.

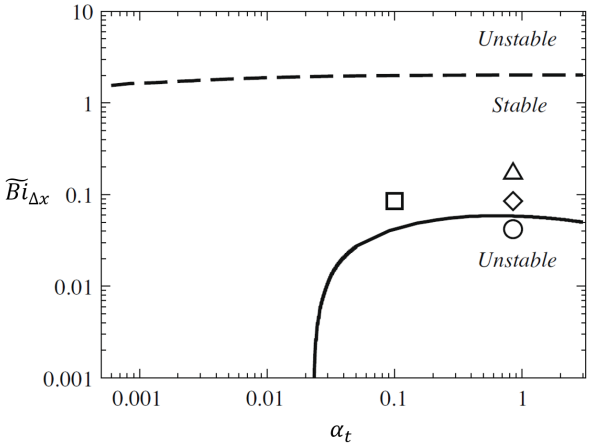

Figure 1.15: Stability map of matrix $[M^s_{cht}]$ as function of coupling relaxation parameter α_t and numerical Biot number $\tilde{B}i_{\Delta x}$ [59]

1.4.4 Penetration depth and aliasing

In Section 1.4.2 the benefits of a desynchronisation of time steps on loosely coupled approaches were stressed, especially concerning the speed-up of solution convergence. The communication between the solvers is a sampling process of fluid heat flux and solid wall temperature. These quantities are mapped on a different time line. For instance, changes in heat flux on fluid domain are viewed by the solid as an apparent (smaller) frequency relying on the following scaling rule:

$$f_s = \frac{1}{a}\frac{\Delta t_f}{\Delta t_s} f_f \tag{1.86}$$

where $a = n_s/n_f$ is the acceleration parameter. As a result, numerical issues must be faced that are unphysical penetration depth and aliasing. Penetration depth is defined as the length for which the amplitude of a sinusoidal forcing signal of temperature at wall decays of 99% crossing the solid thickness. Solving for this problem the 1D version of Eq. 1.2 without heat source terms, the temperature distribution is derived [31]:

$$T(x,t) = \Delta T e^{-\sqrt{\frac{\omega}{2\alpha}}x} cos\left(\omega t - \sqrt{\frac{\omega}{2\alpha}}x\right) \tag{1.87}$$

where ΔT is the amplitude of the input signal and ω is its pulsation. This expression highlights that the frequency of the signal is preserved but the amplitude is exponentially damped moving through the solid. Moreover, the higher the frequency, the stronger the damping of an input signal, as shown in Fig. 1.16. Eq. 1.87 can be used to derive the penetration

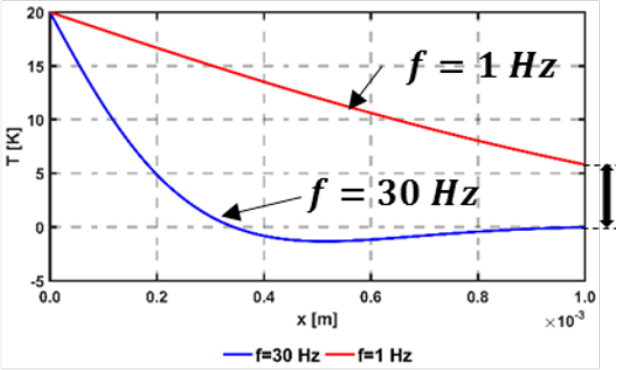

Figure 1.16: Decay of temperature amplitude in the solid thickness for two different frequencies of the input signal.

length, that is:

$$x_{1\%} = ln(100)\sqrt{\frac{2\alpha}{\omega}} \tag{1.88}$$

Unfortunately, the forcing frequency of the solid is enlarged by the desynchronisation for a loosely coupled problem, causing the overprediction of penetration depth. This is one of the reasons leading this kind of approaches suitable only for quasi-steady solutions. However, these unrealistic oscillations can provide a wrong prediction also for the mean temperature if they affect the flow field as for thin solid.
Aliasing, instead, is a direct consequence of bad sampling. Considering the simple 1D problem of a thermal capacitor heated through convection by a fluid with pulsating temperature of amplitude T_{fluc}:

$$q''(t) = H_c(T_f(t) - T_s(t)) \tag{1.89}$$

The analytical solution of the problem is [31]:

$$T_s(t) = (T_{s0} - T_{f0} - \frac{T_{fluc}}{1+\omega_0^2\tau^2})e^{-\frac{t}{\tau}} + \frac{T_{fluc}}{\sqrt{1+\omega_0^2\tau^2}} cos(\omega_0 t - arcsin(\frac{\omega_0\tau}{\sqrt{1+\omega_0^2\tau^2}})) + T_{f0} \tag{1.90}$$

where $\tau = \rho c_{ps}/H_c$. The temperature fluctuation is damped by the solid that acts as a low pass filter. However, if the same problem is solved in a discrete fashion as for loose coupling, the convective flux is kept constant for a certain time interval depending on the coupling frequency [31]. As in the sampling theory, the results of Nyquist-Shannon theorem should be taken into account, which states sampling frequency must be at least twice the signal frequency to avoid aliasing. This issue can appear in loosely coupled approaches because if the coupling frequency is not small enough, some relevant flow instabilities are sent to solid solver with a lower frequency. At worst, an unfortunate sampling frequency not respecting Nyquist-Shannon theorem can affect also the final wall temperature, as shown in Fig. 1.17. A possible criteria for the choice of coupling frequency

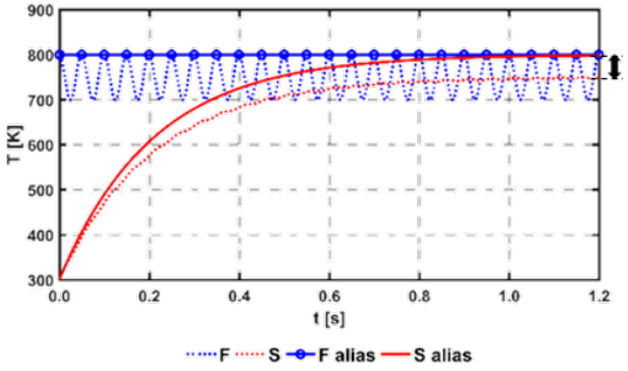

Figure 1.17: Example of undesirable aliasing on fluid temperature (blue) that makes a wrong prediction of solid temperature (red).

is to keep the most energy-carrying frequencies, as shown in Fig. 1.18 for a polychromatic spectrum representative of a combustion chamber. High coupling frequencies f_{cpl} preserve the spectrum shape as aliasing occurs only on the highest frequencies that, anyway, are poorly energy-

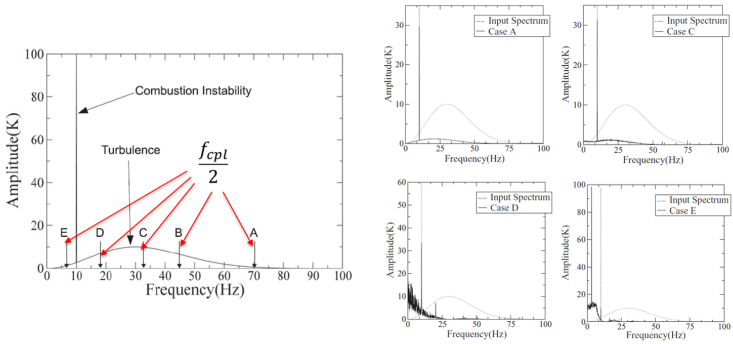

Figure 1.18: Spectrum of solid temperature for different sampling frequencies on the spectrum of fluid temperature[31]

carrying. On the other hand, when f_{cpl} is moved below the frequency of the combustion instability, the whole heat transfer spectrum is shifted towards lower frequencies. As a results, these aliased frequencies, being able to penetrate deeply in the solid, make the solutions unrealistic.
In conclusion, the choice of coupling frequency should be a compromise between computational cost and accuracy, this last obtained limiting the undesirable aliasing and unrealistic penetration depth for the characteristic frequencies of the investigated problem.

1.5 State of the art on unsteady CHT modelling

During the past decades several approaches have been developed to solve transient CHT problems.
Duchaine et al. in [59] proposed a methodology to solve LES-CHT simulations on massively parallel architectures. As shown in Fig. 1.19 it relies on the desynchronisation technique for a parallel coupling strategy. Mixed Dirichlet/Neumann boundary conditions provide a stable coupling at a constant frequency, leading this method suitable for the prediction of steady state metal temperature. The AVBP [60] and AVTP codes are used as fluid and solid solvers, respectively. The codes are coupled with the OpenPALM software [61], a general tool managing almost all the aspects of the coupling. It distributes the CPU between the solvers to optimize the computational resources and limit the queue time. Moreover, it exploits an efficient client-server mechanism to directly exchange the

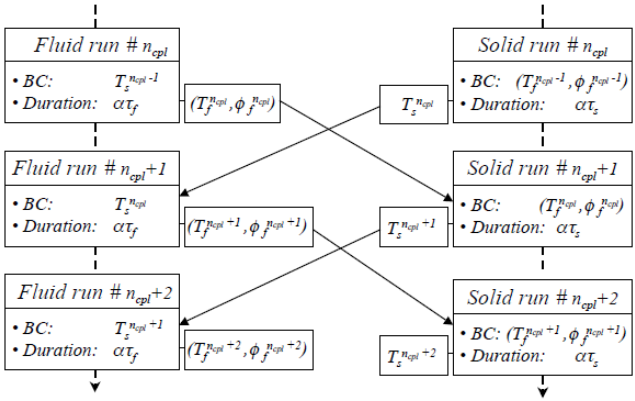

Figure 1.19: Parallel coupling strategy adopted in [59]

interface data between the communicating partitions of the solvers. To preserve the value of fields at the interface when different meshes are adopted, appropriate interpolation scheme are provided. The procedure was successfully applied on a turbine blade, where a sensitivity analysis on both the coupling relaxation parameter and coupling synchronization time parameter is presented. The same strategy was adopted in [62] to solve the CHT problem on a reverse flow RQL combustor. Here, a radiative solver exploiting the DOM model was added and coupled to both the solid and fluid.

He et al. in [63] illustrate a method to solve unsteady CHT problems based on a time-scale decomposition of the near-wall fluid temperature. The mean value is used to solve the steady conduction problem in the solid. Fluctuating component, instead, is decomposed in its harmonics using a Fourier transform. The pairs amplitude-frequency thus obtained are required by a semi-analytical interface model to compute the wall temperature in the spectral domain. This model is obtained by conservation of energy at the interface, where heat fluxes are derived by the flow field solution for the fluid side and by an analytical 1D solution of conduction in a semi-infinite domain for the solid side. The resulting wall temperature is transformed in the time domain, summed to the mean value provided by the steady solid solver and applied as time-dependent interface boundary condition for the fluid side. If the unsteady temperature field within the

solid is desired, the same wall temperature spectrum can be adopted as boundary condition for the unsteady conduction problem. This approach was demonstrated for a turbine cascade subject to inlet unsteady hot streaks using URANS [63] and natural convection problems using URANS [64] as well as LES [65].
Koren et al. in [32, 55] developed a different coupling procedure to simulate multiphysics problems involving turbulent reacting flow, radiative heat transfer and wall heat transfer. As in [59], these phenomena are solved on different solvers following the scheme depicted in Fig. 1.20 and the data exchange is performed through the coupling library OpenPALM. Unlike the previous approach, the application of an Hybrid-Cell interface

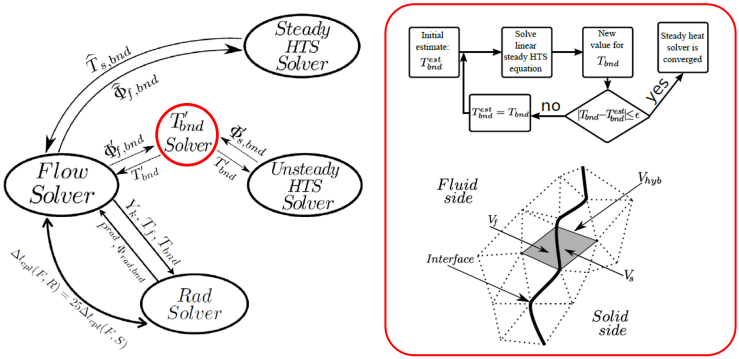

Figure 1.20: Solution strategy adopted in [32] with focus on the interface fluctuating temperature

model ensures the energy conservation. Indeed, it solves in a dedicated ODE solver the energy balance equation on an hybrid cell around the interface composed by the first cell layer of fluid and solid meshes. The resulting interface temperature is set as Dirichlet boundary condition on both the domains. The interface solver is aided by a PID controller that dynamically adjusts the coupling time step size to keep the numerical integration error of the ODE below a threshold value. For obvious reasons this method, called Hybrid-Cell Neumann-Dirichlet (HCND), is not compatible with the desynchronization technique. To have a solution in an affordable computational time, the superposition of both steady (for mean value) and unsteady (for fluctuating component) solid solvers are exploited to predict the transient evolution of wall temperature. The steady Heat Equation requires the mean wall heat flux as interface boundary condition

from the unsteady fluid solver and provides the mean temperature. On the other hand the unsteady solid solver exploits the fluctuating component of the wall temperature returned by the HCND method using the fluctuating wall heat fluxes. The main advantage of this approach is the acceleration of the transient temperature to a permanent regime. Indeed, the mean wall heat flux is not yet converged during the first coupling steps because the data are averaged over a small time and, then, affected by the fluctuating fluxes. As a result, the highest frequencies are not filtered by the meaning process and are treated in a quasi-steady fashion by the steady solid solver.

1.6 Modelling strategies for multi-perforations

Conjugate Heat Transfer applied to turbomachinery is a multiscale problem, in the sense of both time and space scales. Indeed, in addition to the wide range of time scales involved for the multiphysics nature of the problem, the small geometrical features related to the cooling system create a huge disparity in spatial scales. This is particularly evident for effusion cooling of combustor liner, where the hole diameter is around three orders of magnitude below the combustor size. From a numerical perspective the solution of the flow field within thousands effusion holes is infeasible, especially as far as Scale Resolving Simulation is concerned. Nevertheless, this full-coverage film cooling can affect the mainstream, the combustion process, the gas temperature and, above all, the metal temperature distribution. Hence, several approaches have been developed to treat effusion cooling with different levels of accuracy and computational costs, trying to replicate the exchange of momentum and energy with the hot gases as well as the heat sink effect on the solid.
A first interesting approach is the Homogeneous Model (HM) [66]. It applies an homogeneous boundary condition over the entire multi-perforated surface that must satisfies the global momentum fluxes as well as the mass flow rate of the discrete perforation. On the injection side an inlet boundary condition is set, where the normal component of velocity is scaled by the reciprocal of porosity to ensure the real mass flow rate through the perforation. This assumption does not respect the momentum flux on the normal direction which, however, is dominated by the pressure term that limits the negative impact of this discrepancy. Concerning the preservation of streamwise momentum flux, the tangent of the injection angle must be scaled again by the porosity. On the suction side an outlet boundary condition is required. Here, an equivalent formulation is made for the normal momentum flux whereas an equilibrium assumption on the

near-wall cell is made concerning the streamwise momentum flux. Local coolant flux is computed from the pressure drop across the liner, once the discharge coefficient and the geometrical characteristics of the perforation are chosen. The homogeneous model was developed to solve adiabatic simulations including the effects of effusion cooling on the mainstream. Indeed, replacing walls with inlet/outlet boundary conditions, the original model is not suitable for conjugate heat transfer. In [67], however, the heat transfer coefficient is locally computed using the Cottin's correlation [68] that, together with the adiabatic wall temperature provided by the first node value, are send to the conduction solver for the prediction of metal temperature.
Despite the low computational cost, the Homogeneous Model is not able to properly predict the mixing close to wall. Moreover, the model does not benefit of Scale Resolving Simulations for the resolution of wall macro-mixing because a smaller size of the mesh elements has not effects on the model. An evolution of HM is the Thickened-Hole Model (THM) [69]. It employs a distribution function to limit the application of HM on the faces around the hole centroid. On the remaining faces a wall law model is applied. This particular thickening of the holes can take into account of flow disuniformities generated by effusion jets without the need of extremely fine meshes. Obviously, as shown in [69], decreasing the thickness factor together with a finer wall discretisation improve the prediction of both the mean and root mean square values of the quantities. As a result the THM model takes advantage in the combustor design from its mesh independent behaviour in the testing of different multi-perforated geometries on the same liner using a unique mesh. Application of this methodology can be found in [70, 71].
Heterogeneous models relying on imprinted effusion was developed in [72, 73], where the effusion orifices are eliminated to avoid an inaccurate flow resolution because of the difficulties in their proper discretisation. Hence, only the imprinted inlet/outlet faces are kept, dramatically reducing the computational effort. In [72] the methodology was applied to the RANS and LES adiabatic calculation of a through flow and reverse flow combustor. Mass flow rate within the hole is computed locally using a correlation for discharge coefficient that depends on the flow conditions at the imprinted faces and probing the pressure drop close to inlet/outlet boundaries. In [73] the approach was extended to account for heat sink effect within the holes.
Source-based models are the most intuitive to include the energy removed from the solid by the coolant. In [74] point source/sink terms were applied also to the main flow quantities (i.e. mass, momentum, temperature and

turbulence) in order to model injection/aspiration phenomena. All the source values were set according to a preliminary detailed simulation or correlations. To recover solution-dependent values, in [75] the mass flow rate was computed similarly to [74] while a correlation for Nusselt number was required for the heat sink. Distributed mass sources, instead, were applied in [76] within a group of cells on the injection side. In particular, in [76] the CFD solver was coupled with external tools to estimate the change in coolant properties through the hole. In [77] the PAPRICO model was developed in ANSYS Fluent and exploited on the adiabatic RANS simulation of a combustor liner. It applies source terms on the inlet/outlet cells similarly to [76] and includes an automatic parallel search algorithm for the holes.

1.7 Concluding remarks

The present chapter has highlighted the key aspects of Conjugate Heat Transfer on combustor liners, that must be extended to the more general perspective of multiphysics heat transfer. The problem has been analysed focusing on the different requirements for the involved phenomena, mainly concerning time and space resolution. In particular, the large time scale disparities make loosely coupled approaches the only affordable ones in the context of scale-resolving simulations which are increasingly exploited to have a deeper insight of the complex reacting flow field and improve the accuracy of results. Several numerical issues at the coupling interface have been faced up ranging from the choice of boundary conditions to the frequency of data communication. The main solutions available in literature have been presented to deal with unsteady CHT and multiperforated liners, being relevant components of the U-THERM3D approach. The tool in question aims to be an ANSYS Fluent-based framework as general as possible to exploit the predictive capabilities of scale-resolving simulations in the high-fidelity design of combustor liners and will be described in the next chapter. In the present work, in particular, U-THERM3D will be applied as a common framework for the modelling strategy for turbulent spray flames developed by Puggelli in [78] and the steady loose coupling approach for Conjugate Heat Transfer developed by Mazzei [79].

Chapter 2

Numerical modelling of multiphysics heat transfer

Heat transfer from a multiphysics perspective requires to model different interacting phenomena as widely discussed in the previous chapter. Here, the models employed in this manuscript and the proposed framework for their coupling will be presented and the main tasks will be validated.

2.1 U-THERM3D tool

In the past years, a 3D coupled approach for the thermal design of combustor liners, called THERM3D, was developed by Mazzei [79] for steady applications which will be briefly presented in Section 4.2. Such a tool was exploited as a starting point for the present work, that has the objective of developing a coupling code in ANSYS Fluent to solve conjugate heat transfer in the context of an unsteady multiphysics problem.
The basic idea behind U-THERM3D procedure is a desynchronisation of time steps in the solution of the involved phenomena, that can be summarized in convection (including several sub-phenomena as combustion, spray evolution etc.), conduction in the solid and radiation. Each of them is solved in a dedicated simulation, running with a parallel coupling strategy. As in [59], instantaneous values are exchanged at the coupling iteration and consist of surface quantities for the solid-fluid and solid-radiation interactions whereas volume quantities for the fluid-radiation coupling. The procedure used in U-THERM3D is depicted in Fig. 2.1. The CFD and conduction solvers advance in time with their own time-step. As far as radiation is concerned a steady solver is exploited because of the

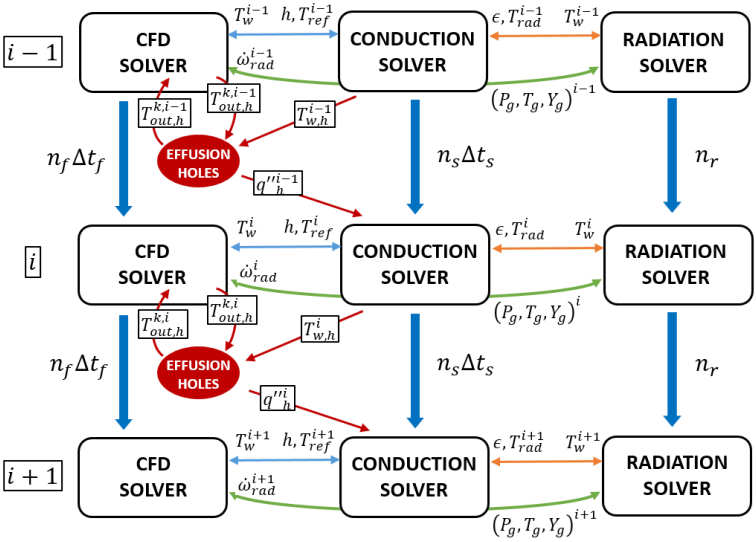

Figure 2.1: U-THERM3D parallel coupling strategy

extremely small time scales (see Section 1.3). Convective and radiative wall heat fluxes are manipulated before sending them to the conduction solver. Convective heat fluxes at fluid-solid interfaces are converted into the more stable convection boundary condition:

$$q''_{conv} = h(T_{ref} - T_w) \tag{2.1}$$

where h is a coupling relaxation parameter and T_{ref} is a reference temperature respecting wall heat flux computed in fluid solver. Concerning radiation, a black-body model is employed, so that:

$$q''_{rad} = \sigma_0(T_{rad}^4 - T_w^4) \tag{2.2}$$

Consequently, the computation of radiative gas temperature T_{rad} is required in order to set the radiative heat fluxes provided by the dedicated simulation. On the other hand, wall temperature is used as Dirichlet BC by flow and radiative field computations, then transferred to their respective solvers. Even though the employed mixed Dirichlet-Robin BC does not ensure a conservative behaviour at the interface, it provides a

stable coupling. The inaccuracies, however, are definitely below the global error of the methodology if a high coupling frequency is set. Radiation solver requires some field variables from the CFD solver, that are gas pressure, temperature and composition. The resulting energy source due to absorption and emission phenomena is returned to the flow field computation.
User Defined Functions were written to handle the synchronisation of the solvers as well as, together with Scheme scripts, to exchange interface data.

2.1.1 Effusion holes solver

In addition to the three solvers, a dedicated tool for the calculation of effusion holes is coupled, relying on the imprinted technique. The orifices are replaced by inlet/outlet boundaries as sketched in Fig. 2.2. A UDF

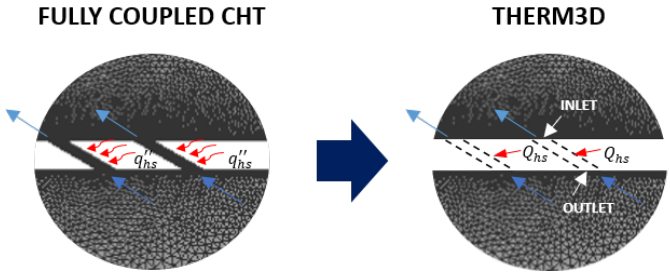

Figure 2.2: Sketch of the effusion holes modelling.

computes gas temperature at the outlet boundary, so taking into account of heat sink effect by means of the Eq. 2.3:

$$Q_{EFF} = HTC \times A_h \times (\bar{T}_{w,h} - \bar{T}_f) \tag{2.3}$$

where A_h is the hole wetted area, $\bar{T}_{w,h}$ is the mean hole wall temperature, $\bar{T}_f$ is the mean inlet/outlet coolant temperature and HTC is the Heat Transfer Coefficient, evaluated in terms of Nusselt number Nu_D with the Gnielinski correlation [80] as:

$$Nu_D = \frac{(f/2)(Re_D - 1000)Pr}{1 + 12.7(f/2)^{1/2}(Pr^{2/3} - 1)}[1 + (\frac{D}{l})^{2/3}] \tag{2.4}$$

where Re_D is the Reynolds number based on hole diameter D, l is the hole length and f is the Fanning friction factor that depends on Re_D:

$$f = [1.58ln(Re_D) - 3.28]^{-2} \tag{2.5}$$

Flow rate through each hole is imposed as boundary condition and can be computed by a flow network solver as well as by a resolved simulation, chosen by a flow split assumption or dependent by the local pressure drop and discharge coefficient. The inlet temperature is given back to the UDF in order to compute a mean gas temperature into the holes for molecular properties estimation.

2.1.2 Efficiency in High-performance Parallel Computing

The present approach shows the best performances in massively parallel computing. For this reason it is suitable in the prediction of the complex thermal interactions within gas turbine combustors. Nonetheless, a good balancing in terms of CPU is required between the involved solvers to minimize the queue time and, therefore, the waste of computational resources. This goal is pursued with a synchronization in CPU time in place of physical time.
Given a certain number of processors P, a fully coupled approach uses all the available resources to solve the complete set of equations. On the other hand, in a loose parallel coupling a portion of the total processors is devoted to solve only the equations modelling the investigated phenomenon. In a convective-conduction problem, for instance, hypothesizing a perfect scaling for both the solvers, load balancing requires that the processors P_f and P_s assigned to fluid and solid computations, respectively, must be such that [59]:

$$\frac{\mathrm{T}_f}{P_f + P_s} = \frac{P_f}{P} = \frac{1}{1 + \frac{\mathrm{T}_s}{\mathrm{T}_f}} \tag{2.6}$$

Here, T_f and T_s are the execution times of the fluid and solid solvers on one processor to compute physical times $\Delta\tau_f$ and $\Delta\tau_s$, respectively.
A deeper analysis to quantify the advantages in terms of saved computational resources can be performed for the present methodology. In the following I_x is the execution time of one time step of the "x" solver on a single grid element exploiting a single processor whereas $N_{el,x}$ is the corresponding number of elements. Given a CHT problem involving convection (f), radiation (r) and conduction (s), a strongly coupled approach

would require an execution time ΔT_{cht} estimated as:

$$\Delta T_{cht} = \frac{\Delta\tau_{max}}{\Delta t_{min}} \frac{N_{el,f}(I_f + n_{r,cht} I_r) + N_{el,s} I_s}{P} \tag{2.7}$$

where $n_{r,cht}$ represents the number of iterations in a fluid time step for the radiative computation and it is introduced because radiation is solved in a steady fashion unlike the other solvers. The maximum physical time $\Delta\tau_{max} = max(\Delta\tau_f, \Delta\tau_r, \Delta\tau_s)$ is driven by the solid. The minimum time step $\Delta t_{min} = min(\Delta t_f, \Delta t_s)$, instead, is limited by the fluid solver.
Moving to the U-THERM3D approach, the parallel scheme provides a different form of the execution time:

$$\Delta T_{uth} = max(\frac{\Delta\tau_f}{\Delta t_f} \frac{N_{el,f} I_f}{P_f}, \frac{\Delta\tau_f}{\Delta t_f} n_{r,uth} \frac{N_{el,r} I_r}{P_r}, \frac{\Delta\tau_s}{\Delta t_s} \frac{N_{el,s} I_s}{P_s}) + n_{cpl} T_{com} \tag{2.8}$$

where $n_{r,uht}$ represents the total number of iterations performed by the radiative solver during a fluid time step and it is commonly set less than 1. The second right-hand term is added to account for a non-ideal communication method, that depends on the number of coupling n_{cpl} as well as the execution time T_{com} for the communication on a single coupling. The characterization of T_{com} is not trivial because can depend on the size of the exchanged data, the communication scheme and, last but not least, the computational power estimated as the number of processors, the CPU quality and the communication protocol.
To have a gain in the use of U-THERM3D approach, ΔT_{uth} must be such that:

$$\Delta T_{uth} < \Delta T_{cht} \tag{2.9}$$

Substituting Eqs. 2.7 and 2.8, in the case of ideal communication and normalizing by the total number of available processors P, Eq. 2.9 becomes:

$$\begin{aligned} max(\frac{\Delta\tau_f}{\Delta t_f} \frac{N_{el,f} I_f}{P'_f}, \frac{\Delta\tau_f}{\Delta t_f} n_{r,uth} \frac{N_{el,r} I_r}{P'_r}, \frac{\Delta\tau_s}{\Delta t_s} \frac{N_{el,s} I_s}{P'_s}) < \\ \frac{\Delta\tau_s}{\Delta t_f}(N_{el,f}(I_f + n_{r,cht} I_r) + N_{el,s} I_s) \end{aligned} \tag{2.10}$$

where $P'_x = P_x/P$ is the fraction of P demanded to the "x" solver. A perfect synchronization in CPU time should avoid queue time of the solvers, then all the simulations stop in the same instance and restart

immediately. This ideal condition is expressed as:

$$\frac{\Delta\tau_f}{\Delta t_f}\frac{N_{el,f}I_f}{P'_f} = \frac{\Delta\tau_f}{\Delta t_f}n_{r,uth}\frac{N_{el,r}I_r}{P'_r} = \frac{\Delta\tau_s}{\Delta t_s}\frac{N_{el,s}I_s}{P'_s} \tag{2.11}$$

As a result, more computationally expensive simulations will require a larger portion of the processors. The ideal distribution of the computational resources should be:

$$P'_f = \frac{\frac{\Delta\tau_f}{\Delta t_f}N_{el,f}I_f}{\frac{\Delta\tau_f}{\Delta t_f}N_{el,f}I_f + \frac{\Delta\tau_f}{\Delta t_f}n_{r,uth}N_{el,r}I_r + \frac{\Delta\tau_s}{\Delta t_s}N_{el,s}I_s} \tag{2.12a}$$

$$P'_r = \frac{\frac{\Delta\tau_f}{\Delta t_f}n_{r,uth}N_{el,r}I_r}{\frac{\Delta\tau_f}{\Delta t_f}N_{el,f}I_f + \frac{\Delta\tau_f}{\Delta t_f}n_{r,uth}N_{el,r}I_r + \frac{\Delta\tau_s}{\Delta t_s}N_{el,s}I_s} \tag{2.12b}$$

$$P'_s = \frac{\frac{\Delta\tau_s}{\Delta t_s}N_{el,s}I_s}{\frac{\Delta\tau_f}{\Delta t_f}N_{el,f}I_f + \frac{\Delta\tau_f}{\Delta t_f}n_{r,uth}N_{el,r}I_r + \frac{\Delta\tau_s}{\Delta t_s}N_{el,s}I_s} \tag{2.12c}$$

and Eq. 2.10 becomes:

$$(\Delta\tau_f - \Delta\tau_s)\frac{1}{\Delta t_f}N_{el,f}I_f + (\frac{\Delta\tau_f}{\Delta t_f}n_{r,uth}N_{el,r} - \frac{\Delta\tau_s}{\Delta t_f}N_{el,f}n_{r,cht})I_r + (\frac{1}{\Delta t_s} - \frac{1}{\Delta t_f})\Delta\tau_s N_{el,s}I_s = G_{uth} < 0 \tag{2.13}$$

The left-hand side represents the gain G_{uth} in computational time for the present loosely coupled approach if compared with a strong coupling in the ideal condition of perfect synchronization in CPU time and instantaneous communication between the solvers. Observing Eq. 2.13, the first and third terms in brackets are always negative because $\Delta\tau_f < \Delta\tau_s$ and $\Delta t_f < \Delta t_s$: a problem involving the only convection and conduction is always characterized by a safe in computational cost if solved in a loosely coupled fashion. In presence of radiation the second term in brackets should be negative to ensure Eq. 2.13. This condition is verified also in the worst case of $N_{el,r}n_{r,uth} = N_{el,f}n_{r,cht}$ because $\Delta\tau_f < \Delta\tau_s$. However, in the radiative solver of a loosely coupled approach is common practice to set both $N_{el,r} < N_{el,f}$ and $n_{r,uth} < n_{r,cht}$ in order to reduce the computational effort for the solution of this phenomenon.

Defining the time scale factor $\Delta\tau'$:

$$\Delta\tau' = \frac{\Delta\tau_f}{\Delta\tau_s} \tag{2.14}$$

and the following ratios:

$$\begin{gathered} i_f = \frac{I_f}{I_s} \quad , \quad i_r = \frac{I_r}{I_s} \quad , \\ m_r = \frac{N_{el,r}}{N_{el,f}} \quad , \quad m_s = \frac{N_{el,s}}{N_{el,f}} \quad , \quad f = \frac{\Delta t_f}{\Delta t_s} \end{gathered} \tag{2.15}$$

a general expression for the relative gain g can be defined as:

$$g = \frac{\Delta \mathrm{T}_{uth} - \Delta \mathrm{T}_{cht}}{\Delta \mathrm{T}_{cht}} = max(g_f, g_r, g_s) \tag{2.16}$$

where:

$$g_f = \frac{(\frac{\Delta\tau'}{P'_f} - 1)i_f - n_{r,cht}i_r - m_s}{i_f + n_{r,cht}i_r + m_s} \tag{2.17a}$$

$$g_r = \frac{(\frac{\Delta\tau' n_{r,uth} m_r}{P'_r} - n_{r,cht})i_r - i_f - m_s}{i_f + n_{r,cht}i_r + m_s} \tag{2.17b}$$

$$g_s = \frac{(\frac{1}{fP'_s} - 1)m_s - i_f - n_{r,cht}i_r}{i_f + n_{r,cht}i_r + m_s} \tag{2.17c}$$

Solving Eq. 2.16 with reasonable values for the parameters reported in Tab. 2.1 and a perfect load balancing provides a gain of 99.9% in respect to a strong coupling that need to be run for a time comparable to $\Delta\tau_s$ but with the fluid time step Δt_f.

$\Delta\tau'$	f	i_f	i_r	m_r	m_s	$n_{r,cht}$	$n_{r,uth}$
0.001	1000	11	16	0.3	2	1	0.5

Table 2.1: Reasonable normalized parameters for a combustor.

More interesting is the relative gain obtained exploiting a separate solver for radiation in the absence of conduction. Fig. 2.3 shows the gain as a function of the processors distribution P'_f and the mesh element ratio m_r for two different values of iteration frequency $n_{r,uth}$. Black curve ($m_r = 0$) represents the limiting case where the bottleneck is the fluid solver and all the curves collapse on $m_r = 0$ for low values of P'_f. If a bad load balancing is chosen no advantages (i.e. $g \geq 0$) are obtained

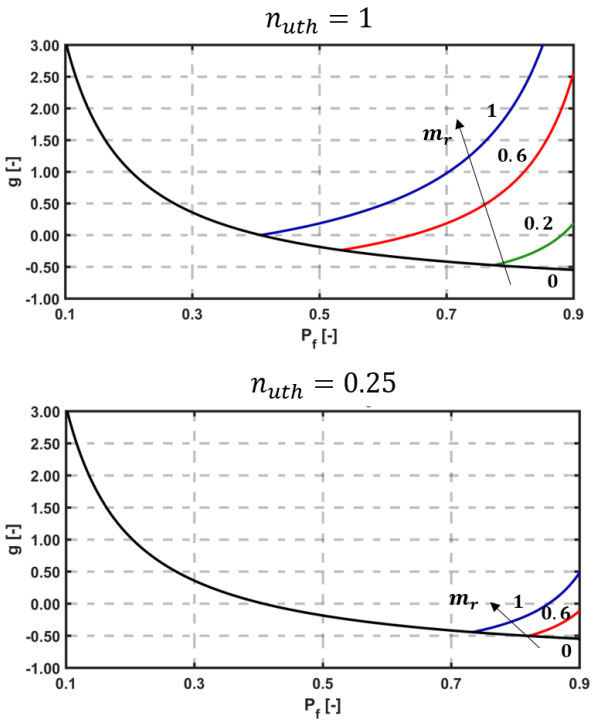

Figure 2.3: Computational gain using U-THERM3D in place of a strong coupling approach for the fluid-radiation interaction as function of P'_f for different values of m_r and $n_{r,uth}$.

with a decoupling approach. This is the case of computational resources excessively unbalanced towards radiative or fluid solvers. In the latter condition, the bottleneck is radiation. When radiative simulation becomes more computational expensive, as for increasingly iteration frequency and radiation mesh size, the gain in using separate solvers is unavoidably less evident. On the other hand, decreasing m_r and n_{uth} below critical values can lead to numerical instabilities in the coupling as well as poor accuracy of the results and a good compromise can be found only with experience. As previously mentioned, even if the U-THERM3D approach saves huge computational time, a lack of attention in the distribution of the processors

between solvers has a negative effect on the performance of the present method. Hence, the degree of performance losses Δg can be defined as:

$$\Delta g = \frac{\Delta \mathrm{T}_{uth} - \Delta \mathrm{T}_{uth}^{opt}}{\Delta \mathrm{T}_{uth}^{opt}} \tag{2.18}$$

where $\Delta \mathrm{T}_{uth}^{opt}$ is the minimum execution time provided by a perfect load balancing. Fig. 2.4 shows the trend of Δg as function of the load balance (i.e. P_f' and P_r') for the parameters of Tab. 2.1. Obviously, only values

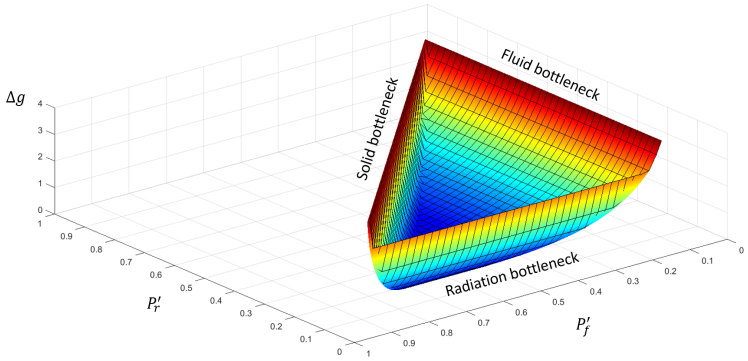

Figure 2.4: Relative computational losses for U-THERM3D in the case of non-ideal balancing as function of P_r' and P_f'.

of P_f' and P_r' such that $P_f' + P_r' < 1$ are permitted. The ideal load balancing for the present parameters corresponds to $P_f' = 0.68$, $P_r' = 0.2$ and $P_s' = 0.12$ but the computational time can increase beyond the 400% when different values are chosen. The location of the optimal point is critical because a small change in P_r' as well as a small increase of P_f' can lead to abrupt worsening of performance. This occurs because the execution time becomes driven by solid or radiation solvers depending on the value of P_r'. The three bottleneck are evident in Fig. 2.4: the rate of performance losses when more processors are devoted to a solver is inversely proportional to the cost of the simulation. Indeed, while solid and radiation show steep increase of Δg, fluid solver is less sensible to a reduction in the number of processors. Moreover, for lower values of P_f' a wider margin of P_r' is allowed without a further loss of performance.
It is worth remember that the present analysis was performed with the

main hypothesis of ideal communication between the solvers, corresponding to $T_{com} = 0$ in Eq. 2.8. However, especially when a high coupling frequency is required, this parameter can strongly affect the computational performances of a loose coupling approach. For this reason, one of the main goals in the development of such a tool is the minimization of inter-communication time through advanced methods exploiting, for instance, MPI protocol. However, optimization of these aspects are not the focus of the present work and in U-THERM3D data are exchanged using standard tools provided by ANSYS Fluent such as interpolation and profile files. Further effort is required from this perspective and it could be the starting point for future activities.

2.1.3 Preliminary assessments

A test case was simulated to check the consistency of U-THERM3D in terms of energy balance. Comparison between CFD and experiments is always affected by uncertainties in the measurements as well as in the numerical schemes. In addition, attempt to reproduce the experimental conditions in a numerical simulation is challenging because of difficulties in having full details on the geometry and accurate boundary conditions. For these reasons a test case with a well-known solution for metal temperature was conceived and set.
Fig. 2.5 shows the domain. It consists in a flat plate in contact with a gas

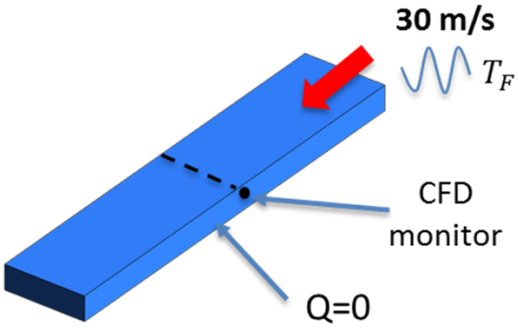

Figure 2.5: Sketch of the flat plate problem.

on one side, keeping the other sides adiabatic. This boundary condition ensures a final solid temperature equals to the mean value of an oscillating temperature signal at fluid inlet. Properties of materials were chosen to

have a speed-up in the convergence of the coupled simulation and they are reported in Tab. 2.2. A constant velocity of 30 m/s, atmospheric pressure

	Density [kg/m3]	Heat capacity [J/kg/K]	Thermal Conductivity [W/m2/K]
Fluid	3	1006	0.0242
Solid	7030	48.2	1.6

Table 2.2: Properties of materials for the simplified CHT problem.

and an harmonic temperature signal (mean value=1000 K, amplitude=50 K and frequency=20 Hz) were set at the fluid inlet. In order to limit the computational cost of the simulation, an URANS k-e turbulence model was chosen for this non-stationary test; such an approach is justifiable when the interest is on the effect of a small number of characteristic frequencies of the problem that are known a priori. The coupled simulation was run using a time step of 0.004 s and 0.005 s respectively for solid and fluid domains. The coupling was performed every 50 time steps in the solid simulation and at each time step in fluid one. Starting from an initial value of 950 K, the temperature history on the monitor point located in the solid domain (see Fig. 2.5) is reported in Fig. 2.6 as red line, overlaid with the fluid input temperature seen by the solid (black line). The final value obtained at the monitor point is the expected one, i.e 1000 K, confirming the validity of the present methodology.
A further assessment was performed on a backward-facing step depicted in Fig. 2.7, once again in the URANS $k-\epsilon$ framework. A 2-D conjugate heat transfer problem between air and a solid was investigated limiting the domain size in the spanwise direction and applying symmetry conditions. The set of boundary conditions was completed by a constant temperature and a sinusoidal velocity at the inlet and a constant pressure at the outlet. The solid was coupled with the fluid domain on one side while a convective boundary condition was applied on the other side. As a result, the location of the stagnation point is time-dependent with a consequent unsteady wall heat flux and temperature. The mean wall temperature predicted by U-THERM3D was compared against the results provided by a strongly coupled approach. To have an affordable computational cost of the reference simulation material properties of the solid were chosen to reduce its characteristic time scale and are summarized in Tab. 2.3. The initial solid temperature was set according to the steady RANS results to avoid the thermal transient. Hexahedral meshes of 800K and 20K elements was built to solve the fluid and solid, respectively. To model

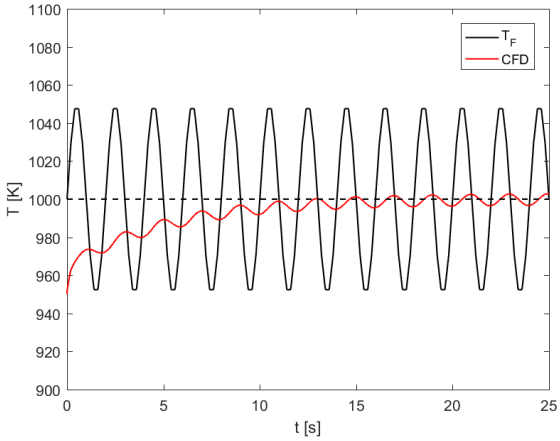

Figure 2.6: Result of wall temperature over time (red line) for the flat plate problem, overlaid with the fluid temperature at the inlet (black line) and the mean expected value (dotted line).

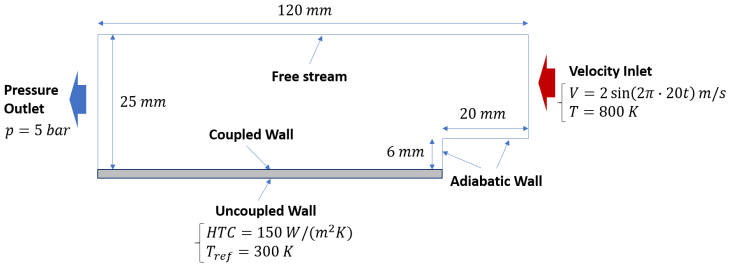

Figure 2.7: Geometric details and boundary conditions of the backward-facing step problem.

Density [kg/m3]	Specific Heat [kJ/(kgK)]	Thermal Conductivity [W/(mK)]
100	50	5

Table 2.3: Solid properties for the backward-facing step problem.

wall heat fluxes and shear stresses, scalable wall functions were adopted. Independently by the accuracy of the numerical setup, the main aim in this phase is the assessment of U-THERM3D as a valid alternative of a standard strongly coupled CHT approach. Hence, using the same mesh, numerical setup as well as boundary conditions in both the unsteady simulations the effect of a different coupling on the prediction of wall temperature can be isolated.
Fig. 2.8 shows on the axial plane the cooling of gas due to the heat transfer at wall for the U-THERM3D simulation. The different distribution of instantaneous and mean gas temperature are related to the fluctuating inlet velocity that modifies over time the size of the recirculation zone. The comparison of axial distribution of temperature at

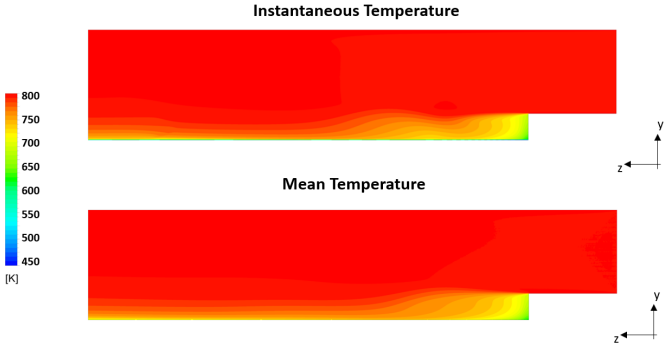

Figure 2.8: Instantaneous and mean temperature resulting form the U-THERM3D simulation for the backward-facing step problem.

the coupled wall between the two approaches is reported in Fig. 2.9. In addition, the strongly coupled (CHT) and the U-THERM3D simulations are superimposed on the result of THERM3D, a steady loosely coupled approach that will be discussed in Chapter 4. The peak wall temperature, located around the stagnation point where the heat transfer coefficient is maximum, moves upstream in unsteady simulations. The main interesting result, however, is the perfect matching of the present method with a more computational expensive one as the strongly coupled simulation, highlighting the consistency in terms of energy balance.

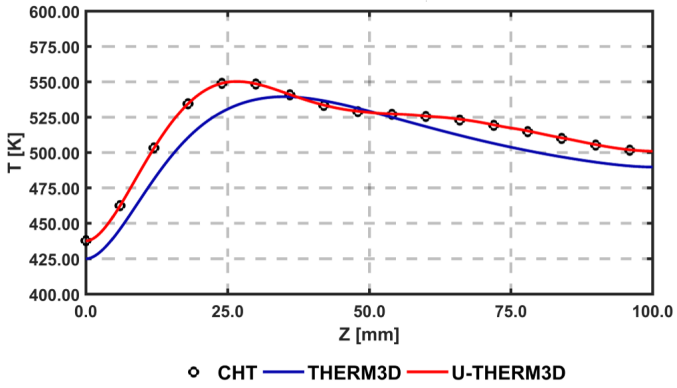

Figure 2.9: Axial distribution of temperature at the coupled wall obtained with a strongly coupled method (CHT), U-THERM3D and THERM3D

2.2 Modelling of turbulent spray flames: a brief

Numerical modelling of turbulent spray flames is a very challenging problem because it involves several interacting phenomena as turbulence, spray evolution and combustion. Gas velocity and turbulence, for instance, affect the spray evolution and the turbulent dispersion of the fuel droplets. The fuel distribution, but also the aerothermal field, determine the flame shape and position which, in turn, modify gas temperature. On the other hand, gas temperature is directly related to the aerodynamic field by means density changes and, as a result, can impact on all the aspects of spray evolution, from the motion of liquid particles to their evaporation. To face this strongly coupled problem, different approaches are proposed in literature [81, 82, 83, 84]. However, being this topic beyond the scope of this manuscript and for the sake of brevity, the interested reader is referred to [85] for a detailed overview of the most successfully methodologies and applications.

The numerical modelling here employed for the present simulations relies on the Flamelet Generated Manifold (FGM) combustion model and the approach has been widely assessed on previous works. As depicted in Fig. 2.10 the numerical procedure was applied on increasingly complex configurations, from a jet spray flame [26] to a swirled atmospheric spray flame [86, 87] and a model aero-engine combustor [27, 87, 88], highlighting the capabilities of this setup in the modelling of the coupled

phenomena. The FGM model was also investigated in the context of a

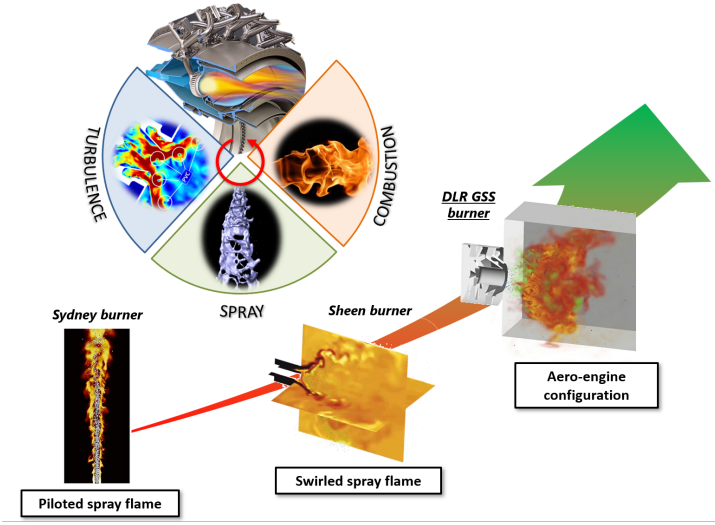

Figure 2.10: Overview of the stages towards the definition of an accurate numerical setup for turbulent spray flames.

methane gaseous swirled burner [89], revealing a good prediction of the stabilization mechanism as well as the concentration of the main species. Even though the setup here discussed shows the best potential in the context of scale-resolving simulations, it can provide acceptable solutions also when RANS models are employed.

2.2.1 The Flamelet Generated Manifold model

The use of a detailed mechanism by means of solving transport equations for every species is challenging and reduced chemistry techniques, i.e. steady-state and partial equilibrium assumptions, are not often sufficient, especially as far as scale-resolving approaches are concerned. With the aim of simplifying flame calculations, FGM method combine the philosophy of the flamelet model that a multi-dimensional flame may be considered as an ensemble of one-dimensional flames with the low-dimensional manifold ones, as explained by van Oijen in [90]. However, unlike the original flamelet models, where flamelet solution is parametrized on strain χ as

the only non-equilibrium variable, FGM is parametrized on a progress variable to account for quenching and ignition phenomena. As a result, in FGM a 2-D manifold $\phi(Z, c)$ is created through the solution of a set of laminar adiabatic 1-D flamelets and parametrizing the chemical state only as function of two key variables, i.e. the mixture fraction Z and the normalized progress variable $c = Y_c/Y_{c,eq}$. In the present work, the un-normalized reaction progress variable, which characterizes the transition from fresh to burnt gases, is always defined as $Y_c = Y_{CO} + Y_{CO_2}$. Such a choice usually provides a monotonous behaviour of Y_c between fresh and burnt gases for hydrocarbon combustion.
To include the turbulence-chemistry interactions, laminar quantities of the manifold are integrated in a pre-processing step using a presumed β-Probability Density Function (β-PDF) for both mixture fraction and progress variable, as in [91]. Assuming a statistically independence of Z and c in the flame a generic turbulent quantity $\tilde{\psi}$ is computed as:

$$\tilde{\psi} = \int\int \psi(c, Z) P(c, \tilde{c}, \widetilde{c''^2}) P(Z, \tilde{Z}, \widetilde{Z''^2}) \, \mathrm{d}c\mathrm{d}Z \tag{2.19}$$

where $\Psi(c, Z)$ is the corresponding laminar quantity. As shown in Eq. 2.19, both mean values $\tilde{(\cdot)}$ and variances $\widetilde{(\cdot''^2)}$ relying on a Favre-averaging of mixture fraction and progress variable are employed to account for turbulence. As a result, a 4-D tabulation is required for all the manifold quantities, that are species, temperature and progress variable source term as shown in Fig. 2.11. However, a fifth dimension is commonly

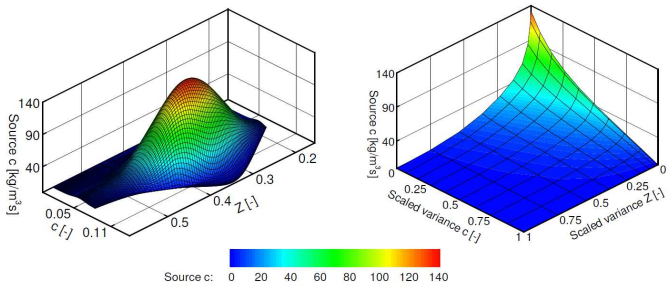

Figure 2.11: Source term of progress variable as function of Z and c (left) or Z'' and c'' (right), obtained by Ramaekers et al. [47] applying the FGM to the GRImech 3.0

added to include the non-adiabatic effects through the enthalpy defect.

Once the values of these quantities are computed, the manifold data are retrieved and an interpolation on tabulated values is performed.
The following two transport equations are solved for mean values of mixture fraction and un-normalized progress variable:

$$\frac{\partial \bar{\rho}\tilde{Z}}{\partial t} + \frac{\partial \bar{\rho}\tilde{u}_j\tilde{Z}}{\partial x_j} = \frac{\partial}{\partial x_j}(\bar{\rho}D_{eff}\frac{\partial \tilde{Z}}{\partial x_j}) + \bar{\dot{\Omega}}_z \tag{2.20}$$

$$\frac{\partial \bar{\rho}\tilde{Y}_c}{\partial t} + \frac{\partial \bar{\rho}\tilde{u}_j\tilde{Y}_c}{\partial x_j} = \frac{\partial}{\partial x_j}\left(\bar{\rho}D_{eff}\frac{\partial \tilde{Y}_c}{\partial x_j}\right) + \overline{\dot{\omega}}_c \tag{2.21}$$

where $D_{eff} = D + \mu_{sgs}/Sc^{sgs}$ is the effective diffusivity of the scalars, including molecular and Sub-Grid Scale (SGS) terms, whereas $\overline{\dot{\omega}}_c$ is the mean source term of progress variable provided by the PDF table under the finite-rate assumption. It is worth noting that in spray combustion mixture fraction is no longer a passive scalar due to the source term of spray vaporization $\bar{\dot{\Omega}}_z$.
While in RANS simulation two additional transport equations are solved for the unknown variances, in the context of scale-resolving simulations algebraic gradient-based closures are acceptable and in ANSYS Fluent they are expressed as [92]:

$$\widetilde{Y_c''^2} = C_{var,c}\frac{L_s^2}{Sc_t}(\nabla\tilde{Y_c})^2 \tag{2.22}$$

$$\widetilde{Z''^2} = C_{var,Z}L_s^2(\nabla\tilde{Z})^2 \tag{2.23}$$

where $C_{var,c} = 0.1$ and $C_{var,Z} = 0.5$ are model constants whereas Sc_t is the sub-grid turbulent Schmidt number. Such approximation is able to provide a good accuracy with a lower computational effort.

2.2.2 Lagrangian spray tracking

A coupled Eulerian-Lagrangian formulation has been instead adopted to account for the spray dynamics. Such an approach is suitable when no primary breakup takes place and in the present work no efforts have been prompted to introduce the generation of the liquid film and its subsequent atomization. It is worth pointing out that all the physical phenomena taking place in the dense spray region have been therefore overlooked as well as droplet combustion events. Models for droplet motion, evaporation and heat transfer are employed to calculate the source terms for the gas phase. Drag effects are taken into account for

the liquid momentum equation, where the drag coefficient is computed through the hypothesis of spherical not deformable droplet [93]. Secondary breakup effects are evaluated through the Wave model [94] due to the high Weber number (i.e. We >100) in all the reported calculations. Concerning evaporation modelling, a uniform temperature approach is used [95], that assumes vaporization as mainly governed by the gradient of fuel vapour concentration at the droplet surface. This is a standard hypothesis in the context of dilute sprays. The fuel vapour is considered in equilibrium with the liquid, thus the vapour partial pressure is equal to the saturation value at the droplet temperature. Employing these hypothesis, the flux of fuel vapour in the carrier phase is related to the difference in vapour concentration at the droplet surface and in the bulk gas leading to the following expression for the evaporation rate:

$$\tilde{\dot{m}}_d = -\pi d \rho D S_h B_M \tag{2.24}$$

where d is the droplet diameter, ρ and D are density and mass diffusivity of the air-vapour mixture and B_M represents the mass Spalding number [95]. S_h is instead the Sherwood number, which has been evaluated as a function of Schmidt and particle Reynolds numbers [96].
Spray-turbulence interaction is modelled by a Discrete Random Walk [92] approach in RANS framework whereas is demanded to the only resolved component of gas velocity in scale-resolving simulations.

2.2.3 Scale-resolving turbulence modelling

Direct Numerical Simulation (DNS) is the most accurate approach because an extremely fine spatial and temporal discretization, of the same order of Kolmogorov scale, is exploited. However, the high CPU cost limits its applications to particular research activities. With the aim of better characterize turbulent structures and their effects on mean flow, scale-resolving approach can be a cost-effective solution; Large-Eddy Simulation (LES), Scale Adaptive Simulation (SAS) but also hybrid RANS-LES models, such as Detached Eddy Simulation (DES), belong to this class.

2.2.3.1 Large-Eddy Simulation

In Large-Eddy Simulation (LES) a filtering operation is applied to NSEs in order to resolve, like a DNS, the large energy-carrying scales (i.e. the large eddies) and model only the smaller ones. Two main advantages

of such approach in comparison to previously cited models immediately arise:

- Reduction of the computer resources compared to DNS;
- In comparison to RANS only smallest scales are modelled and, exploiting the Kolmogorov hypothesis (see Section 1.2.2), simpler turbulence closures can be adopted.

From a mathematical point of view, in physical space a generic filtering operation represents a convolution operation as:

$$\bar{\phi}(\mathbf{x},t) = \int_T \int_V G(\mathbf{x},\mathbf{r},t,\tau)\phi(\mathbf{x}-\mathbf{r},t)d\mathbf{r}d\tau = G * \phi \tag{2.25}$$

for a scalar quantity ϕ and a given filtering function G. Hence, the subfilter component ϕ' can be defined as:

$$\phi'(x,t) = \phi(x,t) - \bar{\phi}(x,t) \tag{2.26}$$

where $\bar{\phi}$ is the resolved part.
The sub-filter components of velocity are grouped in the subgrid stress tensor that must be properly modelled to account for the effects of these scales on the resolved spectrum of the flow field.

2.2.3.2 Scale Adaptive Simulation

Scale Adaptive Simulation (SAS) approach represents a second generation URANS formulation based on the introduction of the von Karman length scale L_{vK} into the turbulence equations in order to dynamically adjust the resolved structures and locally reduce the eddy viscosity.

$$L_{vK} = \kappa|\frac{U'}{U''}|; |U'| = \sqrt{\frac{\partial U_i}{\partial x_j}\frac{\partial U_i}{\partial x_j}}; |U''| = \sqrt{\frac{\partial^2 U_i}{\partial x_j^2}\frac{\partial^2 U_i}{\partial x_k^2}}; \tag{2.27}$$

where κ is the von Karman constant. The SAS model remains in RANS mode in zones characterized by low flow instability, while it provides LES-like results in the unsteady regions of the flow field. However, if spatial and temporal discretizations are not adequate to correctly solve the LES part, SAS simulation will permanently stay in RANS mode due to an overprediction of turbulent viscosity. The RANS part of the model is unaffected by the grid spacing, preventing the issues related to possible grid induced separation (GIS), and, unlike DES, the model can be employed to perform simulations on a much wider range of numerical

grids. In its SST-SAS formulation, the governing equations of this model differ from those of standard $k-\omega$ SST RANS model by an additional SAS source term in the ω-equation [97].

Discrete Ordinate radiation model

Discrete Ordinate Method (DOM) [98] is a ray tracing approach to solve the Radiative Transfer Equation for a discrete number of finite solid angles. The balance depicted in Fig. 1.9 is applied in the control volumes for each direction. Hence, the RTE is discretized using the same mathematical treatments of NSE. Considering a polar coordinate system the whole angular space is discretized in $N_\theta \times N_\phi$ solid angles as shown in Fig. 2.12. However, such a discretization can lead to a misalignment between solid angle directions and face normals of the control volume. This overhang causes inaccuracy in the computation of fluxes of radiation intensity. To correctly account for the overhanging fraction a pixelation is applied to the overhang angles, dividing the solid angle in $N_{\theta_p} \times N_{\phi_p}$ pixels. A validation of the radiation modelling approach can be found in [99].

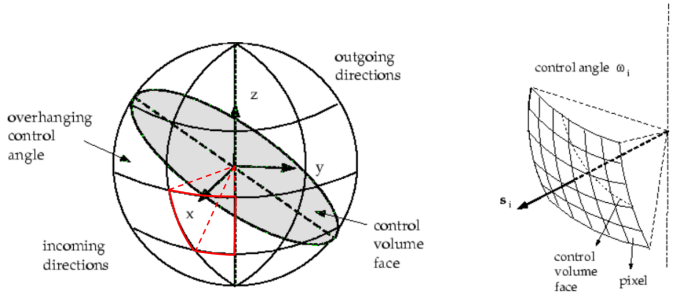

Figure 2.12: Discretization of the angular space and pixelation on a control angle overhang. Adapted from [92].

2.2.4 A further assessment of the modelling strategy

As shown in Fig. 2.10 the present modelling strategy was set up and applied in last years on increasingly complex test cases. However, these spray flames operate at an atmospheric and low pressurized environment and, therefore, they are not fully representative of real aeroengine

combustors. To simulate combustion chambers at flight conditions a further assessment step was needed. For this purpose the DLR-GSSC apparatus was chosen again because accompanied by measurements at an operating pressure of 4 and 10 bar. It consists in a combustor developed and investigated at DLR in the framework of the TIMECOP-AE Project. The main features of the burner and injection system, together with the flame shape, are shown in Fig. 2.13-left. A complete description of the

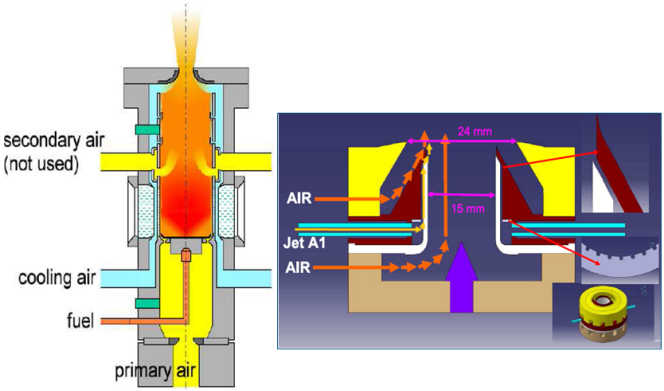

Figure 2.13: DLR Generic Single Sector Combustor with details of the swirler geometry (adapted from [100, 101]).

test case can be found in [100, 101]. The burner was designed in order to be representative of a lean burn aero-engine combustor. It consists of a cylindrical plenum feeding a square-section combustion chamber. A control of inlet air temperature, combustor pressure and Air Fuel Ratio (AFR) can be realized in order to cover different operating conditions. Jet A-1 is injected through a prefilming injection system shown in Fig. 2.13-right. Several experimental diagnostics were employed in reacting conditions like Phase Doppler Anemometry (PDA) to study velocities and droplet size of the evaporating spray and Planar Laser Induced Fluorescence (PLIF) of OH to determine the temperature distribution and flame lift-off. Tab. 2.4 summarizes the operating conditions of this test case, which can be considered as representative of a cruise condition.

Inlet pressure [bar]	10
Inlet temperature [K]	650
Burner AFR [-]	20
Burner air flow rate [g/s]	140
Slot cooling air flow rate [g/s]	39
Burner fuel flow rate [g/s]	6.8

Table 2.4: Operating conditions for DLR-GSSC [101].

Setup

The present test article has been the subject of several research works in last years employing the numerical methodology described above in the context of SAS turbulence modelling. Different aspects of the numerical procedure have been already assessed and here, for the sake of brevity, only the most important ones are mentioned. The interested reader is addressed to [27, 87], where an overview about all the work done so far is reported. The considered numerical domain together with the boundary conditions used for the gas phase are shown in Fig. 2.14. Mass flow rate

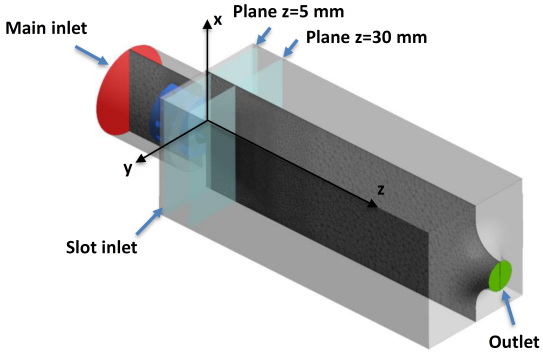

Figure 2.14: Computational domain used for DLR-GSSC burner.

was imposed at inlets of both air and slot coolant, whereas static pressure was prescribed at the outlet following data reported in Tab. 3.1. All the other patches are treated as smooth, no slip and adiabatic walls. In [27] a grid refinement study both in isothermal and reactive test conditions is

shown. The obtained results indicate that the velocity and temperature fields can be correctly determined even with the coarsest grid and that the proposed mesh refinement does not lead to appreciable improvements. Therefore, in the present work, only the coarse grid is employed. This mesh, shown in Fig. 2.14, was generated with ANSYS® ICEM-CFD and is composed by 3.28M elements and 0.76M nodes, with a mesh size of 0.75 mm at the swirler exit.

Results obtained on the present test case are strongly dependent on spray boundary conditions. In fact, the film breakup completely defines the liquid evaporation and the subsequent reacting flow field. In [88], a dedicated Eulerian wall film model was exploited to perform a detailed analysis on film evolution. A different test point (4 bar, representative of Idle condition) of the same test case was studied in order to evaluate different aspects of liquid film evolution and disruption. It was noticed that the experimental Gepperth's correlation [102] can be reliably employed to include the primary breakup at prefilming lip. Based on the operating conditions reported in Tab. 2.4 and employing a Rosin-Rammler PDF, a mean diameter of 20 μm has been defined together with a spread parameter of 2. The fuel is injected in the axial direction and with a velocity of 2 m/s in order to leave the liquid free to evolve just based on the turbulent flow field. In Tab. 2.5 the main characteristics of spray boundary conditions are briefly summarized.
The time step used has been 1e-06 s, as suggested in [27], in order to control the Courant number and properly reproduce also the main characteristics of the liquid phase.

Mean Diameter [μm]	20
Injection Velocity [$m\ s^{-1}$]	2
Cone angle [deg]	0
Spread Parameter [-]	2

Table 2.5: Main parameters for liquid injection for the DLR-GSSC.

Results

The instantaneous and time-averaged axial velocity and temperature contour plots obtained in such test condition are shown in Fig. 2.15.

The co-rotating double swirler generates a swirling flow field with a pockets of hot gases located at the center of the burner. Due to the high operating pressure and temperature of the carrier phase, the inner

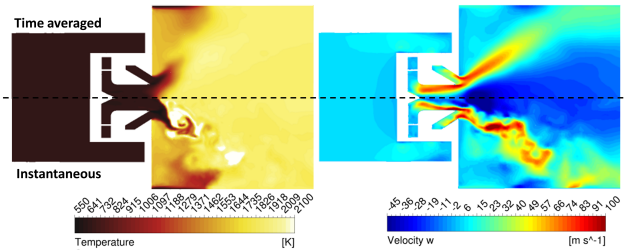

Figure 2.15: Time-averaged and instantaneous temperature and velocity contour plots obtained with SAS-FGM for Test Point C.

recirculation zone arrives nearly inside the injector. The flame moves towards the burner walls with a strong reduction of the lift-off distance with respect to results obtained at lower pressure [27, 87]. Focusing the attention on the instantaneous temperature contour, reactions seem to take place mainly in the inner surface of the spray cone where higher values of temperature can be observed. A detailed comparison of the instantaneous temperature distribution between CFD and experiments is shown in Fig. 2.16. In both images the red line indicates the presence of the liquid

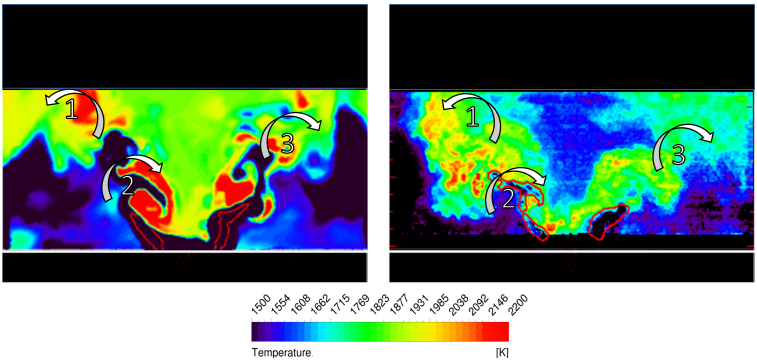

Figure 2.16: Instantaneous temperature contour plots obtained with SAS-FGM (left) and experimental map (right) adapted from [101].

phase. Clearly, the two snapshots are referred to different physical times and so the absolute local temperature is not the same. Anyway, the main characteristics of the flame can be observed and analysed.

As soon as the liquid is injected, the higher pressure and temperature here investigated lead to a strong evaporation of the fuel that is highlighted by the low temperature region inside the red iso-line. The generated kerosene vapour is mixed with air and the flame assumes a standard V-shape. Temperature peaks are located all along the inner surface of the spray cone and the flame tends to spread out towards the burner walls (1-3). Part of the fuel is instead trapped by the turbulent structures of the swirling flow field (2) and is burnt with the heat transferred from the hot inner recirculation region. From a numerical point of view, it should be pointed out that the sizing of turbulent structures is larger than in experiments. This is consistent with the SAS approach here employed, which is not probably switching everywhere to a LES-like behaviour. Nevertheless, a consistent representation of the aforementioned physical phenomena can be pointed out at least from an instantaneous point of view.
As far as time averaged distributions are concerned, the obtained contour plot of heat release is compared against experimental data in Fig. 2.17. A satisfactory agreement has been obtained. As already mentioned, with respect to results obtained at lower pressure [27] the lift-off distance is strongly reduced and this leads to a much stronger interaction between the liquid fuel and the flame.

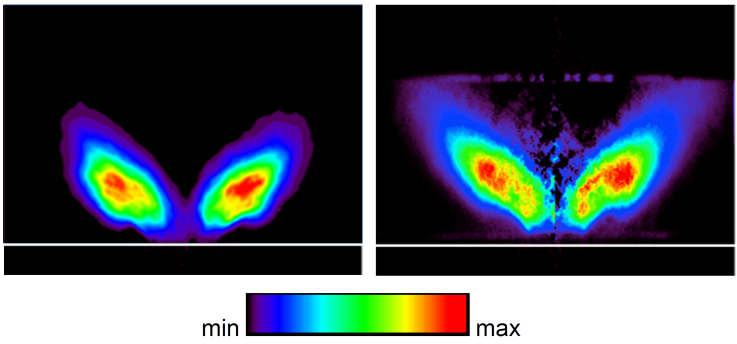

Figure 2.17: Time-averaged heat release contour plot obtained with SAS-FGM (left) against the experimental map (right) adapted from [101].

Finally, in Fig. 2.18 the obtained temperature distribution is shown together with the experimental map. It is worth noting that the experimental temperature map was obtained from absolute OH-PLIF technique and, as reported in [100, 101], they are generally affected by an over-

estimation of around 100 K. In fact, OH density has been calculated experimentally using simultaneous PLIF and absorption under the hypothesis of chemical equilibrium for OH. The OH super-equilibrium can lead locally to the afore-mentioned temperature overestimation. For the sake of clarity, from a numerical point of view the contour plot obtained accounting for such experimental uncertainty is shown in the figure, which confirms again the overall good quality of the prediction.
Therefore, from these comparison, it has been shown that, in an operating condition representative of cruise, the SAS-FGM approach determines a proper description of the reacting flow-field. These results, together with data already shown in [27, 87] with the same numerical setup, assess the proposed methodology for its exploitation on a real aero-engine combustor, which is the topic of Chapter 4.

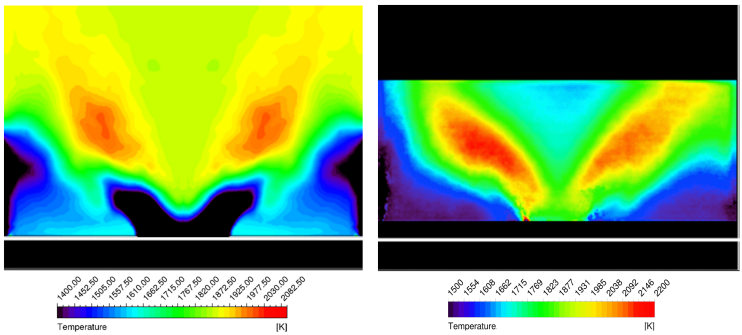

Figure 2.18: Time-averaged temperature contour plot obtained with SAS-FGM (left) against the experimental map (right) adapted from [101].

2.3 Concluding remarks

The U-THERM3D tool has been presented as potential framework for the modelling of multiphysics heat transfer in gas turbine combustors. The coupling strategy of the solving blocks as well as the numerical aspects of the main modelling tasks have been described in detail. A theoretical analysis on the computational cost of the procedure has confirmed the infeasibility of unsteady strong coupling and the need of a proper load balancing in HPC applications to save computational resources. The fluid/solid coupling has been successfully validated on simplified test cases

whereas a further assessment of the modelling strategy for turbulent spray flames has been required by the high pressure applications.

Chapter 3

DLR model aero-engine combustor

Even though research effort is widely devoted to the development of new concept designs, the RQL technology remains the standard for aero-engine combustors. The rich zone of the burner is characterized by an heavy soot production which has a negative impact on the operational safety of the combustor chamber, contributing to increase heat loads on liners due to radiation and affecting the thermal resistance of the components. Moreover, near future standards on pollutant emissions recommended by ICAO-CAEP/10 will include new criteria for the engine certification, aligning non-volatile Particle Matter (nvPM) standard to the NOx and CO ones. Indeed, it aims to replace the old smoke number criterion with a new standard regulating the number and mass of nvPM, which will be revised and made more stringent in the next CAEP/11 meeting.
Soot processes are a consequence of complex chemical processes sensitive to the temperature distribution. On the other hand, gas temperature is affected by mixing, heat transfer and thermal radiation, the latter in turn depending on soot concentration. Experimental campaigns at relevant operating conditions are associated to significant difficulties and high costs. Therefore, numerical simulations play a key role to improve the design of combustion systems and to investigate the involved phenomena. For this purpose, a proper modelling of all complex phenomena that characterize a sooting flame has to be employed. In this context, scale-resolving simulations carried out from a multiphysics perspective are required for high-fidelity results.
In the present chapter U-THERM3D will be employed to investigate the

main features of a non-premixed sooting flame. The experimental test rig is characterized by various experimental measurements in terms of gas and wall temperatures as well as soot mass concentration. In particular, a comparison on the wall temperatures will be useful to assess the procedure in the prediction of Conjugate Heat Transfer.
The chapter is structured as follows: first, a description of the experimental test case is presented together with the characterization of the mathematical models used to address physical phenomena involved in a reacting flow field and the description of the adopted computational setup. Then, numerical results are presented and compared with experimental data. Finally, the computed wall temperature is reported together with experimental measurements.

3.1 A brief review on soot modelling

The presence of soot can be accounted in numerical calculations in several ways depending on the levels of detail and complexity required. According to [103], numerical methods can be divided into three main groups: empirical, semi-empirical and detailed methods. Detailed soot models employ detailed chemistry algorithms to predict PAH formation for accurate predictions in a wide range of fuels and operating conditions, since it strongly influences soot inception and growth. At the same time, a description of soot particle size distribution is performed by these models through of a Number Density Function (NDF), defined as the number of particles of a given size. This is related to the high influence of soot particle sizes on their formation and destruction processes. The NDF is obtained by solving the Population Balance Equation (PBE) for which statistical approaches must be adopted. This is achieved with three classes of resolution methods of the PBE: the Method of Moments (MOM), the Sectional Method (SM), and the Monte Carlo (MC) stochastic Lagrangian approach. The MOM approach consists in solving the N first moments of the NDF, employing specific source terms to compute them which require untransported moments. A common approach is the Hybrid MOM (HMOM) [104], where an algebraic relationship between moments is used. On the other hand, in sectional approaches the NDF is discretised into a finite number of sections, where the soot mass fraction of each section is transported [105]. However, since at least 25 sections are required for a reliable prediction, this method is high expensive in terms of computational costs for a LES simulation. Finally, stochastic particles are tracked in a Lagrangian framework in the MC approach, directly solving the PBE to obtain the NDF. Although good results have been performed

[106], these models are computationally expensive and take much longer to return data compared to empirical and semi-empirical models. In the semi-empirical method of Moss and Brookes [107] two additional transport equations are solved for normalized radical nuclei concentration and soot mass fraction. Although deep investigations on soot distribution cannot be carried out with such model, the low computational cost and the easy implementation into CFD solvers appoint this model as a robust alternative to more complex approaches for soot investigation [108].

3.2 Experimental test case

In the present study, numerical simulations of DLR model aero-engine combustor are reported. The considered test case shows the typical features of a real aero-engine combustor and it is representative of a RQL technology. This test rig has been developed and investigated by Geigle et al. [109, 110] at German Aerospace Center (DLR), providing a rich dataset of accurate measurements for several operating conditions. For a detailed description of the experimental setup and the investigated operating conditions, the reader is addressed to [109] and references therein. In Tab. 3.1, the conditions of the investigated operating point are highlighted.

Operating pressure [bar]	3
ϕ [-]	1.2
$P_{primary}$ [kW]	32.2
$Q_{air,c}$ [slm]	140.8
$Q_{air,r}$ [slm]	328.5
Q_{fuel} [slm]	39.3
Q_{oxi} [slm]	187.4

Table 3.1: Investigated operating condition.

A sketch of the main geometrical features is reported in Fig. 3.1. The combustion chamber has a square section of 68x68 mm^2 and is 120 mm high. It is surrounded by a stainless-steel pressure housing. Combustor and housing walls consist of quartz windows in order to ensure optical access within the combustion chamber for the collection of experimental data.
Primary air is supplied through a dual radial swirler. The inner swirler has a Swirl Number $SN = 0.82$ and consists of 8 vanes, whereas the outer

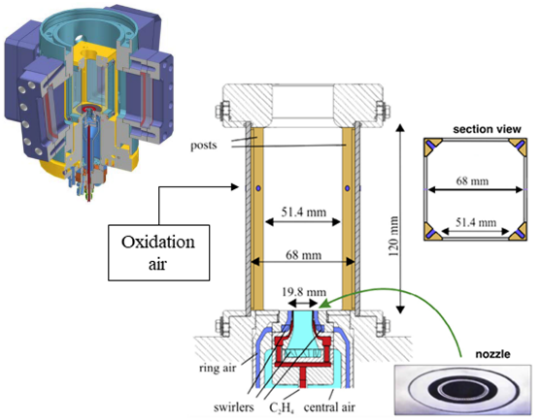

Figure 3.1: DLR-FIRST burner.

one is composed of 11 vanes ($SN = 0.78$). This configuration generates a recirculation zone and a highly turbulent region next to the injector outlet. An additional system of ducts are located at each of the four corners of the combustion chamber at a height of 80 *mm* for the injection of secondary air. These dilution jets create a quench region, according to the RQL concept. Ethylene is injected by means of a concentric ring of 60 equally spaced straight channels between the internal and the external air channels. As far as the experimental campaign is concerned, available data consist of measurements in terms of velocity components with Stereo-PIV (Particle Image Velocimetry), temperatures with SV-CARS (Shifted Vibrational Coherent Anti-stokes Raman Scattering) [110] and in terms of soot volume fraction adopting LII (Laser-Induced Incandescence) [109].

3.3 Numerical details

3.3.1 Turbulence Modelling

The compressible Navier Stokes Equations (NSEs) for a reacting mixture have been solved employing a LES turbulence modelling. In this work, the Wall Adapting Local Eddy viscosity (WALE) model [111] has been employed for the closure of the sub-grid stress tensor. In this approach, the eddy viscosity μ_t is related to the resolved strain rate $\overline{S}_{ij}$

as:

$$\mu_t = \rho L_s^2 \frac{\left(S_{ij}^d S_{ij}^d\right)^{3/2}}{\left(\overline{S}_{ij}\overline{S}_{ij}\right)^{5/2} + \left(S_{ij}^d S_{ij}^d\right)^{3/2}} \tag{3.1}$$

Here, L_s and S_{ij}^d are, respectively, the characteristic SGS mixing length and the traceless symmetric part of the square of the velocity gradient tensor $\overline{g}_{ij}$ defined as:

$$L_s = min\left(\kappa d, C_w V^{1/3}\right) \tag{3.2}$$

$$S_{ij}^d = \frac{1}{2}\left(\overline{g}_{ij}^2 + \overline{g}_{ij}^2\right) - \frac{1}{3}\delta_{ij}\overline{g}_{kk}^2, \qquad \overline{g}_{ij} = \frac{\partial \overline{u_i}}{\partial x_j} \tag{3.3}$$

where κ is the von Karman constant, d is the local distance to the closest wall, $C_w = 0.325$ is the WALE constant, V is the cell volume and δ_{ij} is the Kronecker delta.

3.3.2 Soot Modelling

According to Moss and Brookes model [107], two additional trasport equations for radical nuclei concentration b_{nuc}^* and soot mass fraction Y_{soot} have been solved:

$$\frac{\delta\left(\rho b_{nuc}^*\right)}{\delta t} + \bigtriangledown \cdot \left(\rho \overrightarrow{v} b_{nuc}^*\right) = \bigtriangledown \cdot \left(\frac{\mu_t}{\sigma_{nuc}} \bigtriangledown b_{nuc}^*\right) + \frac{1}{N_{norm}}\frac{dN}{dt} \tag{3.4}$$

$$\frac{\delta\left(\rho Y_{soot}\right)}{\delta t} + \bigtriangledown \cdot \left(\rho \overrightarrow{v} Y_{soot}\right) = \bigtriangledown \cdot \left(\frac{\mu_t}{\sigma_{nuc}} \bigtriangledown Y_{soot}\right) + \frac{dM}{dt} \tag{3.5}$$

where M is the soot mass concentration and N is the soot particle number density.
In Eq. 3.4, the instantaneous production rate of soot particles dN/dt is the result of two opposite contributions, nucleation from the gas phase (source) and coagulation in the free molecular regime (sink):

$$\begin{aligned}\frac{dN}{dt} = &\underbrace{C_\alpha N_A \left(\frac{X_{prec} P}{RT}\right)^l exp\left\{-\frac{T_\alpha}{T}\right\}}_{\text{Nucleation}} \\ &\underbrace{- C_\beta \left(\frac{24RT}{\rho_{soot} N_A}\right)^{1/2} d_p^{1/2} N^2}_{\text{Coagulation}}\end{aligned} \tag{3.6}$$

where C_α, C_β and l are model constants.
In Eq. 3.5, the source term for soot mass concentration dM/dt is affected by the effects of different mechanisms of nucleation (source), surface growth (source) and oxidation (sink):

$$\begin{aligned}\frac{dM}{dt} = &\underbrace{M_P C_\alpha \left(\frac{X_{prec}P}{RT}\right)^l exp\left\{-\frac{T_\alpha}{T}\right\}}_{\text{Nucleation}} \\ &\underbrace{+ C_\gamma \left(\frac{X_{sgs}P}{RT}\right)^m exp\left\{-\frac{T_\gamma}{T}\right\}\left[(\pi N)^{1/3}\left(\frac{6M}{\rho_{soot}}\right)^{2/3}\right]^n}_{\text{Surface Growth}} \\ &\underbrace{- C_{oxid} C_\omega \eta_{coll}\left(\frac{X_{OH}P}{RT}\right)\sqrt{T}(\pi N)^{1/3}\left(\frac{6M}{\rho_{soot}}\right)^{2/3}}_{\text{Coagulation}}\end{aligned} \tag{3.7}$$

where C_γ, C_{oxid}, C_ω, m and n are additional model constants.
It is worth specifying that the components of the source terms of each equation show a strong non-linear dependency by temperature which highly affects soot distribution within the combustor, making soot formation strongly coupled to spatial evolution of the reactive flow and to temperature distribution. This strict dependency by the temperature was investigated in previous RANS studies [112] on the same test case, highlighting how including radiation can drastically modify the soot concentration field. At the same time, it is important to note the source term dependence on the mole fraction of soot precursors. Therefore, a proper numerical setup in this sense is crucial for a reliable prediction of soot distribution.

3.3.3 Setup

As required by U-THERM3D, three different computational grids were generated with ANSYS Meshing. The governing equations of CFD solver have been discretised and resolved on the 11Me tet mesh shown in Fig. 3.2. Size of the elements was deduced by preliminary RANS simulations as shown on the top of Fig. 3.2 and verified a posteriori with the Pope's criterion. Local refinements were carried out in the primary and dilution zones, characterized by a higher unsteadiness. To properly solve turbulent structures in the flame zone a minimum size of 0.8 mm was applied. It is worth mentioning that the outlet was extruded for 2.5 diameters to avoid non-physical disturbances in the flametube. Instead, an hexahedral mesh

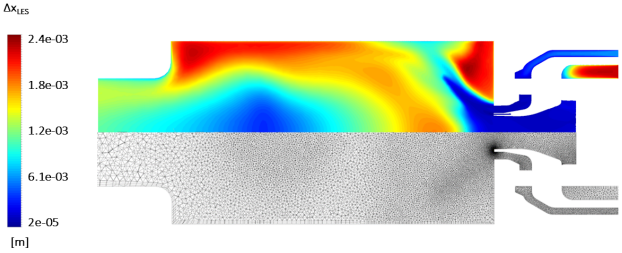

Figure 3.2: Preliminary sizing calculation (on the top) and gas phase mesh (on the bottom).

of 2.5Me has been employed to solve conduction in the quartz windows with 10 elements on the thickness.
An LES-FGM simulation was carried out to simulate the aerothermal field. Since an ethylene/air combustion occurs within the combustion chamber, Wang and Laskin mechanism [113] has been adopted for the description of the chemical kinetics, considering 75 species and 529 reactions. A set of 64x64 flamelets was generated for the tabulation of the species, temperature and progress variable source. For the present study, the Discrete Ordinate radiation model was adopted with a 4x4 angular discretisation and a 3x3 pixelation for each direction. Finer discretisations were investigated in RANS context but the simple burner geometry did not highlighted improvements in the results. In addition, spectral radiation has been included through a weighted sum of grey gases, using Modest expression [114] to account for the presence of soot.
Timesteps have been chosen relying on the requirements of the different solvers and applying the desynchronisation technique [59]. As a result, fluid time step has been set to 2e-6 s, whereas the solid solver has been advanced for a larger timestep of 1e-3 s. The coupling between simulations was performed every 10 fluid timesteps and 40 solid timesteps.
The whole multiphysics simulation was run on 160 CPU (Xeon E5-2630v4), requiring 2 and 3 flow through times, respectively for flushing and averaging, corresponding to a total effort of 85000 CPU hours.

3.4 Results

In the following section, the results of the computed numerical simulations are reported. Firstly, an analysis of the aerothermal features of

the combustor is performed, focusing the attention on velocity, gas temperature and soot fields. Then, experimental data of metal temperature distributions are compared with the numerical results obtained in [112] using the THERM3D approach and a similar numerical setup with the exception of turbulence modelling. For more information, the reader is addressed to [112] and references therein.

Aerothermal fields

The computed instantaneous and time-averaged velocity and temperature distributions in a plane passing the centerline of the combustor are reported in Fig. 3.3. Velocity fields highlight the typical flow structure of

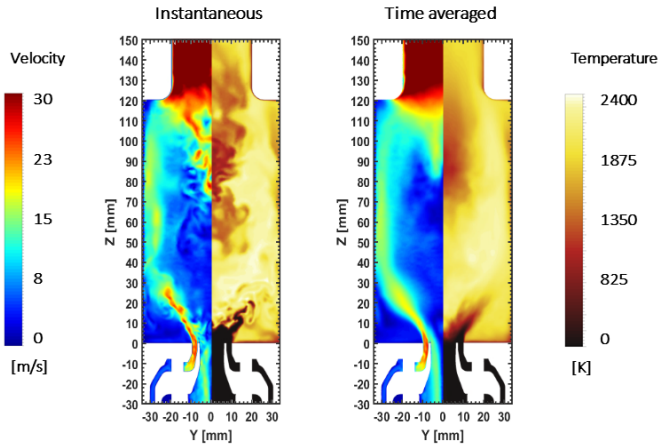

Figure 3.3: Instantaneous and time-averaged velocity (left) and temperature (right) distributions in a midplane of the combustor.

a swirling flow. In fact, an inner and outer recirculation zone generated by the double swirler system can be appreciated downstream the injector outlet and all around the burner respectively, whereas higher velocities remain along the combustor walls.
Regarding temperature fields, peak values are located in the first part of the combustion chamber where the flame is stabilized and a typical V-shaped flame can be observed. This occurs since the secondary air injected by the dilution holes recirculates backward up to the swirler, shifting the

flame towards the stoichiometric conditions. Moving downstream, the highest temperatures are placed close to the walls, far from the axis of the burner where a significant amount of secondary air is present. Such air determines a significant quenching of the flame, strongly reducing the gas temperature towards the chamber exit. From the instantaneous contour, turbulent structures can be appreciated, causing the corrugation of the flame front in the primary region and the mixing of the oxidation air in the secondary zone

As far as temperature profile along the centerline of the combustor is concerned, a quantitative comparison is reported with respect to experimental data and RANS results in Fig. 3.4. The numerical values are in

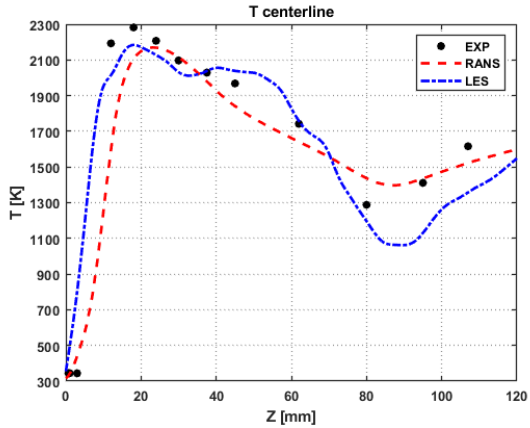

Figure 3.4: Comparison in terms of temperature profiles along the centerline of the combustor.

good agreement with experimental measurements, where the stabilization of the flame occurs and a better prediction of temperature axial trend is performed compared to RANS results, especially in terms of peak location. However, an underestimation of the peak value and an under-prediction of about 100 K downstream of secondary air inlets can be observed. This is probably due to an incorrect computation of turbulent mixing levels around the injection region of the oxidation jets, causing an higher penetration of secondary air and a lower convection towards the flame, which does not feed the combustion process. This may be related to the absence of secondary air ducts in the computational domain and to the

top-hat profiles adopted for velocity and temperature at secondary inlets. For a deeper understanding of the effects of turbulent fluctuations on the temperature field within the combustion chamber, a comparison between experimental and numerical results in terms of Probability Density Functions (PDFs) of instantaneous temperature is reported in Fig. 3.5, where r is the radial coordinate with respect to the axis of the combustor.

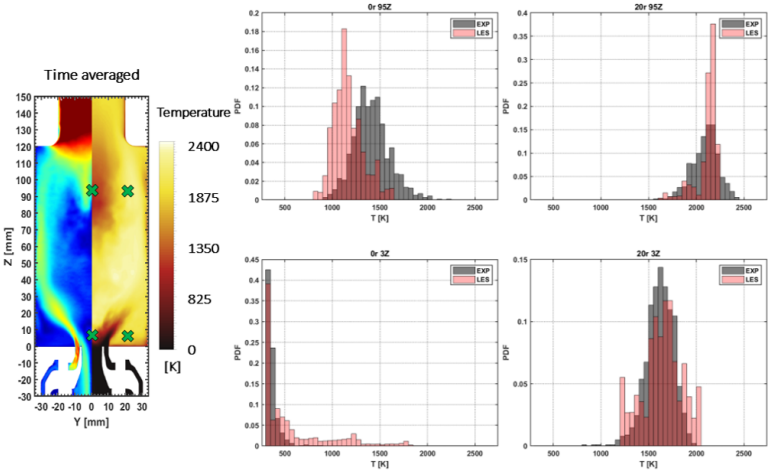

Figure 3.5: PDF temperature at four locations in the combustor.

As far as axial locations are concerned ($r = 0mm$, on the bottom of the figure), a general agreement can be appreciated in terms of range and values for $Z = 3mm$ whereas a shift towards lower temperatures of the modal value occur downstream the secondary air inlets for $Z = 95mm$, related to the underestimation of temperature levels in this region, as previously shown. A better prediction is performed close to the walls (on the top) where it is possible to note a fairly good agreement with experimental data in terms of the spreading of the distribution as well as the statistic mode value. Some discrepancies can be observed at $Z = 95mm$ where it seems that less fluctuations are computed, probably due to an under-predicted spreading of dilution air. Nevertheless, as aforementioned, during the simulation the resolution of the turbulence field was checked by means of Pope criterion [115], confirming the goodness of the methodology used to determine *a priori* the mesh sizing.
Regarding soot formation within the combustor, Fig. 3.6 and Fig. 3.7

show a comparison between experimental and numerical results in terms of time-averaged and instantaneous soot volume fraction distributions, respectively. From the experimental map, it can be noted that soot is primarily formed in the high temperature region next to the injector exit and in the outer part of the recirculation zone. High soot levels can be also observed close to the walls when the pollutant particles are transported downstream until dilution air causes soot oxidation.

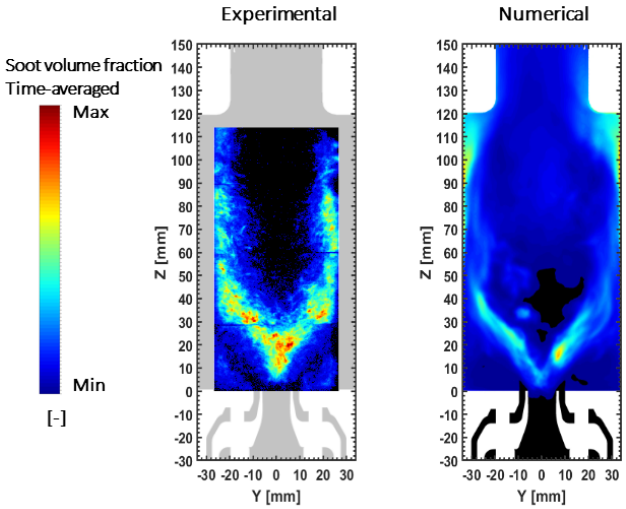

Figure 3.6: Experimental and numerical time-averaged soot volume fraction distributions in a midplane of the combustor.

Considering time-averaged results, a similar qualitative distribution is performed by numerical simulation and the same cone shape enclosing the peak value regions can be identified. However, soot levels are underpredicted by one order of magnitude from a quantitative point of view. This can be ascribed to the simplified soot model as well as to the lower temperature in the flame zone, reducing the soot source terms defined in Eqs. 3.6-3.7 that, as mentioned before, is highly sensitive to temperature. From the instantaneous contour, the intermittent and localized nature of soot production is highlighted, due to high temperature dependence of all complex phenomena involved in this process. In the numerical map, the red line bounds the region with a positive soot mass source maxi-

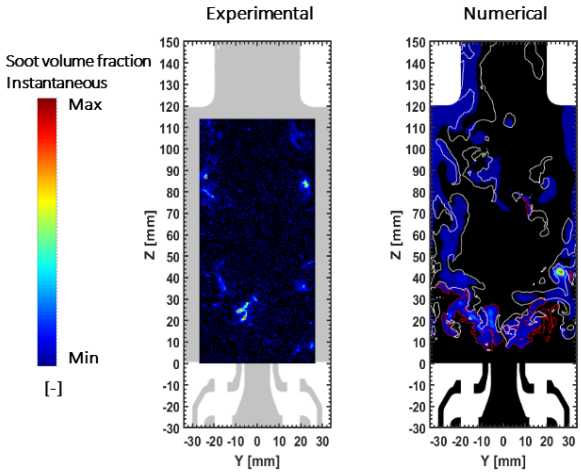

Figure 3.7: Experimental and numerical instantaneous soot volume fraction distributions in a midplane of the combustor.

mum value (related to soot formation) while the white line highlights the negative values zone (related to soot oxidation), allowing to understand where soot particles are generated and oxidized. As described before, soot formation regions are mainly localized at the burner outlet where the reaction process starts. Secondary injections supplies fresh air also to the recirculation zone where oxidation can be observed. Also in this case, an under-prediction of roughly one order of magnitude is performed by CFD. As shown in Fig. 3.8 and 3.9, the computed instantaneous and time-averaged distributions are also reported for OH mass fraction in order to better visualize the flame structure and a qualitative comparison with experimental maps is discussed.

As far as instantaneous plots are concerned, it can be observed how the LES approach allows to describe turbulent structures which corrugate the flame front downstream the injector exit. Peak regions are predicted at the inner and outer surface of the swirling flow (1-2), whereas lower values are located where the flow spreads next to the injector exit as observed in the experimental map (3). High levels of OH remain also downstream, surrounding the quenching zone in contrast to experimental map. Here, unburned hydrocarbons which come from the first reaction

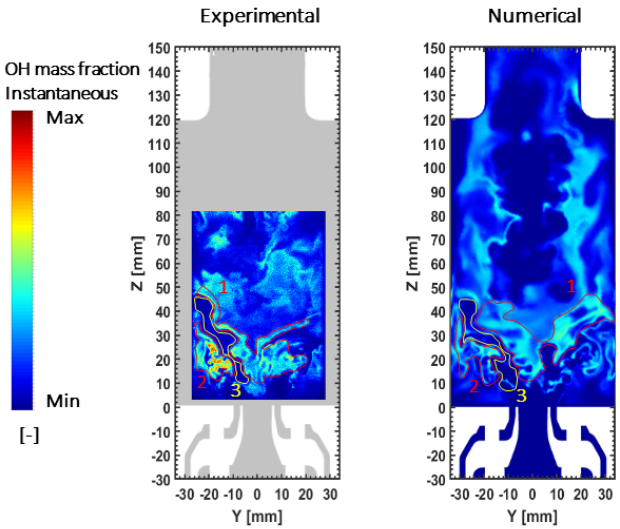

Figure 3.8: Experimental and numerical instantaneous OH mass fraction distributions in a midplane of the combustor.

zone feed a second flame front. This is probably related again to the underestimation of the turbulent mixing of the oxidation jets, leading to a more pronounced flame front in this region rather than in the recirculation zone.
A general qualitative agreement can be also appreciated when time-averaged distributions are considered. High values of OH means that reactions occur in the central region and go on downstream close to the walls, observing a similar evolution both in the numerical and in the experimental results. A similar distribution can be also noted in the corner vortex region with a slightly smaller spreading of the flame front in the numerical map.

Quartz temperature

The previous section has highlighted the main findings about the investigation of a sooting flame using U-THERM3D. The gas temperature, however, is not only affected by an energy redistribution due to radiation. Convective and radiative wall heat fluxes related, respectively, to the

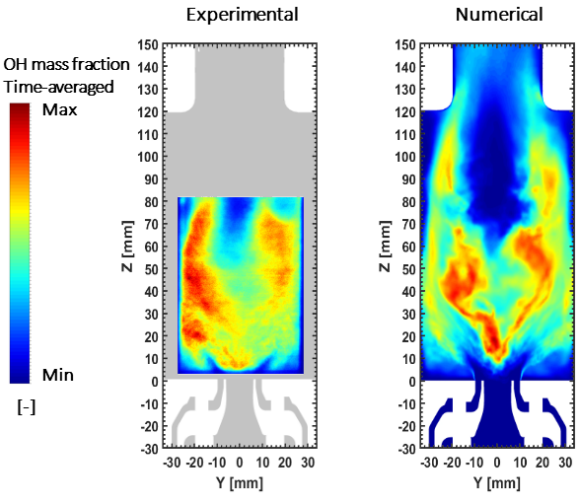

Figure 3.9: Experimental and numerical time-averaged OH mass fraction distributions in a midplane of the combustor.

fluid-solid and radiation-solid interactions can generate relevant heat losses that modify the aerothermal field. These interactions are taken into account using multiphysics tools as U-THERM3D, whose main output is precisely the solid temperature. Nevertheless, in the present work, for the hypothesis of totally-transparent window, radiative wall heat flux corresponds to the incident radiation and is independent by the surface temperature, eliminating the need of radiation-solid coupling.
Fig. 3.10 shows the temperature distribution on the hot and cold sides of the quartz window. The wall region that faces to the burner primary zone has the highest thermal load. Convective heat transfer in this zone is driven by flame-wall interactions that expose the surface to high temperatures as well as to high turbulence which increases the heat transfer coefficient. The peak temperature reaches almost 1600 K. This value is not surprising because the windows are uncooled on the hot side and cooled only by tangential air jets on the cold side. According to the lower gas temperature, at downstream positions along the axial direction the window temperature decreases as well. Closer to the boundaries, solid temperature drops abruptly to the constant value of 900 K sets

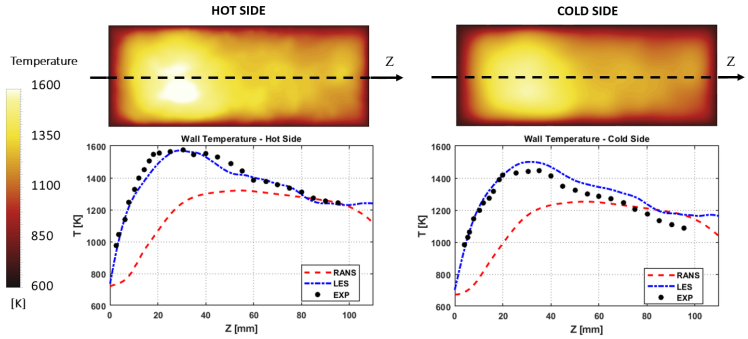

Figure 3.10: Quartz windows temperatures compared with experiments [116] and RANS results [112].

on the adjoining surfaces that are not included in the conjugate heat transfer problem at this point of the work. Because of the low thermal conductivity of quartz, however, boundaries limit their influence to few millimeters and the region around mid-line is unaffected.
A comparison with experimental data on the window centerline reported in Fig. 3.10 emphasizes the predictive capabilities of U-THERM3D as far as the wall temperature is concerned. Indeed, numerical results are in good agreement with experiments along the whole surface. Compared to the THERM3D results obtained in [112], the window is 200 K warmer in the peak region. This different behaviour is mainly related to the resolution of turbulence scales in LES. The turbulent structures influence all the processes involved in swirling flames, from combustion to aerodynamics, playing a key role also in the convective motions. A resolution of the larger scales of the turbulent wall heat flux improves the prediction of the heat load that, in this case, is higher than the one computed by a RANS model. As a result of the major heat losses, wall temperature decreases gradually and similarly to the experimental trend. In [116] the wall heat flux is correlated to the downstream oxidation at higher radii caused by the additional air as shown in Fig. 3.9. Indeed, the mixing with the partially-burned rich mixture releases further energy that contributes to keep the gases warm. In the present simulation secondary air recirculates less than in experiments and the aforementioned phenomenon is reduced, making the temperature plateau narrower and the wall temperature slightly underestimated for $Z > 40mm$. Nevertheless,

as the U-THERM3D curves match the measurements on both the window sides with good accuracy, conduction within the solid seems well-predicted by the present methodology.

3.5 Concluding remarks

In the present chapter, a reactive Large Eddy Simulation of a non premixed ethylene/air sooting flame has been performed, employing a semi-empirical model for the prediction of soot formation. The calculation has been carried out in the framework of the U-THERM3D multiphysics procedure employing three loosely-coupled simulations for fluid, solid and radiation. This allows to appropriately account for the mutual interaction of convective and radiative heat transfer, combustion and soot production. The computed results have been compared with the available experimental measurements in terms of aerothermal fields, emissions and solid temperatures.
Regarding the gas phase temperature, LES results provide a general good agreement along the centerline of the combustor with a slight under-prediction of the peak value in the rich region and some discrepancies downstream of the secondary air inlets. The reason of these differences has been ascribed to an underestimated secondary air recirculation, causing an improper enhancement of the reaction process in the rich region. These considerations have been confirmed by the analysis of PDF temperature distributions at different characteristic locations within the combustor, where a better prediction can be noted closer to the walls rather than on the combustor axis.
Together with the simplified adopted model, these discrepancies have led to an underestimation by one order of magnitude of soot volume fraction. However, the cone shape and the location of the peak values in the rich region are generally predicted from a qualitative point of view and soot particles remain next to the combustor walls until they reach the oxidation region. From the instantaneous plots, the intermittent and localized nature of soot production can be observed.
Concerning wall temperature distributions, U-THERM3D procedure is able to properly predict the heat loads acting on combustor walls and the conduction within the solid. In this context, an accurate evaluation of local wall heat flux fluctuations is fundamental for a reliable calculation of the wall temperature which can only be provided with a scale resolving approach, such as LES model.

Chapter 4

LEMCOTEC combustor

With the aim of fulfilling pollutant emission limitations required for the next generation of civil aero-engines [4], lean burn combustion appears as one of the most promising technologies. Differently from current RQL technology, reduction of NO_x emission levels is achieved working in a narrow range of flame temperature and local equivalence ratio. Indeed, it should promote a rapid mixing between air and fuel in the primary zone to minimize mixture inhomogeneities. Moreover, the absence of dilution holes complicates the control of exit profile temperature that must be attained acting on the burner aerodynamics. As far as the liner heat load is concerned, highly-effective cooling systems are required to face the limited availability of coolant. Considering the costs and complexity related to experimental investigations at high pressure and temperature conditions, Computational Fluid Dynamics has been adopted as primary tool to have a deeper insight into the involved phenomena and, as a result, support the aerothermal design of modern LDI combustors.
In this chapter, a modelling strategy for turbulent spray flames is applied to a lean burn annular combustor designed and tested during the LEMCOTEC (Low EMission COre-engine TEChnologies) European Union Project. The main goal here is the investigation of methods from a design perspective to assess its capabilities in the prediction of the burner performance with different levels of accuracy, with a special focus on the metal temperature. The chapter is divided into two part: first, steady CHT analysis were carried out with the THERM3D tool for a preliminary investigation of the heat load trend in different operating conditions. Then, the aerothermal field and metal temperature were investigated from a high-fidelity perspective solving adiabatic flametube and U-THERM3D multiphysics simulations, respectively.

4.1 LEMCOTEC combustor

The test case consists in the prototype of a single annular combustor developed in the context of the LEMCOTEC European project. Part of the air passing through the dump diffuser is directed to the annuli where it is used for the liner cooling and the bleeding holes. The remaining part is instead divided between the swirler and the dome cooling system. The dome is protected by an impingement-cooled heat shield, which additionally provides slot cooling through coolant discharge, whereas the liners are equipped with staggered arrays of inclined effusion cooling holes with circular cross section. Despite the impossibility to show the actual device due to confidentiality issues, it can be considered an evolution of a previous combustion chamber designed, manufactured and tested during the NEWAC program (see Fig. 4.1). Compared to such a device, volume of the combustion chamber, shape of the flametube and characteristic of the effusion cooling system were revised to enhance emissions and durability of the liners. Another significant improvement to the reduction of pollutant formations was achieved through the redefinition of internal flow split and injection system.

Figure 4.1: GE Avio's NEWAC combustor prototype.

The combustion system, based on lean burn combustion, achieves low NO_x emission using an innovative injection system called PERM (Partial Evaporation and Rapid Mixing), developed for medium overall pressure ratios ($20 < OPR < 35$). The device, whose sketch is reported in Fig. 4.2, is characterized by co-rotating double radial swirlers. Flame stabilization is ensured by fuel staging between the pilot injection from a pressure

atomizer (for low-power stability) and the main injection achieved through the formation of a film on the outer side of the lip.

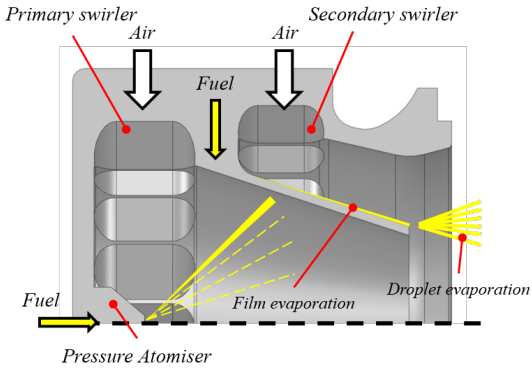

Figure 4.2: Sketch of the injection system.

Design validation was carried out in the final stage of the project through tests performed at the Central Institute of Aviation Motors (CIAM). All the experimental data reported in the present paper were collected at CIAM during the experimental campaign. The details about the operating point considered in this work have been reported in Tab. 4.1. It is worth mentioning that tests were performed only up to the Cruise condition, while the Take-Off test point was considered in this work only from a numerical point of view, exploiting the validated CFD methodology.

Test point	P30 bar	T30 K	FAR ‰	P/T %	Active injectors
Idle (ICAO 7)	5.4	518	14.5	100	9
Approach (ICAO 30)	13.5	655	17.2	70,90,100	18
Cruise (ICAO 85)	13.5	655	28.3	5,10,20	18
Take-Off (ICAO 100)	19.0	840	28.3	5,10,20	18

Table 4.1: Description of the investigated test points. Underlined the value of P/T used in the CFD simulations.

The experimental measurements performed on such full annular combustor allowed to obtain valuable data in terms of pollutant emissions, exit

temperature profile and wall temperature. In details, temperature profiles and emissions were acquired with a rotating traverse system installed at the combustor outlet (Plane 40). Available data consist of CO_2, H_2O, CO, NO_x and uHC emissions sampled by two rotating probes characterized by 4 extraction holes, from which the gas is collected, mixed and analysed. As shown in the left side of Fig. 4.3, the traverse system is equipped also with four rakes that measure the temperature at 5 span locations. An example of the resulting temperature pattern is shown in the right side of Fig. 4.3. Metal temperature of the liners, instead, were measured at different stream- and span-wise locations by means of thermocouples equipped on the cold side of the liners. Measurement points were located in selected sectors at different angular positions and grouped to obtain a tangential distribution for a single ideal sector.

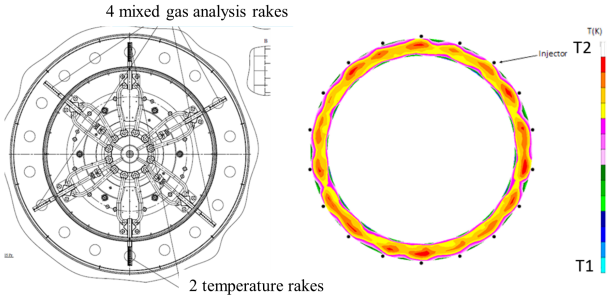

Figure 4.3: Sketch of the traverse system (left) and example of resulting temperature pattern at Plane 40 for the Approach condition (right).

4.2 Preliminary steady CHT analysis

In each design process, a preliminary investigation of the combustor using low time-demanding approaches should be mandatory as intermediate stage. In the context of CFD methodologies for a detailed design of combustor liners, the aerothermal field is computed employing a RANS simulation and the in-house THERM3D approach is here applied for the 3D prediction of the metal temperature.

4.2.1 THERM3D procedure

The key concepts of the methodology are analogous to that made in [35] for ANSYS® CFX code, i.e. the execution of a multiphysics calculation composed of an iterative sequence of three different simulations: reactive CFD, radiation and heat conduction. The interaction among the simulations is accomplished through the exchange of data according to [30, 59, 117]. Then, the new procedure can be seen as an upgrade of THERM3D design tool [35] in order to exploit the ANSYS® Fluent capabilities in terms of combustion, spray and radiation models. The three simulations run in a sequential manner; then, in order to minimize the computational time, all of them are simultaneously loaded. The queues and exchange of data are handled by User Defined Functions (UDFs) [118] and Scheme language [119].
The conceptual representation of the procedure is depicted in Fig. 4.4:

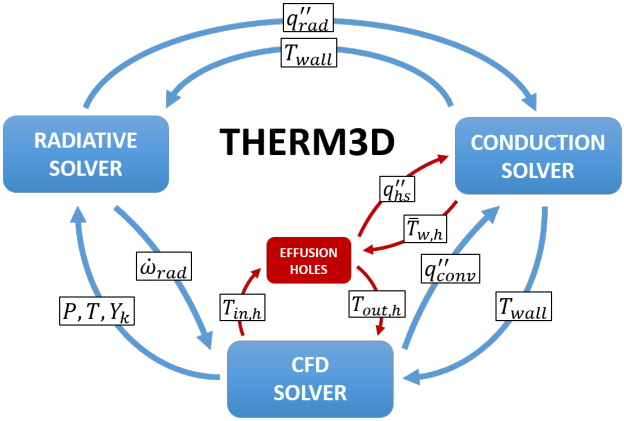

Figure 4.4: Conceptual representation of the THERM3D methodology.

1. The flow field simulation can involve turbulent combustion, heat transfer and liquid fuel injection. After a predefined number of iterations, temperature, pressure and species fields are passed to the radiative solver.

2. On the basis of the actual wall temperature profile (i.e. a guess solution at the first loop) and a frozen aerothermal state within the domain, the radiative solver provides a wall heat flux for solid

calculation while the energy source/sink ascribable to radiation are returned to the flow solver.

3. As in U-THERM3D, convective and radiative heat fluxes at coupled walls are passed to heat conduction solver after converting them to convective and black-body radiation boundaries, respectively. Using these fluxes the solid solver returns a wall temperature distribution for the other simulations. Metal temperature into film cooling holes is averaged and passed to the effusion solver for the estimation of heat sink effect.

4. The previous steps are repeated until the convergence of the procedure, evaluated in terms of mean metal temperature variation between the last two iteration, is satisfied.

The THERM3D procedure is composed of two different internal loop, as shown in Fig. 4.4. An inner loop exploits an effusion solver (i.e. "effusion holes" block in Fig. 4.4) to compute and set the temperature of coolant exiting the hole based on a continuous updating of gas temperature at hole inlet due to the CFD computation. An outer loop, instead, performs the metal temperature evaluation that is given back to the CFD solver as wall temperature distribution and to the UDF as mean hole wall temperature. It is worth mentioning that a first guess CFD solution is obtained assuming a uniform metal temperature distribution.

4.2.2 Numerical setup

As explained in the previous section, the present thermal procedure is based on three different simulations that must be independently set, with specific requirements in terms of computational grid, discretization schemes, stability and convergence criteria. First of all, the coupled walls must be chosen. In this work only the liner walls are fully subject to the coupling procedure, as shown in Fig. 4.5. Nearest-neighbor interpolation scheme is used to communicate the fields between the solvers because more accurate and costly interpolation schemes (i.e. inverse distance) were tested without appreciable benefits.

CFD solver

A significant part of the whole computational effort in the present procedure is devoted to the solution of the compressible Navier Stokes Equations (NSEs) for a reacting mixture. In particular, employing a steady approach, RANS (Reynolds Averaged Navier Stokes) equations

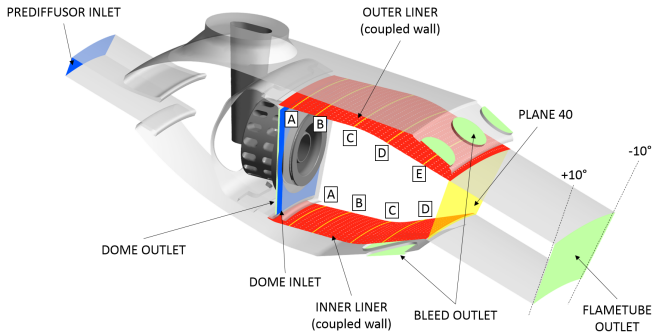

Figure 4.5: Computational domain with measurement locations.

have been solved using a realizable $k-\epsilon$ turbulence model [120] due to its capability in the prediction of the main features of swirling flow fields. Computations have been carried out on the computational grid shown in Fig. 4.6, which was created with ANSYS® Meshing, and consists of nearly 17M tetrahedral elements and 4.6M nodes. It includes the flame-tube as well as the cold sides. From the scheme it is possible to notice the inlet (on the left), where a mass flow rate was imposed, and the outlet where a static pressure was prescribed. Flow split was determined from preliminary RANS simulations with holes modelled through point mass sources using the SAFE (Source bAsed eFfusion modEl) methodology, presented in [121] and applied also in [35]. Temperature at the plenum inlet, operating pressure and mass flow rates were set according to the specific operating condition reported in Tab. 4.1. Boundary conditions at the outlet and inlet patches of the multi-perforation were set relying on the THERM3D methodology. Hence, for each row of effusion holes, uniform pressure outlet and mass flow inlet boundary conditions were applied to keep the chosen flow split, while coolant temperature exiting from the holes is computed at run-time by the dedicated effusion solver. All the uncoupled walls were treated as smooth, no slip and adiabatic. Particular attention has been devoted to wall treatment. Two different methods have been considered to assess the impact on wall heat flux and, consequently, metal temperature. Both scalable wall functions [122] and an enhanced wall treatment, developed in [92] and able to extend the model in all the near-wall regions, have been tested. In the first case 3

prism layers have been employed, whereas in the latter one 10 elements have been used to ensure proper y^+ values. In all the analysed test points a negligible impact of wall modelling on the resulting metal temperatures has been pointed out ($\approx 25\ K$). Therefore, in the following just data obtained with scalable wall functions are discussed for the sake of brevity.

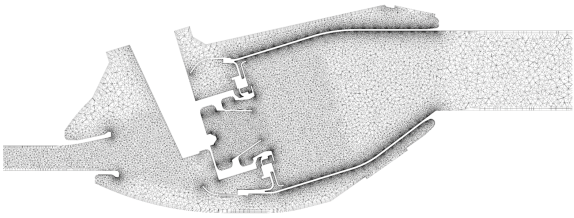

Figure 4.6: Computational grid of fluid domain.

The simulations reported in the present work were performed modelling kerosene as pure $C_{10}H_{22}$ (n-decane), using a detailed reaction mechanism taken from [123] with 96 species and 856 reactions. The manifold for the FGM model was generated using a set of 64x64 non-premixed flamelets. The technical report published by [124] was used to characterize Jet A-1 fuel. Temperature-dependent properties, instead, were applied to the gas phase. In addition, to include the effects of change in composition due to the combustion process, a dependency from progress variable and mixture fraction was formulated.
Spray boundary conditions on the prefilming airblast atomizer were estimated using the Geppert's correlation [102] that provides a physical treatment of the related atomization process, as already observed in Section 2.2.4.

Radiation solver

The radiation between burnt gas mixture and metal, in addition to the gas-gas and solid-solid radiative interactions, are computed by solving the Radiative Transfer Equation (RTE). This is accomplished by freezing the aerothermal field predicted by the CFD solver and the temperature distribution at the walls provided by the heat conduction solver in the previous coupling iteration. As mentioned in the previous section, a dedicated simulation is performed to solve the RTE. A suitable

computational grid on the same CFD domain is generated keeping a good balancing between accuracy and CPU effort. The mesh counts 4M elements and 800k nodes. If compared to the CFD mesh, the element number is strongly reduced thanks to the absence of the prismatic layer and a substantial coarsening of the mesh core, especially in the regions poorly influenced by radiative heat transfer. Boundary conditions for the radiation problem consist of absorbing/emitting walls, inlets and outlets. The phenomenon is modelled by the Discrete Ordinate (DO) model using a 4x4 angular discretization and 3x3 pixels for each direction. The spectral radiation is approximated with a weighted sum of gray gases while metal emissivity is set 0.8. A validation of the radiation modelling approach can be found in [99].

Conduction solver

Solid calculation is characterized by a limited computational cost. Indeed, heat transfer in the liner walls is governed by the Fourier's law and the Heat Equation (HE). Moreover, only the coupled walls (i.e. inner and outer liners) are solved by the conduction solver. The computational domain includes all the 2000 effusion holes, resulting in 21.28M tetrahedral elements and 4.23M nodes. As previously mentioned, at the solid-fluid interfaces wall heat flux provided by the CFD solver is converted in a convective boundary condition, while radiative heat flux is expressed in terms of radiation temperature and emissivity. Heat sink effect in the perforation is modelled recovering the HTC and the average inlet/outlet fluid temperature of each row of holes from the CFD solver. These couple of values are exploited in a convective boundary condition. Solid was modelled as a metal alloy, for which a temperature-dependent thermal conductivity and heat capacity were set.

4.2.3 Results

Results of the simulated operating conditions are here reported. First of all, aerothermal fields are investigated followed by a detailed comparison on metal temperature distributions.

Aerothermal field

The flow field of the different test points is shown in Fig. 4.7 in terms of velocity and temperature distributions.
Velocity fields are similar in all the operating conditions, even if the jet

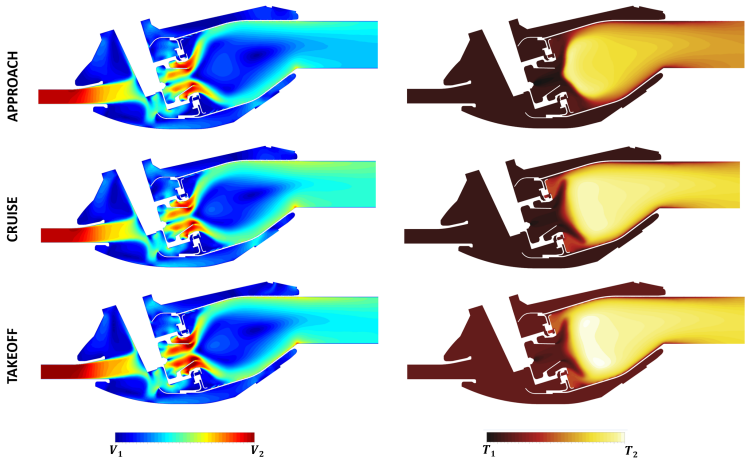

Figure 4.7: Velocity magnitude field (top) and Temperature field (bottom) at the meridional plane for all the operating conditions.

core becomes stronger moving towards Take-Off condition. The high-velocity swirling jet exits from the injector with a large opening angle, impinging on the liner walls and generating a strong recirculation of hot exhaust gases. This widely observed feature, typical of swirling flow, promotes flame stabilization at the low velocity shear between the cold and hot flows, as highlighted by the peak temperature region. A global rise of temperature within the flametube can be appreciated when the FAR increase, as in Cruise condition if compared to Approach test point. However, when P30 and T30 grow up at a fixed FAR value, as moving from Cruise to Take-Off simulation, the augmentation of temperature is relevant only at the cold sides, with a smaller influence on flametube distribution in terms of peak value. In addition, the fuel injection at lip is prevailing at the highest load conditions, leading to burn a small portion of reactant mixture in the corner regions. The temperature fields were compared against experimental data obtained with the rotating probe. A CFD postprocessing on the Plane 40 was performed to provide 1D profiles of RTDF and OTDF, as defined in Eq. 4.1 and 4.2:

$$RTDF(r) = \frac{\overline{T(r)} - T_{40}}{T_{40} - T_{30}} \tag{4.1}$$

$$OTDF(r) = \frac{T(r)^{max} - T_{40}}{T_{40} - T_{30}} \tag{4.2}$$

The results are reported in Fig. 4.8. All the operating conditions show a typical parabolic profile characterized by significant temperature gradients in the radial direction. This is essentially ascribable to the absence of dilution holes capable of controlling the temperature peak at midspan of the exit section as well as the thick layer of coolant generated by effusion.

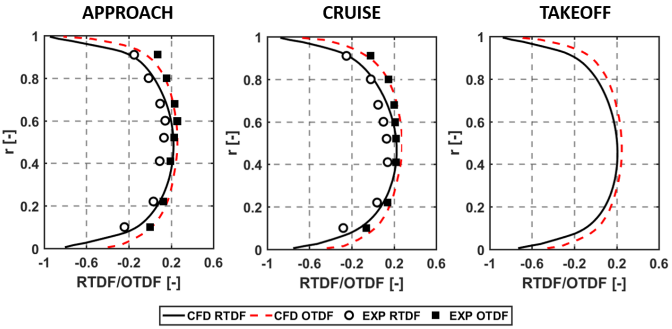

Figure 4.8: RTDF and OTDF profiles at Approach (left), Cruise (center) and Take-Off (right) conditions.

Concerning the comparison against the test data, it is possible to observe overall a reasonable agreement, both for Approach and Cruise conditions, with a consistent slight overprediction. Moreover, it is worth pointing out that the maximum value of RTDF shows a displacement from $r = 60\%$ (Approach) to $r = 40\%$ (Cruise). CFD seems incapable of reproducing such an effect, which may be ascribed to a too dissipative behaviour that could be overcome exploiting more accurate Scale-Resolving Simulations.

Metal temperature

Metal temperature and heat flux distributions resulting from the THERM3D calculation are shown in Fig. 4.9 for all the operating conditions on the hot side facing the flametube. A common peak temperature zone can be observed for all the test points. These spots are related to the increased heat fluxes, which are ascribable to two main effects associated

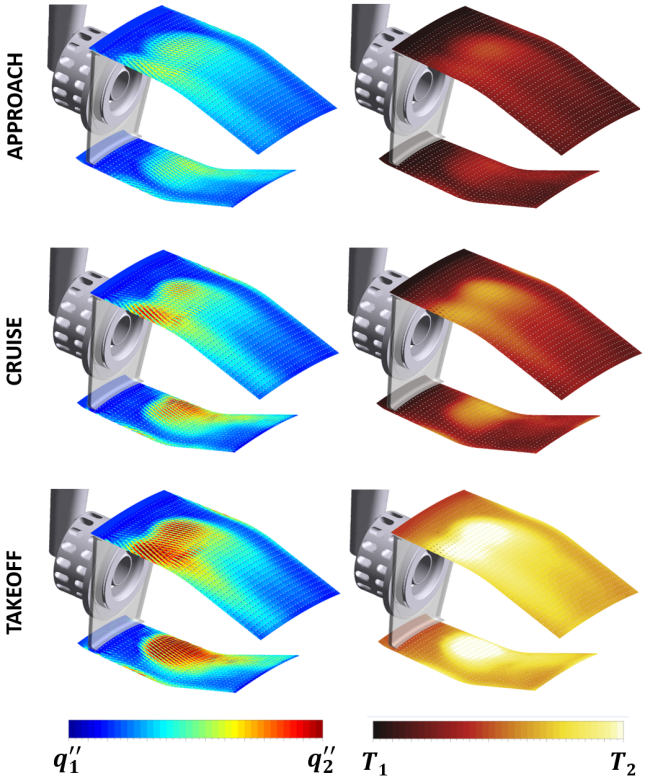

Figure 4.9: Wall Heat Flux (left) and Temperature (right) distributions on the hot side of inner and outer liners for all the operating conditions.

to the impact of the swirling jet on the surface. The first is the increase in heat transfer coefficient for an impinging effect of the jet. The latter is a reduction in film effectiveness caused by the coolant swept away from the liner by flow rotation. Thus, the swirling flow leads to opposite tangential locations of the peak value for the two liners (i.e. inner and outer).
A general heating effect can be observed in Fig. 4.9 moving from Approach to Take-Off, associated to higher heat fluxes. A prominent temperature increase is shown by Take-Off contour and confirmed more quantitatively

in Fig. 4.10. The picture reports, both for inner and outer liners, the area-averaged hot side metal temperature and the energy budget, represented by surface integrals of convective (CONV) and radiative (RAD) heat fluxes on hot (HS) and cold (CS) sides, as well as the heat sink (EFF) contribution. On the hot side, convective and radiative heat transfer

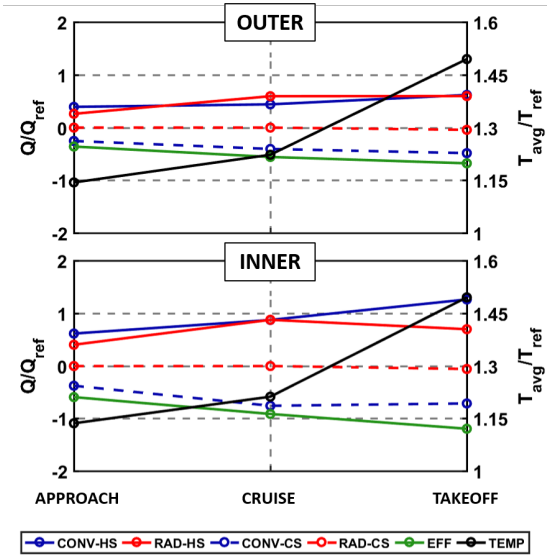

Figure 4.10: Normalized energy budget and mean temperature on Outer (top) and Inner (bottom) liners for all operating conditions.

are comparable, unlike the cold side. In that case radiation is almost negligible in all the test point, which can be justified by the cold side aerothermal condition. In fact, this region is characterized by a channel flow with a temperature slightly higher than T30, wetting the liner on one side and the casing on the other one, where an adiabatic boundary condition is applied. The view factor between these surfaces can be assumed equal to 1, so that only their mutual radiative heat exchange can be considered. Since the casing reaches the T30 temperature, the difference between the two wall temperature is small and the radiative heat fluxes are not appreciable. This is confirmed by Take-Off condition, where an abrupt increase in metal temperature is not accompanied by a larger contribution of radiation, which can be explained keeping in mind

the characteristics of the operating conditions (see Tab. 4.1). On the hot sides, while the convective term shows a monotonous trend increasing the burner thermal load, the radiative heat transfer curve highlights a maximum at Cruise condition followed by a slight reduction at Take-Off. In fact the FAR value between these simulations is unchanged and the flame is only slightly hotter, even if T30 rises by $\approx$ 200 K when moving to Take-Off. Consequently, the metal undergoes a strong warming caused by T30 as well as by the higher pressure P30 that increases the heat transfer coefficients. Temperature difference on the hot side becomes smaller, thus reducing the radiative load while convective fluxes grow strengthened by the higher HTC. Concerning the heat sink, it is relevant and increases moving towards Take-Off, even if the higher T30 limits the increase associated to the higher wall temperatures.
The different contributions to the liner heat load can be observed more effectively in Fig. 4.11, reporting the energy budgets on bar graphs for the inner and outer liner in the different test points. The graphs have

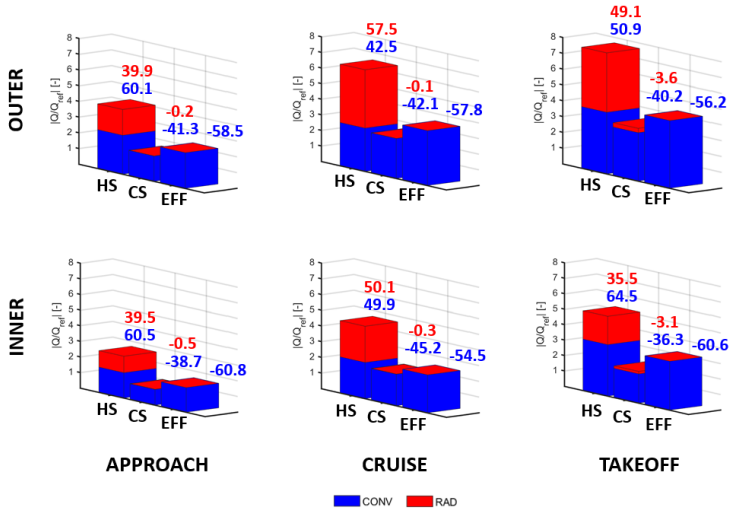

Figure 4.11: Energy budgets for the outer and inner liner in the different operating conditions.

separate bars for the hot side (HS), cold side (CS) and effusion (EFF). Each bar represents the absolute value of the normalized heat loads. The

HS bar and CS bar have both the convective (blue) and radiative (red) terms. Fig. 4.11 shows promptly the increase of heat load moving from Approach to Takeoff as well as the weight of radiation on the hot side. The numbers at the top of the bars, coloured as the heat transfer modes, are the relative contribution (in percentage) of the heat transfer modes to the total incoming or outgoing heat load. The liner is cooled for about 60% by effusion and 40% by cold side, almost independently by the operating condition. On the hot side, instead, convection dominates on radiation at Approach while the latter becomes more relevant at higher loads on the outer liner.
Quantitative comparisons of metal temperatures with experimental data are reported in Fig. 4.12 and Fig. 4.13, respectively for outer and inner liners. Results are normalized with respect to a reference temperature and shown for all the operating conditions as circumferential distributions in an angle range of -10°/+10° at different axial locations (see Fig. 4.5). Approach test point is in good agreement with measurements on outer liner but a certain underestimation is observed on B and C locations on inner liner. At Plane A the uniform profile can be ascribed to the homogeneous highly-effective slot cooling. At downstream sections the strong interaction between walls and swirling jet leads to a double-peak value on the outer side at positive angles while a single-peak value on the inner liner at negative angles, accordingly with flow rotation. Moving to Cruise condition a general increase of metal temperature is shown both in measurement and numerical data due to the higher gas temperature, even if this rising is more prominent in experiments. The disagreement is more evident in the first measurement planes where the different P/T of the two test points should lead to different spray evolution and flame behaviour, badly reproduced by these RANS as seen in Fig. 4.7. Such a limit could also negatively affect the prediction of radiative contribution. However in the downstream locations a better agreement is recovered because the less influence of flame structure on aerothermal field, which is close to equilibrium temperature with roughly uniform velocity.
Concerning the Take-Off, Fig. 4.14 highlights as the temperature profiles are even more shifted towards high values as already seen in Fig. 4.9. From a numerical point of view, the shape of the profiles is quite similar varying the operating condition, confirming a similarity in the metal temperature distribution, previously suggested by Fig. 4.9.

Sensitivity analysis

As shown in Fig. 4.10 the mean liner temperature increases moving from Approach to Take-Off but a greater slope is obtained moving from

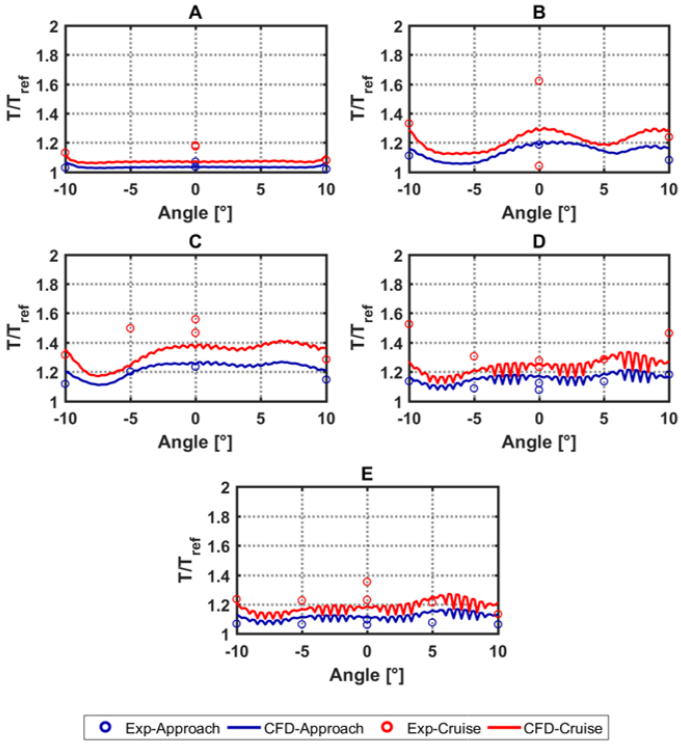

Figure 4.12: Circumferential profiles of normalized metal temperature compared with experiments at different cross sections on the outer liner.

Cruise to Take-Off. Here the increase is about 20%, while it stops to 10% moving from Approach to Cruise. A further investigation to the temperature trend was carried out. For this purpose a 0-D model of an equivalent annular combustor was built with global parameters according to the investigated burner. Inlet conditions were adjusted to the three flight operations. A sensitivity analysis on key variables of the model was performed to find the parameters and the main uncertainties affecting the solid temperature in the present CHT problem. The chosen quantities, depicted in Fig. 4.15, are: inlet temperature ($T30$) and pressure ($P30$), fuel-air ratio (FAR), adiabatic effectiveness (η_{ad}) and

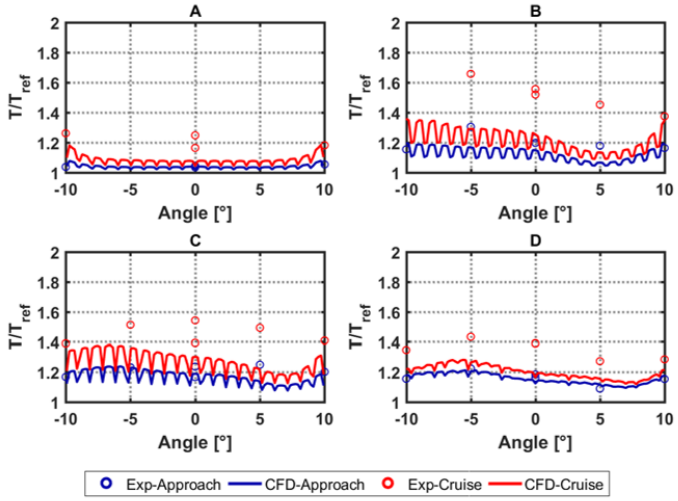

Figure 4.13: Circumferential profiles of normalized metal temperature compared with experiments at different cross sections on the inner liner.

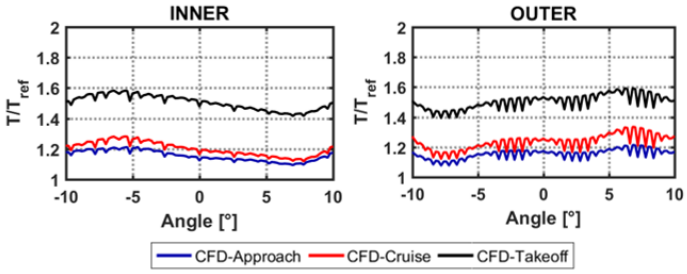

Figure 4.14: Circumferential profiles of normalized metal temperature for Approach, Cruise and Take-Off test points at Plane D.

heat transfer coefficients (HTC_{hs}, HTC_{cs}). All these parameters were normalized to the Cruise value. The analysis prove that T30 drives the metal temperature trend because it has a direct impact on both the gas

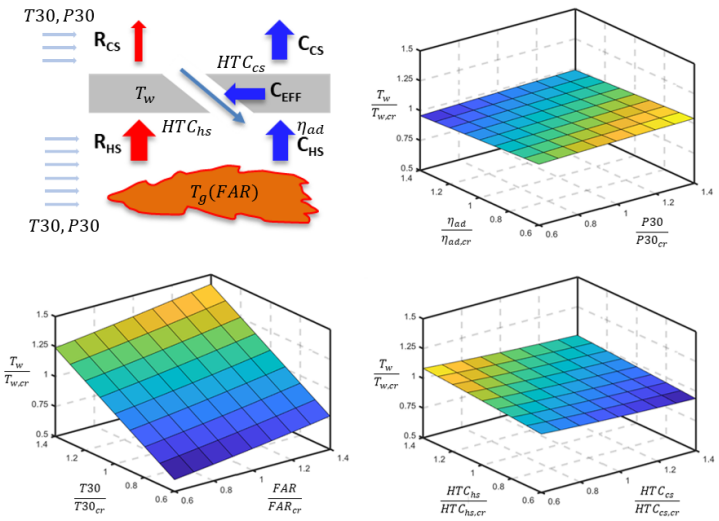

Figure 4.15: Sensitivity analysis to model parameters for the 0-D simulation.

and coolant temperatures that are the reference temperatures for the convective heat transfer processes. This result explains the higher growth rate of temperature moving from Cruise to Take-Off observed in Fig. 4.10.

4.3 High-fidelity design

Prediction of accurate metal temperatures inevitably requires an appropriate solution of the gas velocity and temperature fields that, in turn, are strongly affected by the interactions occurring in turbulent spray flames between spray evolution, turbulence and combustion, as widely stressed in Section 2.2. Scale-Resolving Simulations are able to overcome the main limitations of classical RANS approaches and have been successfully exploited for simulations of reactive multiphase flows. Significant efforts have been focused in the past also on other scale-resolving modelling strategies for turbulent spray flames distinguished mainly for what concerns the turbulence-chemistry interaction.

4.3.1 Numerical details

Several numerical aspects of the previous THERM3D simulations were adopted in the following high-fidelity simulations as combustion, spray and radiation modelling. However, the conflicting needs of a more accurate prediction of the aerothermal field and an affordable computational cost, have found in Scale Adaptive Simulation the proper turbulence model for the present complex geometry. Pressure-velocity coupling was solved by the pressure-based SIMPLEC (Semi-Implicit Method for Pressure Linked Equations-Consistent) algorithm for the convective solver. Second order schemes were adopted to discretize both the advection and temporal terms. According to the unsteady simulation and the U-THERM3D method, a time-step of 3e-6 s and 1e-3 s were set for the fluid and solid, respectively. Coupling between the two domain was carried out every 10 fluid time-steps and 30 solid time-steps.

Domains

Computations have been carried out on the domain shown in Fig. 4.16, that is a simplified version of the domain shown in Fig. 4.5 where the annulus and the upstream diffuser are removed. As a result, in order to reduce computational time keeping a good accuracy, the gas phase domains needed for solving the convective and radiative problems include the flametube and an upstream plenum. Indeed, the main benefits of a SRS are appreciated within the flametube because of the strong interaction between turbulence, combustion and spray evolution. Moreover, the focus of present manuscript is on the high-fidelity prediction of metal temperature, that is mostly affected by the unsteadiness on the hot side. This simplification has even less effects on the radiative fluxes, that are negligible in the annulus if compared with the convective ones as reported on energy budgets in Fig. 4.11. It is worth mentioning that in order to replicate the fuel staging strategy adopted at Idle condition (9 active injectors out of 18), only one sector has been simulated. To model the presence of the sectors with unfed fuel injectors, the emissions have been corrected with an ideal mixing between the concentration calculated for the burning sector and pure air from a turned off sector. As shown in Fig. 4.16 and according to the present loosely coupled approach solid conduction is computed in a physically-separated domain representing the inner and outer liners. Indeed, being the metal opaque for radiation,

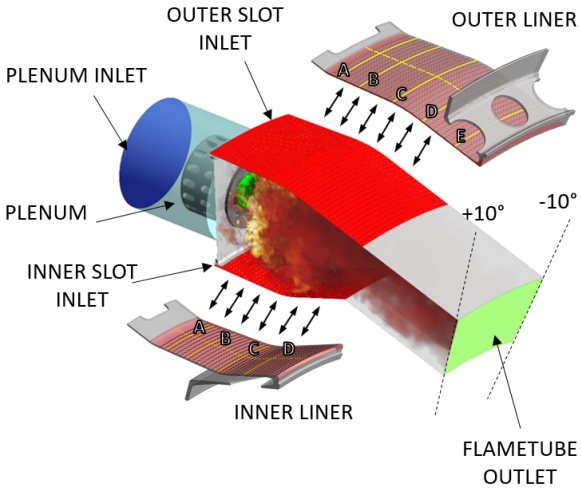

Figure 4.16: Computational domains and main boundary conditions.

beams can be only absorbed or reflected at the fluid-solid interface and the computation of radiation is not required in the solid domain.

Computational grids

The different requirements for the involved computations were taken into account during the generation of the three meshes with ANSYS® Meshing. Mesh for the convective problem consists of nearly 8.7M tetrahedral elements and 2.1M nodes with a sizing smaller than in RANS mesh, as required by a SAS approach. As in the near-wall region the SAS model behaves as a RANS k-ω SST model, to exploit a wall function approach [125] the mesh counts 3 prismatic layers at wall and a y+ in the range of applicability for this wall treatment. The adequacy of the mesh was evaluated *a posteriori* using Pope's criterion [126], verifying that most of the domain ensures a resolution of at least 80% of the turbulence spectrum. Radiation and solid meshes, instead, were recovered from the THERM3D computation. It is worth remember that, as estimated in Section 2.1.2, the use a loose coupling for the fluid-radiation interaction together with a mesh coarsening can reduce the computational effort of

the coupled problem of around $30 - 40\%$.

Boundary conditions

The boundary conditions were chosen with the same criteria adopted in the THERM3D simulations. However, concerning the convective domain, the plenum inlet represented in Fig. 4.16 is now the main inlet where the only mass flow passing through the injector was applied, according to the prescribed flow split discussed in Section 4.2.2. Coolant temperatures provided by the THERM3D simulations for each row of the multi-perforation were set on the inlet patches representing the exit of the holes and kept constant during the whole calculation. This assumption is justified by the small temperature jump of coolant through the multiperforated liner. The hot sides of the two liners (red regions in Fig. 4.16) were coupled with solid and, for this purpose, coupling boundary conditions were applied. The results of the steady THERM3D analysis on the full geometry, instead, were exploited to deduce the heat transfer coefficients and the reference temperature for the cold side as well as the wall of effusion holes in the solid simulation.

4.3.2 Flametube adiabatic analysis

To pave the way for Conjugate Heat Transfer simulations, adiabatic analysis on the 4 test points were carried out, so having a deep insight on the aerothermal fields and make sure about the capabilities of the modelling strategy. Such an ideal condition was investigated within the flametube and, for this reason, all the walls were treated as smooth, no slip and adiabatic.
This section is therefore structured as follows:

- Description of the aerothermal field, so as to highlight the main features of the velocity and temperature fields as well as their variations at the different test conditions.

- Analysis of the resulting temperature profiles at the combustor exit in terms of RTDF and OTDF and comparison against experimental data.

- Considerations about the formation of pollutants (CO and NO_x) and comparison in terms of emission index at the combustor exit.

Aerothermal field

The velocity fields generated within the combustion chamber are shown in Fig. 4.17. It is possible to observe that the injection system generates a large swirling flow that interacts with the liners and extends almost up to the exit of the chamber. The velocity in the swirler shows a slight increase moving towards the Take-Off condition, however the nature of the flow field is substantially preserved changing the test point.

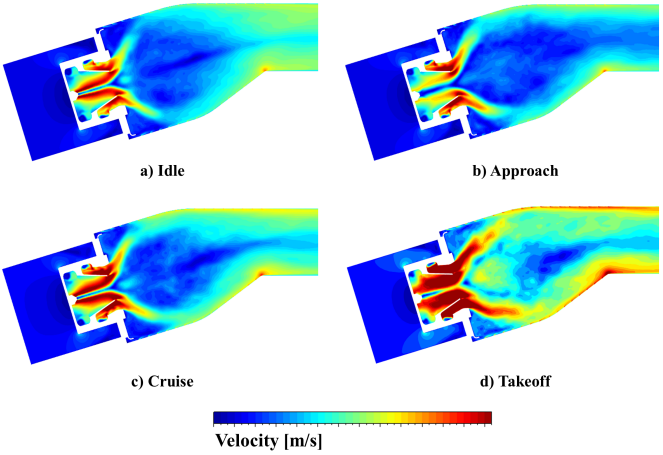

Figure 4.17: Contours of the mean velocity magnitude at different conditions.

More interesting conclusions can be drawn from the instantaneous and mean temperature maps reported in Fig. 4.18. At Idle condition all the fuel is injected through the pressure atomizer at the pilot and forms a liquid film that breaks up at tip of the injector lip. In the absence of an appropriate modelling for the thin film, this process is modelled applying a spray injection at the above-mentioned tip, with a distribution estimated with the correlation proposed by Gepperth [102]. The spray generated has a rather high SMD ($\approx 68\ \mu m$), resulting in a flame stabilized downstream if compared to the other test points. It is also worth mentioning that at Idle the combustor would be operated with a circumferential fuel staging, on the basis of which only 9 of 18 sectors are ignited. Clearly, the interaction of the flame with the adjacent cold swirling flow is completely missing, since we are considering only the burning sector. It is reasonable

to expect that this phenomenon would have a significant impact on the temperature profile and the emissions at the combustor outlet, which is neglected at the moment.

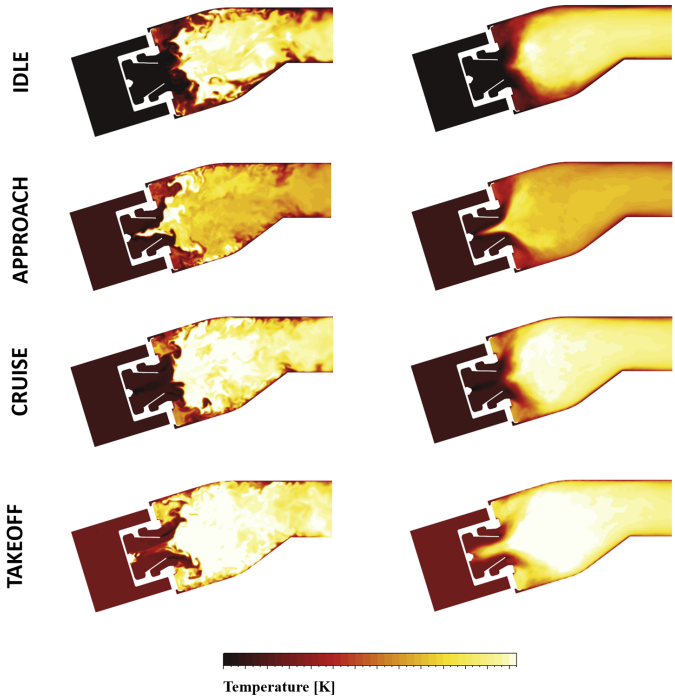

Figure 4.18: Contours of instantaneous (left) and mean (right) temperature at different conditions.

Considering the Approach condition, the increase in the FAR is sufficient to achieve a stable combustion process in each sector, provided that the flame is piloted with at least 70% of the fuel. The reaction appears confined within the swirling flow, with a tendency to propagate upstream within the swirler.
It is interesting to notice that at Cruise condition, operated with same P_{30} and T_{30}, but different FAR and P/T, the resulting temperature field appears significantly affected. Most of the fuel (90%) is injected at the lip,

evaporating directly within the swirling flow and generating a recirculation region at relatively uniform temperature. The reduction in P/T generates a leaner mixture that prevents the ignition process with the swirler. On the contrary, the higher amount of fuel directed to the main injection gives rise to a non-negligible turbulent transport of fuel in the corner recirculations, thus increasing the temperature.
This phenomenon is evident also at Take-Off, with the difference that, given the flammability limits extended by the higher inlet pressure and temperature, a tendency to flashback occurs similarly to what highlighted at Approach. Interestingly, additional Scale-Adaptive Simulations have shown that in transient simulations this effect is subject to hysteresis depending on the initialisation conditions.
Once highlighted the impact of the different operating conditions on the aerothermal field, it is possible to show and discuss their impact on the resulting temperature profiles at the combustor exit.

Temperature profiles at combustor exit

The temperature fields were postprocessed on the Plane 40 so as to obtain the 1D profiles of RTDF and OTDF. The comparison against the experimental data obtained with the rotating probe is reported in Fig. 4.19. Only Idle is characterized by high temperature lobes in the proximity of the liners that propagate up to the combustor exit. As for RANS results, all other conditions show a typical parabolic profile. Concerning the comparison against the test data, it is possible to observe overall a reasonable agreement for both Approach and Cruise conditions, with a consistent, slight overprediction of the RTDF.
Fig. 4.20 shows the temperature distribution at the Plane 40 in terms of mean and fluctuating component, the latter expressed as the ratio of root mean square to local mean temperature value. While the peak of mean temperature is located at midspan, the highest fluctuations occur at wall because of the film cooling.

Emissions

A further comparison was performed considering the pollutant emissions measured with the rotating probe, focusing on CO and NOx. The Emission Index (EI) of each pollutant depending on the operating condition is depicted in Fig. 4.21. As it is possible to notice, the experimental dataset shows some scattering that is ascribable to a non-exact repeatability of data obtained from the rotating probe during successive measurements. CFD is instead plotted calculating the time-average value

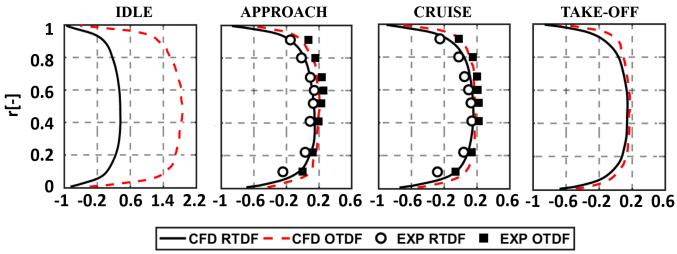

Figure 4.19: RTDF and OTDF profiles at different operating conditions.

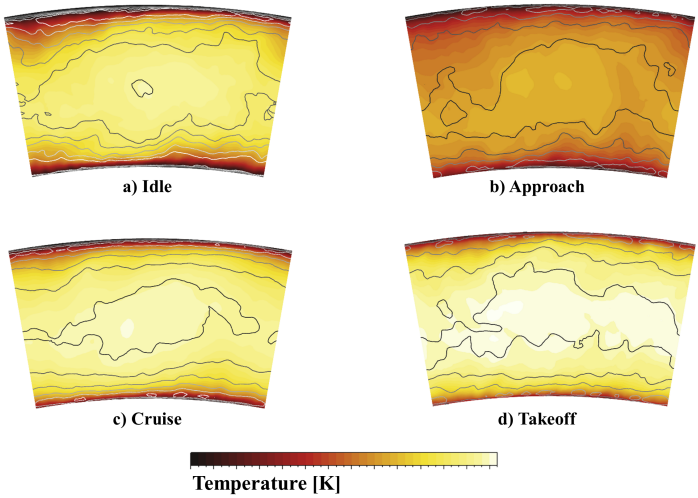

Figure 4.20: Mean temperature distributions at Plane 40 section overlapped by contour lines of temperature RMS normalized to the local mean value (black-to-white scale representing value from 0% to 30%)

collected during the data sampling, while the standard deviation was superimposed to represent the potential oscillations showed in the time evolution.
The estimation of CO emissions proved to be challenging and CFD shows a tendency to slightly overestimate the concentration at the burner exit.

The Idle condition deserves a special consideration, especially bearing in mind that we are neglecting the interaction with the adjacent cold sector. This would reasonably produce local quenching phenomena of the flame that can be associated to an increase in the production of CO. The simulation of the dual sector configuration would be challenging and worth of attention but will be considered in the future. Nevertheless, it should be pointed out that overall a reliable prediction of the absolute values of the CO levels is determined and this leads to a further assessment of the numerical setup here employed. Going from Idle to the Take-Off operating conditions, as expected, the level of carbon monoxide is progressively reduced and the trend numerically predicted is in line with experiments. The scenario is similar for what concerns NO_x (Fig. 4.21), as CFD matches both the measured values and the overall trend quite closely. Nevertheless, considering the complexity of the geometry under investigation as well as the unavoidable uncertainty on experiments in this challenging operating conditions, the achieved agreement is satisfactory mainly from an industrial point of view.

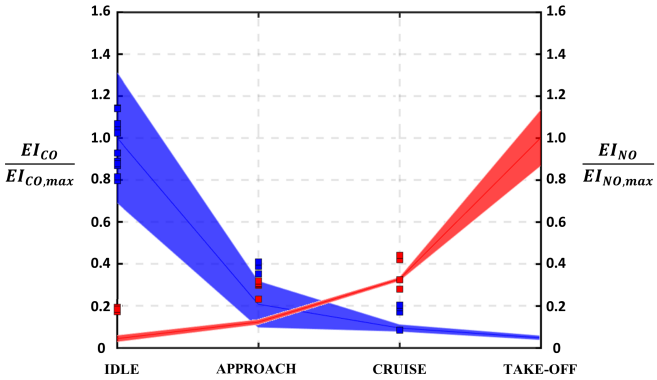

Figure 4.21: Comparison of CO (blue) and NO (red) emission index at different conditions.

Once validated the numerical methodology, the efforts are devoted to provide a better understanding of the impact of the operating conditions on flame, spray evolution and pollutant formation. At this purpose, a regime indicator has been introduced to highlight the regions where the flame presents a premixed or diffusive behaviour. The flame index Θ has

been defined in the present work as suggested by [127]:

$$\Theta = \left(\frac{\nabla Y_F \cdot \nabla Y_O}{|\nabla Y_F \cdot \nabla Y_O|} \right) \tag{4.3}$$

where Y_F and Y_O are respectively the fuel and oxidizer mass fractions. It must be stressed that the chosen definition of the flame index has some limitation to investigate the physics of spray combustion [128], but can be quickly evaluated for a preliminary assessment of flame evolution. It is typically argued that a positive value of Θ indicates a local premixed combustion and that a negative value states a diffusive condition.
In Fig. 4.22 the evolution of Θ obtained through numerical simulations in all the investigated conditions is reported clipping the distribution on flammability range, which has been evaluated as 0.4 and 1.5 respectively for lean and rich limits in terms of equivalence ratio. On the same contour plots, iso-lines corresponding to a liquid volume fraction α_l=0.01% are shown in green in order to point out the zone characterized by the presence of the spray. Instead, blue and red markers specify iso-values of CO and NO_x equal to respectively the 80% and 50% of their local maximum. These contours should give an idea about where pollutant emissions are mainly generated and the corresponding burning mode, which can be useful information from a design point of view. To ease the discussion each test point is individually analysed:

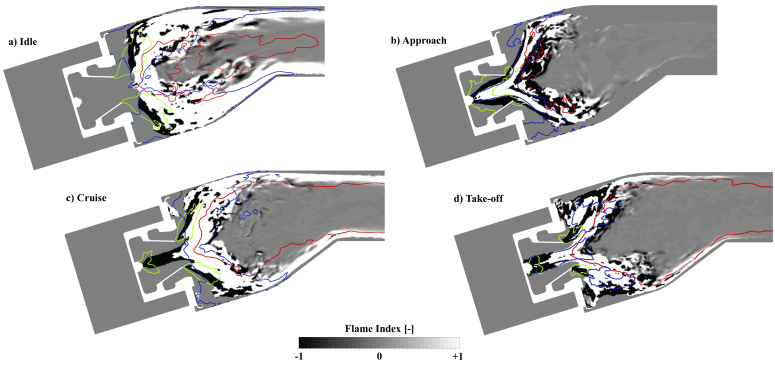

Figure 4.22: Contours plots of instantaneous flame index obtained in all the analyzed test conditions. Iso-lines show the presence of the spray (green) and the concentration of CO and NO (blue and red respectively).

- At Idle, all the spray is injected at the lip and a non-premixed front is initially created, stabilising two regions at high temperature near the liners where CO is produced. This corresponds also to the two lobes at high temperature in Fig. 4.18.

- At the operating condition corresponding to Approach, the higher temperature and pressure lead to a strong evaporation of the liquid fuel injected at the pilot. Here the 70% of fuel is injected in this location and the kerosene vapour generated in this way leads to the stabilization of a premixed flame, which is characterized by a V-shape and arrives inside the injector. Carbon monoxide is mainly produced in this region and follows such premixed burning zone. Immediately downstream, a non-premixed region is instead determined, probably created by the part of the spray that has still to be evaporated. This determines the zone at higher temperature and heat release shown in Fig. 4.18 and also to a major production of NO_x.

- At Cruise, the major part of fuel is injected at the lip. The corresponding region presents a dual burning mode: smaller particles, which are characterized by lower Stokes number and tend to follow the swirling jet on the spray edge, quickly evaporate and burn with a dominant premixed burning mode. Conversely, bigger droplets are probably gathered at the center of the spray and create a diffusive region. A leading premixed flame front is predicted and once again is associated with a major production of CO. A pocket of hot gases is stabilized at the center of the burner, determining a high generation of NO_x. It is interesting to point out that, with respect to the Approach condition, production of CO and nitrogen oxides are here super-imposed.

- At Take-Off, a flame structure similar to Cruise is predicted even if, thanks to the higher pressure and temperature, the flame is stabilized inside the injector. A leading premixed burning mode is predicted and regions immediately after the injection points are associated to a production of both CO and NO_x.

Adiabatic wall temperature

Before moving to the multiphysics coupled simulations, the adiabatic wall temperature was investigated in both RANS and SAS flametube simulations. This analysis is helpful to have a preliminary indication about the zones of the liner most affected by a scale-resolving modelling. Indeed,

the adiabatic wall temperature is strictly related to the adiabatic effectiveness (i.e. the film cooling protection) and the local gas temperature. Differences in this quantity between steady and unsteady approaches in terms of mean value suggest a different prediction of the aerothermal field as well as the swirling flow-wall interaction. Moreover, the instantaneous values obtained by a SAS simulation provide an estimation of the involved frequencies in the heat transfer process which can be exploited to set the coupling parameters in the U-THERM3D simulation.
Fig. 4.23 shows the mean adiabatic wall temperature in the Approach and Cruise SAS simulations, highlighting a substantial increase moving to Cruise according to the THERM3D results on metal temperature shown in Fig. 4.9. A comparison of the gas and wall temperatures between

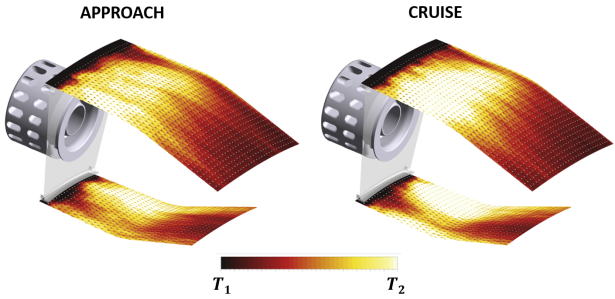

Figure 4.23: Comparison of mean adiabatic wall temperature for SAS simulations of Approach and Cruise conditions.

RANS and SAS adiabatic simulations of the flametube at Cruise operation is depicted in Fig. 4.24.
The strong non-linear temperature-dependence of radiation can lead to considerable inaccuracies in the prediction of radiative thermal load when a RANS approach is exploited because of the absence of temperature turbulent fluctuations, which would not be taken into account by the DO model. SAS is instead capable of resolving the largest turbulence scales and fills in this fashion the aforesaid deficiency of the RANS-DO modelling approach. In addition, the unsteady aerothermal field can affect the gas-wall interaction, as suggested by the mean SAS wall adiabatic temperature, leading to different convective heat fluxes in an unsteady application of the THERM3D procedure. These two aspects are more pronounced in the jet-wall interaction region, as shown in the bottom

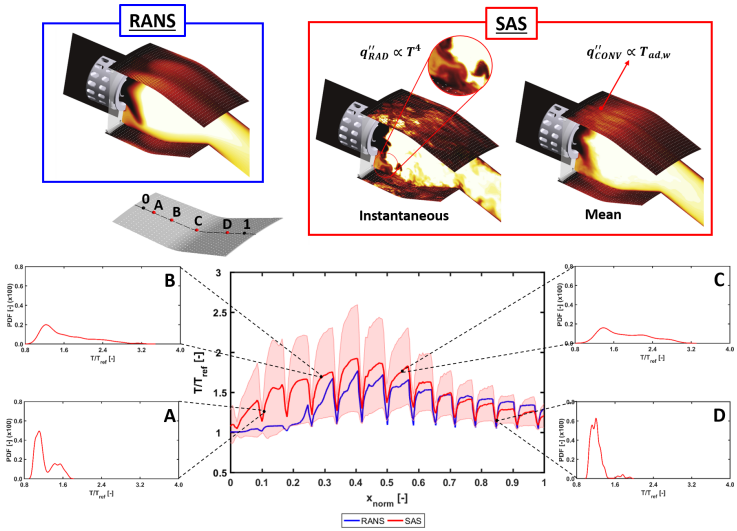

Figure 4.24: Detailed analysis of temperature field of RANS and SAS adiabatic simulations for Cruise condition, with focus on the temperature distribution and Probability Density Functions on the inner liner centerline (the red band represents the SAS temperature standard deviation value).

plots of Fig. 4.24 for the inner liner. The major plot compares adiabatic wall temperature for RANS and SAS simulations along the centerline superimposed by a red band representing the SAS temperature standard deviation. The minor plots instead are focused on the Probability Density Functions (PDFs) of instantaneous temperature obtained by a sampling process on four points of the SAS simulation (i.e. A,B,C and D in Fig. 4.24). SAS mean temperature is definitely higher than RANS one in the first 30% of the liner, while temperature fluctuations are relevant for over 50% of the length. On the contrary, close to slot inlet and effusion holes the temperature variance is locally lower since it is affected by uniform inlet conditions as well as in the final region, where the turbulence is drastically reduced and combustion is almost completed. A deeper analysis on the time-history of wall adiabatic temperature reveals different PDFs depending on the location and therefore on the flow field conditions.

Points B and C show a broad temperature distribution due to the strong interaction with the swirling flow and a mode value close to the coolant temperature, where the shift can be related to the adiabatic effectiveness. Points A and D, closer to effusion holes, have instead a narrower bimodal distribution. This bimodal behaviour is particularly evident for Point A, where the highest peak value can be associated to the effusion and slot cooling. The lowest peak, instead, is generated by the jet-wall turbulent interaction, as widely above explained. This final analysis on adiabatic simulations suggests as the differences in the computation of wall quantities in a SAS approach could be relevant if compared to the more common steady framework. However, further investigations are required to assess the predictive capabilities of metal temperature in Scale-Resolving Simulations.

4.3.3 Multiphysics investigation

As a result of what depicted in Fig. 4.24, the present section tries to be the missed link between the steady CHT analysis presented in Section 4.2 and the scale-resolving investigation within the flametube shown in Section 4.3.2. In this section the results of the test points investigated with the U-THERM3D tool will be presented, compared with the THERM3D results and discussed. First of all, the Approach condition was simulated, analysed and compared against the experiments. Then, the present tool was applied on the Take-Off condition.

Approach

The aerothermal field is strongly influenced by the double swirler configuration that creates a swirling flow with a large inner recirculation zone and two outer recirculation zones in the corners between dome and liners as widely discussed in Section 4.3.2. A major part of liquid fuel is injected in the pressure atomizer (see Tab. 4.1), which breaks it up in droplets. These particles evaporate partially in the inner duct, contributing to feed the hot gases ingestion that periodically occurs within the swirler from the downstream recirculation zone. This behaviour can be observed in Fig. 4.25 showing the temperature field in the combustor. While the timeframe chosen for the instantaneous temperature does not seem to be subject to flashback, the mean field highlights that gas at high temperature is present up to the pilot injector as already observed in Fig. 4.18.
The core region of the flametube is unaffected by the coupled simulation at Approach if compared to the adiabatic simulation reported in Section 4.3.2. The shear stresses and high velocities caused by the burner promotes the

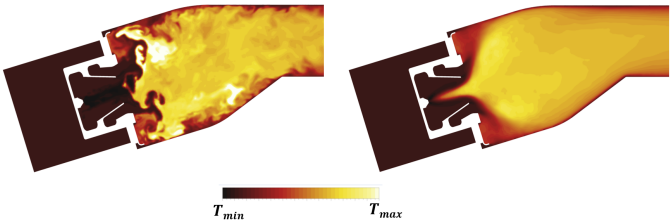

Figure 4.25: Contours of instantaneous (left) and mean (right) gas temperature at Approach condition.

breakup of fuel film flowing on the airblast atomizer, the turbulence of jets and, as a results, the subsequent dispersion of the liquid particles as well as of the evaporated fuel. Large eddies trap the fuel into pockets where it is mixed and burnt, leading to hot spot regions moving downstream. These turbulent structures interact in a non-stationary fashion with the liners increasing convection and, therefore, wall heat transfer. Such a phenomenon was investigated in Fig. 4.24 on the adiabatic simulation, highlighting the differences between RANS ans SAS in the prediction of the mean adiabatic wall temperature and the wide range of its fluctuations in the upstream region of the liner. Turbulent energy redistribution in the flametube has a key role in the heat transfer process as shown in the corner regions, where the mean temperature is definitely higher than the one obtained in Section 4.2. This property is typical of SRSs that are able to solve a portion of turbulent diffusion.
In Fig. 4.26 the instantaneous and mean energy source term due to radiation is shown, representing the data sent from the radiative to the convective simulation. Even if absorption and emission properties depend on species composition, the temperature is the main quantity affecting the energy source. The flame region has negative values and the higher the temperature, the more negative the source. On the other hand, low temperatures in the mixing regions between film cooling and flue gases provide an absorption of radiative energy.
Focusing on the two liners, the resolved part of turbulent convection affects the prediction of metal temperature if an unsteady coupling is exploited. Fig. 4.27 shows the temperature distribution on the hot side of the liners for the THERM3D and U-THERM3D simulations together with the relative difference (in percentage) between the latter and the former normalized by the THERM3D value (in [K]). If compared to the

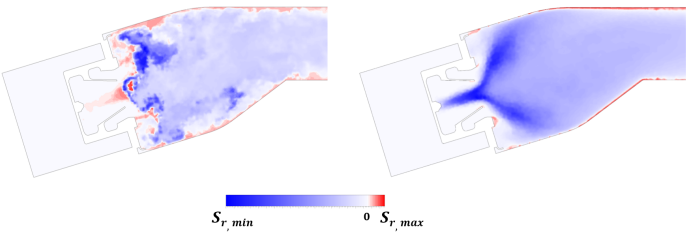

Figure 4.26: Contours of instantaneous (left) and mean (right) energy source term due to radiation at Approach condition.

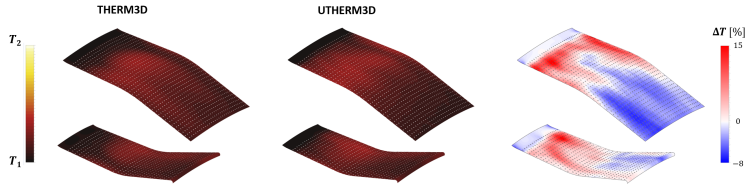

Figure 4.27: Contours of mean temperature on the hot side of the liners for the THERM3D (left) and U-THERM3D (middle) simulations at Approach condition. The percentage difference between the U-THERM3D and THERM3D temperature normalized by the THERM3D value (in [K]) is also reported (right)

steady result, U-THERM3D predicts a broader high-temperature region and a smoother distribution. Indeed, the turbulent interaction between swirling flow and walls is detrimental for the film effectiveness of both the slot and effusion. Opposite cold streaks appeared on the two liners in the THERM3D modelling as the coolant is not disturbed by the swirling flow, maintaining a good protection. This feature disappears completely in the present simulation because of an increased jet opening angle of the swirling flow related to the unsteady treatment. As a result, in this region, temperature rises around 15% compared to a steady RANS coupling. Similar values are observed immediately downstream of the slot exit for the presence of hot gas recirculation in the corners. The liners show two different trends: the first half region is warmer but the downstream zone has lower temperatures.
A quantitative comparison with measurements of the liner temperature

on the cold side reveals the improvements of the present multiphysics tool in the prediction of liner thermal load, as reported in Fig. 4.28, 4.29 and 4.30 in terms of normalized temperature. The data were extracted on the lines highlighted in the sketch of Fig. 4.16.

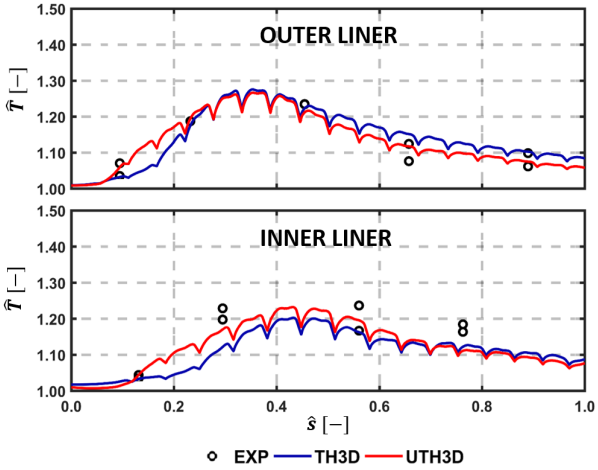

Figure 4.28: Comparison of the centerline temperature between experiments, THERM3D and U-THERM3D on the cold sides of the Inner Liner (top) and Outer Liner (bottom) at Approach condition.

Fig. 4.28 shows the temperature distribution of both the liners along the centerline, expressed as normalized curvilinear abscissa $\hat{s}$. The curves confirm the higher heat load of the U-THERM3D simulation at upstream locations already observed in Fig. 4.27, especially for the Inner Liner. On this side, the numerical results are shifted towards measurements. The Outer Liner temperature, instead, was already well-predicted by THERM3D but the present approach, anyway, shows a further improved trend. For instance, on the first measurement point a better agreement is obtained thanks to the smoothing effect of temperature gradients.
Analogous comparisons can be performed on the spanwise lines depicted in Fig. 4.16 and the results are reported in Fig. 4.29 for the Outer Liner (lines A,B,C,D,E) and in Fig. 4.30 for the Inner Liner (lines A,B,C,D). Once again, U-THERM3D predicts smoother tangential distributions of metal temperature, in particular at B and C locations of the Inner Liner. While in RANS the swirling flow keeps a good film protection up to the

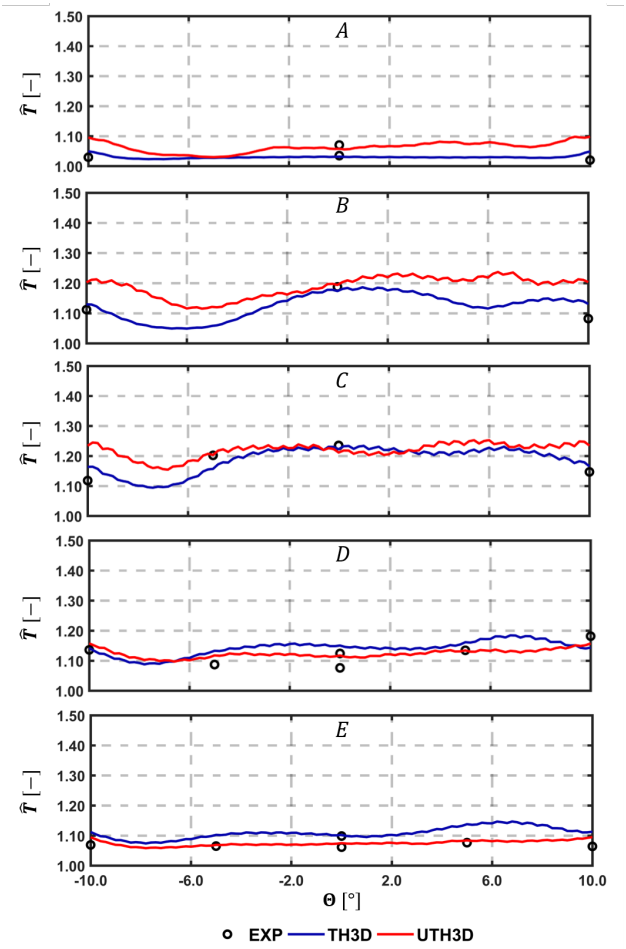

Figure 4.29: Comparison of the spanwise temperature between experiments, THERM3D and U-THERM3D on the cold sides of the Outer Liner for the locations depicted in Fig. 4.16 at Approach condition.

fifth row of holes, in SAS computation the hot gases disrupt the coolant layer before the second row leading to a higher thermal load at line A that is confirmed by experiments. This interaction, however, is excessive

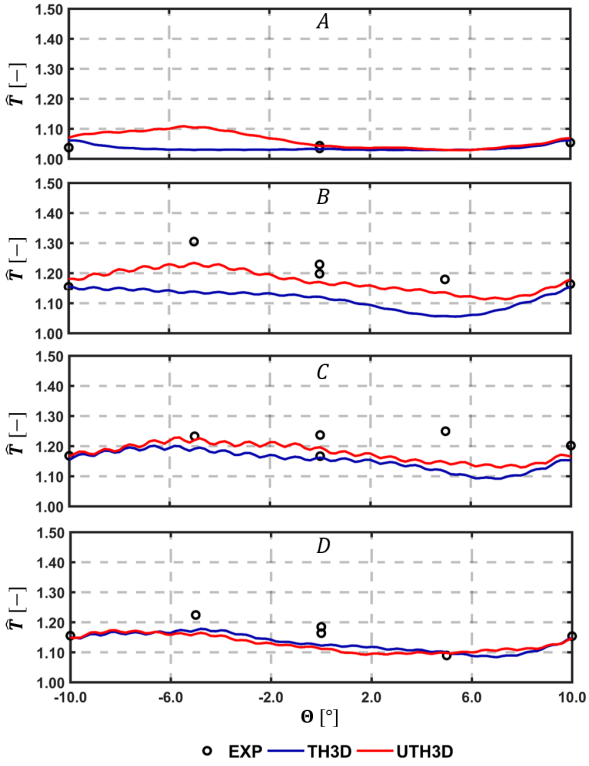

Figure 4.30: Comparison of the spanwise temperature between experiments, THERM3D and U-THERM3D on the cold sides of the Inner Liner for the locations depicted in Fig. 4.16 at Approach condition.

at -10/10° locations on the Outer Liner resulting in an overestimated metal temperature. A general improvement in the distributions could be obtained revising the boundary conditions applied to the effusion holes. Indeed, a constant mass flow rate was chosen for each row but the pressure distribution is not uniform in the tangential direction. This is particularly expected on the hot side because of the impinging of swirling flow on the liner walls that increases locally the pressure. This phenomenon is more relevant in the centerline region, resulting, in the hypothesis of uniform pressure on the cold side, in a decrease of pressure drop and, hence,

in lower mass flow rate compared to the uniform injection. Obviously, more coolant will be injected from the holes close to -10/10° locations if the same total mass flow rate must be kept and the liner will be more protected in these regions. The solution-dependent distribution of coolant on both the tangential and axial directions are hardly predictable *a priori* and its effect on the heat load deserves further investigations in the future.

Take-Off

Increasing the power load by means FAR, $P30$ and $T30$ leads to higher burning rates, gas temperatures and ultimately more critical conditions for the liners. The hot core region moves up to the outlet, as noticeable in Fig. 4.31. As at Approach, the flame propagates within the injector and

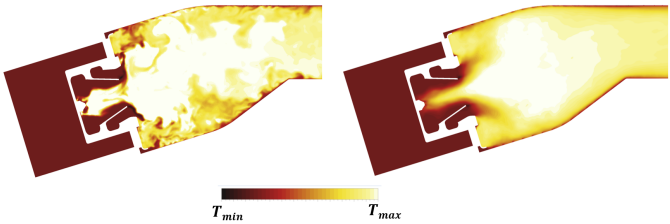

Figure 4.31: Contours of instantaneous (left) and mean (right) gas temperature at Take-Off condition.

can reach the proximity of the pilot atomizer. This phenomenon is visible in both the instantaneous and mean gas temperature, even if monitoring different time-steps have highlighted an alternating positioning of the flame in and out of the swirler. However, the mean opening angle of the swirling jet becomes more closed than at Approach because of the augmented flow rate.
The severe environment within the flametube causes a significant increase in the thermal stresses on the liner compared against the Approach condition, as illustrated by the metal temperature distribution reported in Fig. 4.32. The wall temperature predicted by U-THERM3D is considerably higher than the values provided by the corresponding THERM3D simulation. Unlike the previous operating condition, a general increase of temperature is observed in almost all the surface with peak values of around 20% in a relative term, mainly located in the upstream region

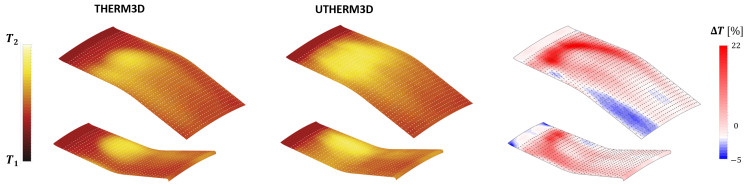

Figure 4.32: Contours of mean temperature on the hot side of the liners for the THERM3D (left) and U-THERM3D (middle) simulations at Take-Off condition. The relative difference between the latter and the former normalized by the THERM3D value (in [K]) is also reported (right).

where the swirling flow interacts with the wall. In particular, as for Approach, the following considerations are still valid:

- The resolution of a portion of the turbulent convection spectrum smooths the temperature gradients;
- The resolved mixing increases the entrainment of hot gases in the outer recirculation zones resulting in an increase of metal temperature in the liner region closer to the slot exit;
- The swirling flow interacts with the slot and film cooling more uniformly in the spanwise direction, almost making the cold streaks of THERM3D disappear.

With a focus on the Outer Liner, the downstream half shows an opposite trend of the relative difference of temperature between an unsteady and steady simulation. Indeed, at the Approach condition, this region is warmed by gases having exchanged more heat with the primary zone of the liner and which, for this reason, are cooler. As the heat transfer in the primary zone is augmented in an unsteady way, the final region can be wet by colder gases resulting in a slightly lower metal temperature. On the other hand, at Take-Off hot radiating pockets are convected downstream to the mid-region of the liner, contributing to keep higher metal temperatures in the second half of the liner.
Similarly to Fig. 4.28, Fig. 4.33 shows again as using U-THERM3D the temperature rise is anticipated along the centerline axial direction, confirming the great impact on metal temperature of a scale-resolving prediction of the aerothermal field in the outer recirculation zone. The maximum value identifies jet-wall interaction phenomena, approximately

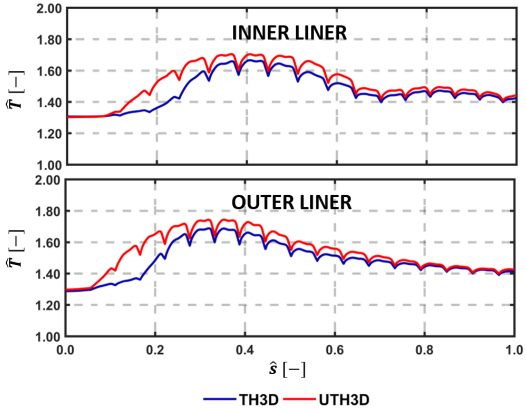

Figure 4.33: Comparison of the centerline temperature between experiments, THERM3D and U-THERM3D on the cold sides of the Inner Liner (top) and Outer Liner (bottom) at Take-Off condition.

located at 40% of the relative curvilinear abscissa for both the liners and the operating conditions. However, on the inner side, a second small peak region appears at 80% of the liner length that is also visible in the THERM3D simulation. This feature is caused by radiation, in terms of a greater weight of the shape factor on the thermal load for this operating point. The view factor from the flame and the dome to the second half of the Inner Liner is unfavourable because of the adopted combustor geometry, leading to a local peak in the radiative heat flux.

Heat load analysis

A deep insight into the contribution of the different heat transfer modes to the thermal load can be useful to understand the metal temperature trends. For this purpose Fig. 4.34 and Fig. 4.35 show the energy budget for Inner Liner and Outer Liner, respectively. The total heat load normalized by a reference value and divided into the convection (blue) and radiation (red) contributions is reported for the hot side (HS), cold side (CS) and effusion holes (EFF). The values are compared against the results obtained with THERM3D for both the operating conditions. The numbers above each bar highlight quantitatively the relative component of convection and radiation on the heating (HS) and cooling (CS+EFF) of the liner. The heat load follows the temperature trend, with a significant increase

moving from Approach to Take-Off independently by the coupling strategy. However, modelling conjugate heat transfer in an unsteady fashion in

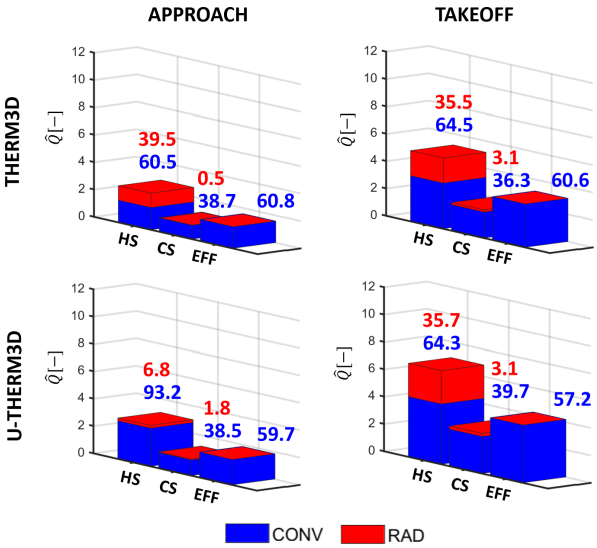

Figure 4.34: Comparison between THERM3D and U-THERM3D of the normalized total heat loads for the Inner Liner at Approach and Take-Off conditions. Values above the bars are the relative contribution of convection and radiation to the heating and cooling of the liner.

place of a steady framework modifies the relative weight of the heat transfer modes. At Approach, in the U-THERM3D simulation radiation is reduced by the lower gas temperature. Moreover, the augmented convection caused by the prediction of higher heat transfer coefficients as well as a lower film protection increases the metal temperature making the contribution of radiation almost null. At Take-Off, instead, because of the widespread hot gas region provided by the SAS computation, the radiative heat load growths compared to both the Approach and the THERM3D results.

The heat load is more than doubled moving from Approach to Take-Off, closer to three times on the Outer Liner. The unbalanced distribution of radiative heat load between Inner and Outer liners can be attributed to the annular geometry of the combustor, which makes high view factors

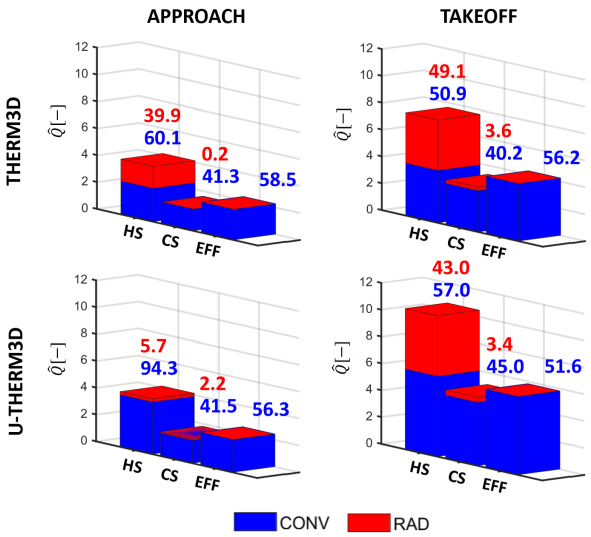

Figure 4.35: Comparison between THERM3D and U-THERM3D of the normalized total heat loads for the Outer Liner at Approach and Take-Off conditions. Values above the bars are the relative contribution of convection and radiation to the heating and cooling of the liner.

from the Inner Liner and the flame to the Outer Liner. On the other hand, the Outer Liner views the Inner Liner with a lower factor. As a result, the latter radiates completely to the former which, however, radiates partially itself. Inhomogeneities in the wall to wall radiation become more relevant when metal temperature is higher, as at Take-Off. This result is also confirmed by the relative contribution of convection and radiation that is around 65%/35% for the Inner Liner and 55%/45% for the Outer Liner. As evident in Fig. 4.34 and Fig. 4.35 the cooling function is largely demanded to the effusion system, whose weight on liner cooling is 56% on average. The absolute value is almost unchanged at Approach using the present unsteady coupling procedure but the increase is evident at Take-Off as a result of the higher metal temperature predicted by U-THERM3D.

4.3.4 Effusion cooling

Effusion film cooling has a key role in the prevention of liner from undesired peak temperatures. The heat sink effect and a good film protection have lead this technique to head between the cooling strategies for combustors. From a design perspective, coolant distribution on the multiperforated liner should be accurately predicted because it affects the heat load and therefore the solid temperature. The thousands of tiny holes require increasingly computational efforts to have a direct solution of the internal flow field that is often not justified by a corresponding improvement of accuracy. Indeed, the small size of these features and the manufacturing techniques create uncertainties on the real hole geometry, concerning parameters as the angle, diameter and roughness, for instance. Unavoidably, losses and heat transfer are affected and their numerical modelling with wall functions or wall-resolved approaches are not always capable to fit measurements. Low-order methods for effusion cooling modelling, as exploited in the present work, are an effective alternative to save computational resources and account for non-ideal geometries in a global fashion. In the previous results effusion was modelled grouping the holes of each row in a single patch, where uniform boundary conditions are applied. As already mentioned, flow rate in a row is derived from preliminary RANS simulations and considerations on the averaged pressure drop. The interaction between swirling flow and wall can cause local inhomogeneities in spanwise direction, leading to potential disagreement in the distribution of coolant on the liner. Adiabatic simulations with three different methods for the solution of effusion holes were performed. In addition to the row-grouped approach (Case 1), Fig. 4.36 shows the

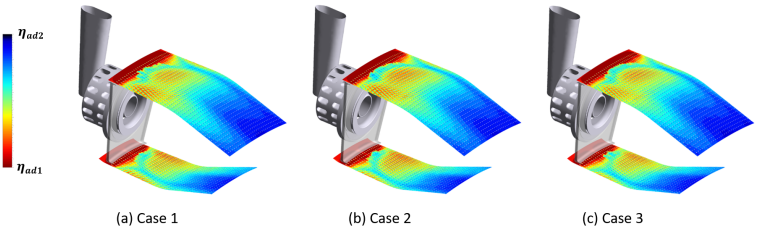

Figure 4.36: Adiabatic effectiveness of efussion cooling for different treatments of multiperforation boundary conditions.

results of adiabatic effectiveness for the two other hole-by-hole methods:

local pressure-drop scaling of a predefined total flow rate (Case 2) and solution-dependent flow rate (Case 3). It is worth mentioning that in Fig. 4.36 only the coolant injected from the effusion holes was considered for adiabatic effectiveness η_{ad} to better highlight the differences of the methods. A more remarkable comparison is reported in Fig. 4.37 for the difference of η_{ad} between Case 2 and Case 1. A negative value (blue

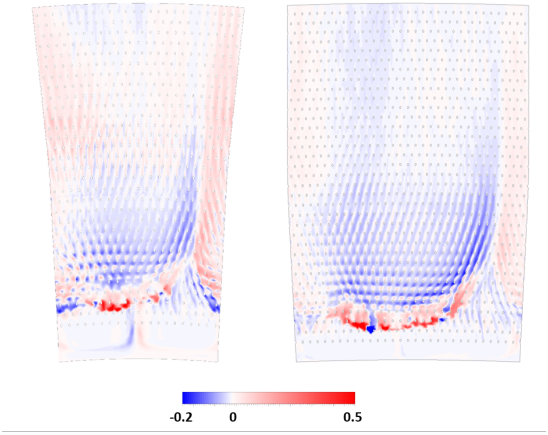

Figure 4.37: Difference of coolant concentration between Case 2 and Case 1.

to white range) means a coolant concentration in Case 1 higher than in Case 2. On the contrary, a positive value (red to white range) means an adiabatic effectiveness in Case 1 lower than in Case 2. The results show that the region where the swirling flow interacts with the liner benefits of a local pressure drop scaling model. Indeed, the stagnant pressure rises in this zone because of the impinging effect of the swirling jet and, as a result, the pressure drop in the hole as well as its flow rate decrease. Keeping the same total coolant flow rate, mid-cup regions get a better protection from hot gases. Making the comparison of the hole-by-hole methods in terms of difference between adiabatic effectiveness of Case 3 and Case 2, a solution-dependent model using a discharge coefficient $C_d = 0.7$ provides an higher coolant mass flow and then η_{ad} on all the multiperforated surface. In light of these results, as the previous CHT simulations were performed with a row-grouped approach, the metal temperature predicted

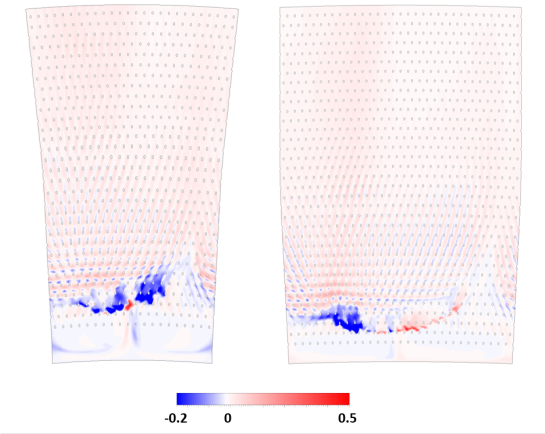

Figure 4.38: Difference of coolant concentration between Case 3 and Case 2.

by THERM3D/U-THERM3D may have been negatively affected by this unrealistic distribution of coolant among all the holes. In particular, the liner will be colder on the mid-cup region and warmer on the cup region, according to Fig. 4.37 and 4.38.

4.4 Concluding remarks

In this chapter the main findings of a numerical campaign aimed at supporting and providing a better understanding during the design phase of an aeronautical effusion-cooled lean burn combustor are illustrated. A proven numerical setup developed for turbulent spray flames was exploited to simulate a typical flight mission. First, a series of multiphysics simulations was performed in RANS context with the THERM3D procedure. A comparison of metal temperature results against experimental data has shown the need of an appropriate prediction of the interaction between swirling flow and liners to correctly catch the temperature distribution at the walls. An accurate prediction of the aerothermal field has been observed in the flametube adiabatic simulations using Scale-Resolving Simulations. Indeed, a detailed analysis of the exit temperature profile and the emissions has revealed a good agreement with the measurements in all the operating conditions. A detailed investigation on the adiabatic

wall temperature has shown that Scale-Resolving Simulations can fill the gap of THERM3D in the prediction of metal temperature. Such an approach, in fact, can properly characterize all the aspects of swirled spray flames, from the stabilization mechanism of the flame to the swirling flow-liner interaction that affects the convective heat load, but can also take into account to the fourth-power dependency on gas temperature of radiative fluxes. The final goal of this chapter, that was the application of the multiphysics tool U-THERM3D (i.e. the object of the thesis) on a simplified arrangement of the combustor, is capable to exploit Scale-Resolving Simulations in the context of CHT analysis. Simulations on Approach and Take-Off conditions were run for roughly 45000 CPU hours, a computational time one order of magnitude greater than the one required by the equivalent steady simulations. Despite the computational cost, the new tool provides a general increase of metal temperature and a smoother distribution that improve the prediction of liner temperature, as confirmed by a comparison with the experimental data. While convection increases, a heat load analysis reveals opposite trends for radiation in the two operating conditions moving from a steady to an unsteady coupling. At Approach, maximum gas temperature does not change compared to THERM3D simulation and, together with the higher wall temperature, eliminate the contribution of radiation. On the other hand at Take-Off the heat transferred by radiation rises because of the widespread hot gases volume within the flametube. Nevertheless, as in the THERM3D solution, the ratio between convection and radiation is around $65:35$ and $55:45$ for the inner and outer liners, respectively. Here, the major weight of radiation in the Outer Liner can be explained by the annular geometry of the combustor that provides self-viewing properties to the outer concave surface.

Conclusion

Designing a modern combustor is a time- and money-consuming task that can benefit from the use of CFD to minimize the recourse to experimental tests, especially nowadays that the increasingly widespread exploitation of massively parallel computing is making affordable numerical investigations from a scale-resolving perspective. Phenomena as combustion, convection, radiation and conduction involved in gas turbine burners are characterized by complex multiphysics/multiscale interactions that must be properly modelled. Among all design requirements, the liner temperature is one of the most dependent on the aerothermal field but its high-fidelity prediction cannot disregard the need of Scale-Resolving Simulations. The unsteady feature of these calculations have to face with the large differences in time scales of fluid and solid, so that in the present manuscript a desynchronised loose coupling methodology, called U-THERM3D, was developed in ANSYS Fluent and proposed as tool to simulate the whole multiphysics problem. Such a modelling is challenging because requires to properly choose the coupling parameters and the load balancing, which can affect the stability and efficiency of the coupled simulation, respectively. The procedure was successfully validated in the context of URANS simulations on predictable and simple solutions, as a flat plate or a backward-facing step, subject to pulsating inlet conditions. A more relevant assessment was carried out on a model aero-engine combustor tested at DLR and featuring a swirled sooting flame, for which several measurements are available from gas temperature and species to the quartz window temperature. As the coupling had to handle the wide range of scales associated to the turbulence spectrum, the DLR burner was the ideal apparatus to test the procedure in conditions closer to real industrial applications. In a previous work RANS multiphysics simulations revealed the strong interaction between soot production, radiation, aerothermal field and wall temperature for the aforementioned test case. For this reason, such an investigation has benefited of a U-THERM3D

simulation combining reacting LES, radiation and conduction. Despite the increased computational cost, the scale-resolving approach predicts a representative flame structure and aerothermal field as well as an intense interaction between swirling flow and window that drastically improves the wall temperature profile. Indeed, higher quartz temperatures were observed in the primary zone where the coupled problem is strongly affected by flow turbulence.
The promising results on the DLR burner paved the way for high-fidelity design simulations on a full-annular rig representing a lean-burn aeroengine combustor tested at CIAM during a EU project. Experimental campaign provided measurements of exit temperature profile, emissions and liner temperatures in several operating conditions. In this work numerical analysis were carried out at increasingly challenging levels. Preliminary steady Conjugate Heat Transfer simulations exploiting the THERM3D tool shown common 3D feature in the metal temperature distribution of the different test points. Indeed, this is again affected by the swirling flow-liner interaction that, in turn, is detrimental for the film cooling coverage. The results of exit profile temperature and emission were largely improved by the adoption of Scale Adaptive Simulation for flametube adiabatic investigations. Simulating the tested operating conditions and extending the prediction to Take-Off, it was clearly highlighted the impact of inlet pressure and temperature, as well as P/T and FAR, on the aerothermal field and in particular, on the flame regime and the process of flame stabilization. From the same simulations, the gas and wall adiabatic temperature suggested a different prediction of heat load using scale-resolving approaches because of the non-linear radiative fluxes and the swirling flow disturbances on the coolant protection. As a result, high-fidelity CHT analysis were conducted using the U-THERM3D procedure for two test points, that are Approach and Take-Off. Moving from the former to the latter a general increase of the heat loads is observed, mainly driven by the increase of T30 and, in the second measure by the FAR. Compared to the THERM3D results, a common feature in the two test points is the increase of temperature in the first half of the liner related to the resolution in SAS framework of the turbulent interaction between the swirling flow and the walls. Indeed, the Scale-Resolving Simulation is able to predict the hot gases entrainment in the outer recirculation zones, the local growth of heat transfer coefficient and the unsteady sweeping of film cooling. While convection increases, a heat load analysis reveals opposite trends for radiation in the two operating conditions moving from a steady to an unsteady coupling.
Hence, the present work highlights that a proper modelling of the aerother-

mal field with Scale-Resolving Simulations can be effective in the prediction of liner temperature and can reveal unexpected changes in the relative contribution of heat transfer modes compared to a steady modelling. The acceptable prediction of metal temperature obtained by U-THERM3D shows the potential of this tool as a framework for the high-fidelity thermal design of gas turbine combustors. Obviously, the accuracy of the coupled simulation can benefit from the improvement in the different involved models and to the author's opinion research effort should be focused on this task, that ranges from combustion to effusion cooling modelling.

Bibliography

[1] ICAO. Aviation benefits.

[2] International Air Transport Association. Economic performance of the airline industry.

[3] Pedro Argüelles, Manfred Bischoff, Philippe Busquin, BAC Droste, Sir Richard Evans, W Kröll, JL Lagardere, A Lina, J Lumsden, D Ranque, et al. European aeronautics: a vision for 2020. *Advisory Council for Aeronautics Research in Europe, Report*, 2001.

[4] ICAO. Environmental report. *Aviation and climate change*, 2016.

[5] ACARE. Strategic research and innovation agenda - volume 1.

[6] Clean Sky 2 Joint Undertaking, Work Plan 2014-2015 Version 2, 2014.

[7] General Electric. Taps ii combustor - final report of continuous lower energy, emissions and noise (cleen) program.

[8] JJ McGuirk. The aerodynamic challenges of aeroengine gas-turbine combustion systems. *The Aeronautical Journal*, 118(1204):557–599, 2014.

[9] V Moreno. Combustor liner durability analysis. 1981.

[10] Aspi R. Wadia. Advanced Combustor Liner Cooling Technology for Gas Turbines. *Defence Science Journal*, 38(4):363–380, January 2014.

[11] K. M. Bernhard Gustafsson and T. Gunnar Johansson. An Experimental Study of Surface Temperature Distribution on Effusion-Cooled Plates. *Journal of Engineering for Gas Turbines and Power*, 123(2):308–316, January 2001.

[12] G. E. Andrews, A. A. Asere, M. L. Gupta, and M. C. Mkpadi. Full Coverage Discrete Hole Film Cooling: The Influence of Hole Size. page V003T09A003, March 1985.

[13] Full coverage film cooling investigations adiabatic wall - Technische Informationsbibliothek (TIB).

[14] Juan Luis Florenciano and Pascal Bruel. LES fluid–solid coupled calculations for the assessment of heat transfer coefficient correlations over multi-perforated walls. *Aerospace Science and Technology*, 53:61–73, June 2016.

[15] B. Wurm, A. Schulz, H.-J. Bauer, and M. Gerendas. Impact of Swirl Flow on the Cooling Performance of an Effusion Cooled Combustor Liner. *ASME J Gas Turb Pwr*, (134):121503–1:121503–9, 2012.

[16] B. Wurm, A. Schulz, H.-J. Bauer, and M. Gerendas. Cooling efficiency for assessing the cooling performance of an effusion cooled combustor liner. *Proceedings of ASME Turbo Expo*, (GT2013-94304), 2013.

[17] B. Wurm, A. Schulz, H.-J. Bauer, and M. Gerendas. Impact of swirl flow on the penetration behaviour and cooling performance of a starter cooling film in modern lean operating combustion chambers. *Proceedings of ASME Turbo Expo*, (GT2014-25520), 2014.

[18] A. Andreini, G. Caciolli, B. Facchini, A. Picchi, and F. Turrini. Experimental investigation of the flow field and the heat transfer on a scaled cooled combustor liner with realistic swirling flow generated by a lean-burn injection system. *ASME J Turbomach*, 137(3)(031012), 2014.

[19] A Andreini, G Caciolli, B Facchini, A Picchi, and F Turrini. Experimental investigation of the flow field and the heat transfer on a scaled cooled combustor liner with realistic swirling flow generated by a lean-burn injection system. *ASME J Turbomac*, 137(3):031012, 2015.

[20] A Andreini, R Becchi, B Facchini, L Mazzei, A Picchi, and F Turrini. Adiabatic effectiveness and flow field measurements in a realistic effusion cooled lean burn combustor. *ASME J Eng Gas Turb Pwr*, 138(3):031506, 2016.

[21] A Andreini, B Facchini, R Becchi, A Picchi, and F Turrini. Effect of slot injection and effusion array on the liner heat transfer coefficient of a scaled lean-burn combustor with representative swirling flow. *ASME J Eng Gas Turb Pwr*, 138(4):041501, 2016.

[22] Antonio Andreini, Riccardo Becchi, Bruno Facchini, Alessio Picchi, and Antonio Peschiulli. The effect of effusion holes inclination angle on the adiabatic film cooling effectiveness in a three-sector gas turbine combustor rig with a realistic swirling flow. *International Journal of Thermal Sciences*, 121:75–88, 2017.

[23] A Andreini, A Ceccherini, B Facchini, F Turrini, and I Vitale. Assessment of a set of numerical tools for the design of aero-engines combustors: study of a tubular test rig. *ASME Paper No. GT2009-59539*, 2009.

[24] Sebastian Tietz and Thomas Behrendt. Development and application of a pre-design tool for aero-engine combustors. *CEAS Aeronautical Journal*, 2(1-4):111–123, 2011.

[25] Arthur H Lefebvre. *Gas turbine combustion*. CRC press, 1998.

[26] A Andreini, D Bertini, B Facchini, and S Puggelli. Large-eddy simulation of a turbulent spray flame using the flamelet generated manifold approach. *Energy Procedia*, 82:395–401, 2015.

[27] Stefano Puggelli, Davide Bertini, Lorenzo Mazzei, and Antonio Andreini. Assessment of scale-resolved computational fluid dynamics methods for the investigation of lean burn spray flames. *Journal of Engineering for Gas Turbines and Power*, 139(2):021501, 2017.

[28] S Puggelli, D Bertini, L Mazzei, and A Andreini. Modelling strategies for large-eddy simulation of lean burn spray flames. *Proceedings of ASME Turbo Expo*, (GT2017-64569), 2017.

[29] E Mercier, L Tesse, and N Savary. 3d full predictive thermal chain for gas turbine combustor metal temperature. In *Proceedings of the 25th International Congress of the Aeronautical Sciences (ICAS 2006), Hamburg, Germany*, 2006.

[30] Sandrine Berger, Stéphane Richard, Gabriel Staffelbach, Florent Duchaine, and Laurent Gicquel. Aerothermal prediction of an aeronautical combustion chamber based on the coupling of large eddy simulation, solid conduction and radiation solvers. In *ASME Turbo*

Expo 2015: Turbine Technical Conference and Exposition, pages V05AT10A007–V05AT10A007. American Society of Mechanical Engineers, 2015.

[31] S. Jaure, F. Duchaine, G. Staffelbach, and L. Y. M. Gicquel. Massively parallel conjugate heat transfer methods relying on large eddy simulation applied to an aeronautical combustor. *Computational Science & Discovery*, 6(1):015008, 2013.

[32] Chai Koren, Ronan Vicquelin, and Olivier Gicquel. Self-adaptive coupling frequency for unsteady coupled conjugate heat transfer simulations. *International Journal of Thermal Sciences*, 118:340–354, August 2017.

[33] S. Mendez and F. Nicoud. An adiabatic homogeneous model for the flow around a multi-perforated plate. *AIAA Journal*, 10(46):2623–2633, 2008.

[34] A. Andreini, R. Da Soghe, B. Facchini, L. Mazzei, S. Colantuoni, and F. Turrini. Local Source Based CFD Modeling of Effusion Cooling Holes: Validation and Application to an Actual Combustor Test Case. *ASME J Gas Turb Pwr*, 136(011506), January 2014.

[35] L Mazzei, A Andreini, B Facchini, and L Bellocci. A 3d coupled approach for the thermal design of aero-engine combustor liners. *Proceedings of ASME Turbo Expo*, (GT2016-56605), 2016.

[36] Roger C Reed. *The superalloys: fundamentals and applications*. Cambridge university press, 2008.

[37] A Andreini, C Carcasci, A Ceccherini, B Facchini, M Surace, D Coutandin, S Gori, and A Peschiulli. Combustor liner temperature prediction: a preliminary tool development and its application on effusion cooling systems. In *First CEAS European Air and Space Conference Century Perspectives, Berlin, September*, pages 10–13, 2007.

[38] Warren M Rohsenow, James P Hartnett, Young I Cho, et al. *Handbook of heat transfer*, volume 3. McGraw-Hill New York, 1998.

[39] Garry L Brown and Anatol Roshko. On density effects and large structure in turbulent mixing layers. *Journal of Fluid Mechanics*, 64(04):775–816, 1974.

[40] Stephen B Pope. *Turbulent flows*. Cambridge university press, 2000.

[41] Thierry Poinsot and Denis Veynante. *Theoretical and numerical combustion*. RT Edwards Inc., 2005.

[42] RG Abdel-Gayed, D Bradley, MN Hamid, and M Lawes. Lewis number effects on turbulent burning velocity. In *Symposium (International) on Combustion*, volume 20, pages 505–512. Elsevier, 1985.

[43] Ömer L Gülder. Turbulent premixed flame propagation models for different combustion regimes. In *Symposium (International) on Combustion*, volume 23, pages 743–750. Elsevier, 1991.

[44] R Borghi and M Destriau. Combustion and flame: chemical and physical principles. *Editions Technip*, 1998.

[45] Antonio Andreini. *Sviluppo di modelli numerici per l'analisi della combustion turbolenta premiscelata nelle turbine a gas*. PhD thesis, 2004.

[46] JP Holman et al. Heat transfer. 10th, 2010.

[47] WJS Ramaekers, BA Albrecht, JA van Oijen, LPH de Goey, and RGLM Eggels. The application of flamelet generated manifolds in modelling of turbulent partially-premixed flames. *RGLM Eggels*, 2005.

[48] Kushal S Kedia and Ahmed F Ghoniem. The anchoring mechanism of a bluff-body stabilized laminar premixed flame. *Combustion and flame*, 161(9):2327–2339, 2014.

[49] Dan Michaels and Ahmed F Ghoniem. Impact of the bluff-body material on the flame leading edge structure and flame–flow interaction of premixed ch4/air flames. *Combustion and Flame*, 172:62–78, 2016.

[50] Carmen Jiménez, Dan Michaels, and Ahmed F Ghoniem. Ultra-lean hydrogen-enriched oscillating flames behind a heat conducting bluff-body: Anomalous and normal blow–off. *Proceedings of the Combustion Institute*, 2018.

[51] R Mercier, TF Guiberti, A Chatelier, D Durox, O Gicquel, N Darabiha, T Schuller, and B Fiorina. Experimental and numerical investigation of the influence of thermal boundary conditions on premixed swirling flame stabilization. *Combustion and Flame*, 171:42–58, 2016.

[52] Thibault F Guiberti, Daniel Durox, Philippe Scouflaire, and Thierry Schuller. Impact of heat loss and hydrogen enrichment on the shape of confined swirling flames. *Proceedings of the Combustion Institute*, 35(2):1385–1392, 2015.

[53] Christian Kraus, Laurent Selle, and Thierry Poinsot. Coupling heat transfer and large eddy simulation for combustion instability prediction in a swirl burner. *Combustion and Flame*, 191:239–251, 2018.

[54] P Schmitt, B Schuermans, K Geigle, and T Poinsot. Effects of radiation, wall heat loss and effusion cooling on flame stabilisation and pollutant prediction in les of gas turbine combustion. In *ECCOMAS thematic conference on computational combustion*, 2005.

[55] Chai Koren, Ronan Vicquelin, and Olivier Gicquel. Multiphysics simulation combining large-eddy simulation, wall heat conduction and radiative energy transfer to predict wall temperature induced by a confined premixed swirling flame. *Flow, Turbulence and Combustion*, 101(1):77–102, 2018.

[56] MB Giles. Stability analysis of numerical interface conditions in fluid–structure thermal analysis. *International Journal for Numerical Methods in Fluids*, 25(4):421–436, 1997.

[57] G Gimenez, M Errera, D Baillis, Y Smith, and F Pardo. A coupling numerical methodology for weakly transient conjugate heat transfer problems. *International Journal of Heat and Mass Transfer*, 97:975–989, 2016.

[58] Tom Verstraete. *Multidisciplinary turbomachinery component optimization considering performance, stress, and internal heat transfer*. PhD thesis, Karman Institute, 2008.

[59] Florent Duchaine, Alban Corpron, Lorenzo Pons, Vincent Moureau, Franck Nicoud, and Thierry Poinsot. Development and assessment of a coupled strategy for conjugate heat transfer with large eddy simulation: application to a cooled turbine blade. *International Journal of Heat and Fluid Flow*, 30(6):1129–1141, 2009.

[60] Laurent YM Gicquel, N Gourdain, J-F Boussuge, H Deniau, G Staffelbach, P Wolf, and Thierry Poinsot. High performance parallel computing of flows in complex geometries. *Comptes Rendus Mecanique*, 339(2-3):104–124, 2011.

[61] Samuel Buis, Andrea Piacentini, and Damien Déclat. Palm: a computational framework for assembling high-performance computing applications. *Concurrency and Computation: Practice and experience*, 18(2):231–245, 2006.

[62] Sandrine Berger, Stéphane Richard, Gabriel Staffelbach, Florent Duchaine, and Laurent Gicquel. Aerothermal Prediction of an Aeronautical Combustion Chamber Based on the Coupling of Large Eddy Simulation, Solid Conduction and Radiation Solvers. page V05AT10A007, June 2015.

[63] L He and MLG Oldfield. Unsteady conjugate heat transfer modeling. *Journal of turbomachinery*, 133(3):031022, 2011.

[64] M Fadl, L He, P Stein, and G Marinescu. Assessment of unsteadiness modeling for transient natural convection. *Journal of Engineering for Gas Turbines and Power*, 140(1):012605, 2018.

[65] M Fadl and L He. On les based conjugate heat transfer procedure for transient natural convection. In *ASME Turbo Expo 2017: Turbomachinery Technical Conference and Exposition*, pages V05AT10A002–V05AT10A002. American Society of Mechanical Engineers, 2017.

[66] S. Mendez and F. Nicoud. An adiabatic homogeneous model for the flow around a multi-perforated plate. *AIAA Journal*, 10(46):2623–2633, 2008.

[67] Romain Bizzari, Dorian Lahbib, Antoine Dauptain, Florent Duchaine, Stephane Richard, and Franck Nicoud. Low order modeling method for assessing the temperature of multi-perforated plates. *International Journal of Heat and Mass Transfer*, 127:727–742, 2018.

[68] G. Cottin, E. Laroche, N. Savary, and P. Millan. Modeling of the Heat Flux for Multi-Hole Cooling Applications. *Proceedings of ASME Turbo Expo*, (GT2011-46330), 2011.

[69] R Bizzari, D Lahbib, A Dauptain, F Duchaine, LYM Gicquel, and F Nicoud. A thickened-hole model for large eddy simulations over multiperforated liners. *Flow, Turbulence and Combustion*, pages 1–13, 2018.

[70] Martin Thomas, Antoine Dauptain, Florent Duchaine, Laurent Gicquel, Charlie Koupper, and Franck Nicoud. Comparison of heterogeneous and homogeneous coolant injection models for large

eddy simulation of multiperforated liners present in a combustion simulator. In *ASME Turbo Expo 2017: Turbomachinery Technical Conference and Exposition*, pages V02BT41A038–V02BT41A038. American Society of Mechanical Engineers, 2017.

[71] Guillaume Vignat, Guillaume Taliercio, Jean Lamouroux, Sébastien Da Veiga, Nicolas Savary, and Patrick Duchaine. Analysis of performance sensitivity to geometrical variations of a modern helicopter engine combustor using les simulations. In *ASME Turbo Expo 2017: Turbomachinery Technical Conference and Exposition*, pages V04BT04A003–V04BT04A003. American Society of Mechanical Engineers, 2017.

[72] Samir Rida, Robert Reynolds, Saugata Chakravorty, and Kapil Gupta. Imprinted effusion modeling and dynamic cd calculation in gas turbine combustors. In *ASME Turbo Expo 2012: Turbine Technical Conference and Exposition*, pages 589–599. American Society of Mechanical Engineers, 2012.

[73] T Aumeier and Thomas Behrendt. Application of an aerothermal model for effusion cooling systems and finite rate chemistry in aero-engine combustors. In *ICHMT DIGITAL LIBRARY ONLINE*. Begel House Inc., 2015.

[74] S. Voigt, B. Noll, and M. Aigner. Development of a Macrospcopic CFD Model for Effsion Cooling Applciations. In *Proceedings of ASME Turbo Expo*, 2012.

[75] A. Andreini, R. Da Soghe, B. Facchini, L. Mazzei, S. Colantuoni, and F. Turrini. Local source based CFD modeling of effusion cooling holes: Validation and application to an actual combustor test case. *ASME J Gas Turb Pwr*, 136(1):011506, 2014.

[76] L. Andrei, A. Andreini, B. Facchini, L. Winchler, and L. Innocenti. Film cooling modelling for gas turbine nozzles and blades: Validation and application. *Proceedings of ASME Turbo Expo*, (GT2015-43345), 2015.

[77] Alejandro M Briones, Brent A Rankin, Scott D Stouffer, Timothy J Erdmann, and David L Burrus. Parallelized, automated, and predictive imprint cooling model for combustion systems. *Journal of Engineering for Gas Turbines and Power*, 139(3):031505, 2017.

[78] S. Puggelli. Towards a unified approach for large eddy simulation of turbulent spray flames. *PhD Thesis - Università degli Studi di Firenze*, 2017.

[79] L. Mazzei. A 3d coupled approach for the thermal design of aero-engine combustor liners. *PhD Thesis - Università degli Studi di Firenze*, 2014.

[80] Phu Hung Nguyen and Eva Dorignac. Experimental study of convective exchange in a low aspect ratio perforation: Application to cooling of multiperforated wall. *Experimental Thermal and Fluid Science*, 33(1):114–122, 2008.

[81] G. Boudier, L. Y. M. Gicquel, and T. J. Poinsot. Effects of mesh resolution on large eddy simulation of reacting flows in complex geometry combustors. *Elsevier Combustion and Flame*, 155:196–214, October 2008.

[82] W.P. Jones, S. Lyra, and S. Navarro-Martinez. Numerical investigation of swirling kerosene spray flames using large eddy simulation. *Combustion and Flame*, 159(4):1539 – 1561, 2012.

[83] W. P. Jones, A. J. Marquis, and K. Vogiatzaki. Large-eddy simulation of spray combustion in a gas turbine combustor. *Combustion and Flame*, 161(1):222–239, January 2014.

[84] A. Giusti and E. Mastorakos. Detailed chemistry LES/CMC simulation of a swirling ethanol spray flame approaching blow-off. *Proceedings of the Combustion Institute*, 36(2):2625 – 2632, 2017.

[85] Simone Hochgreb. Mind the gap: Turbulent combustion model validation and future needs. *Proceedings of the Combustion Institute*, 2018.

[86] S Puggelli, D Bertini, L Mazzei, and A Andreini. Scale adaptive simulations of a swirl stabilized spray flame using flamelet generated manifold. *Energy Procedia*, 101:1143–1150, 2016.

[87] S Puggelli, D Bertini, L Mazzei, and A Andreini. Modeling strategies for large eddy simulation of lean burn spray flames. *ASME J Gas Turb Pwr*, 140(5):051501, 2018.

[88] S. Puggelli, S. Paccati, D. Bertini, L. Mazzei, A. Andreini, and Giusti A. Multi-coupled numerical simulations of the dlr generic

single sector combustor. *Combustion Science and Technology*, 2018. Transaction of the MCS-10: Tenth Mediterranean Combustion Symposium. In press.

[89] D Pampaloni, D Bertini, S Puggelli, L Mazzei, and A Andreini. Methane swirl-stabilized lean burn flames: assessment of scale-resolving simulations. *Energy Procedia*, 126:834–841, 2017.

[90] Jeroen van Oijen. *Flamelet-generated manifolds: development and application to premixed laminar flames*. Technische Universiteit Eindhoven, 2002.

[91] A. Donini, R. J. M. Bastiaans, J. A. Van Oijen, and L. P. H. de Goey. The Implementation of Five-Dimensional FGM Combustion Model for the Simulation of a Gas Turbine Model Combustor. *ASME J Gas Turb Pwr*, June 2015.

[92] ANSYS. *ANSYS Fluent, 17.1 Theory Guide*.

[93] SAj Morsi and AJ Alexander. An investigation of particle trajectories in two-phase flow systems. *Journal of Fluid Mechanics*, 55(2):193–208, 1972.

[94] Daniel D Joseph, J Belanger, and GS Beavers. Breakup of a liquid drop suddenly exposed to a high-speed airstream. *International Journal of Multiphase Flow*, 25(6):1263–1303, 1999.

[95] B Abramzon and WA Sirignano. Droplet vaporization model for spray combustion calculations. *International journal of heat and mass transfer*, 32(9):1605–1618, 1989.

[96] W. E. Ranz and Jr. W. R. Marshall. Vaporation from drops, part i. *Chem. Eng. Prog.*, 48(3), 1952.

[97] Y. Egorov and F. R. Menter. Development and application of SST-SAS turbulence model in the DESIDER Project. *Second Symposium on Hybrid RANS-LES Methods*, 2007.

[98] JY Murthy and SR Mathur. Finite volume method for radiative heat transfer using unstructured meshes. *Journal of thermophysics and heat transfer*, 12(3):313–321, 1998.

[99] L Mazzei, S Puggelli, D Bertini, D Pampaloni, and A Andreini. Modelling soot production and thermal radiation for turbulent diffusion flames. *Energy Procedia*, 126(Supplement C):826 – 833,

2017. ATI 2017 - 72nd Conference of the Italian Thermal Machines Engineering Association.

[100] S. Freitag, U. Meier, J. Heinze, T. Behrendt, and C. Hassa. Measurement of initial conditions of a kerosene spray from a generic aeroengine injector at elevated pressure. In *ILASS - Europe 2010, 23rd Annual Conference on Liquid Atomization and Spray Systems*.

[101] U. Meier, J. Heinze, S. Freitag, and C. Hassa. Spray and flame structure of a generic injector at aeroengine conditions. *ASME J Gas Turb Pwr*, 134(031503), March 2012.

[102] S. Gepperth, E. Barow, R. Koch, and H.J. Bauer. Primary atomization of prefilming airblast nozzles: Experimental studies using advanced image processing techniques. In *26th Annual Conference on Liquid Atomization and Spray Systems (ILASS Europe), Bremen, Germany, Sept*, pages 8–10, 2014.

[103] I. M. Kennedy. Models of soot formation and oxidation. *Progress in Energy and Combustion Science*, 23(2):95–132, 1997.

[104] ME Mueller, G Blanquart, and H Pitsch. Hybrid method of moments for modeling soot formation and growth. *Combustion and Flame*, 156(6):1143–1155, 2009.

[105] Karl Netzell, Harry Lehtiniemi, and Fabian Mauss. Calculating the soot particle size distribution function in turbulent diffusion flames using a sectional method. *Proceedings of the Combustion Institute*, 31(1):667–674, 2007.

[106] Pablo Mitchell and Michael Frenklach. Monte carlo simulation of soot aggregation with simultaneous surface growth-why primary particles appear spherical. In *Symposium (International) on Combustion*, volume 27, pages 1507–1514. Elsevier, 1998.

[107] SJ Brookes and JB Moss. Predictions of soot and thermal radiation properties in confined turbulent jet diffusion flames. *Combustion and Flame*, 116(4):486–503, 1999.

[108] Benedetta Franzelli, Eleonore Riber, Benedicte Cuenot, and Matthias Ihme. Numerical modeling of soot production in aeroengine combustors using large eddy simulations. In *ASME Turbo Expo 2015: Turbine Technical Conference and Exposition*, pages V04BT04A049–V04BT04A049. American Society of Mechanical Engineers, 2015.

[109] K. P. Geigle, R. Hadef, and W. Meier. Soot formation and flame characterization of an aero-engine model combustor burning ethylene at elevated pressure. *ASME J Eng Gas Turb Pwr*, 136(2):021505, 2014.

[110] K. P. Geigle, W. O'Loughlin, R. Hadef, and W. Meier. Visualization of soot inception in turbulent pressurized flames by simultaneous measurement of laser-induced fluorescence of polycyclic aromatic hydrocarbons and laser-induced incandescence, and correlation to oh distributions. *Applied Physics B*, 119(4):717–730, 2015.

[111] Franck Nicoud and Frédéric Ducros. Subgrid-scale stress modelling based on the square of the velocity gradient tensor. *Flow, turbulence and Combustion*, 62(3):183–200, 1999.

[112] Simone Paccati, Davide Bertini, Stefano Puggelli, Lorenzo Mazzei, Antonio Andreini, and Bruno Facchini. Numerical analyses of a high pressure sooting flame with multiphysics approach. *Energy Procedia*, 148:591–598, 2018.

[113] H. Wang and A. Laskin. A comprehensive kinetic model of ethylene and acetylene oxidation at high temperatures. *Progress Report for an AFOSR New World Vista Program*, 1998.

[114] Michael F Modest. *Radiative heat transfer*. Academic press, 2013.

[115] Stephen B Pope. Ten questions concerning the large-eddy simulation of turbulent flows. *New journal of Physics*, 6(1):35, 2004.

[116] Patrick Nau, Zhiyao Yin, Klaus Peter Geigle, and Wolfgang Meier. Wall temperature measurements at elevated pressures and high temperatures in sooting flames in a gas turbine model combustor. *Applied Physics B*, 123(12):279, 2017.

[117] S Berger, S Richard, F Duchaine, G Staffelbach, and LYM Gicquel. On the sensitivity of a helicopter combustor wall temperature to convective and radiative thermal loads. *Applied Thermal Engineering*, 103:1450–1459, 2016.

[118] ANSYS FLUENT. 17.0 udf manual. *ANSYS Inc.*, 2016.

[119] R Kent Dybvig. *The SCHEME programming language*. Mit Press, 2009.

[120] Tsan-Hsing Shih, William W Liou, Aamir Shabbir, Zhigang Yang, and Jiang Zhu. A new k-ϵ eddy viscosity model for high reynolds number turbulent flows. *Computers & Fluids*, 24(3):227–238, 1995.

[121] A. Andreini, R. Da Soghe, B. Facchini, L. Mazzei, S. Colantuoni, and F. Turrini. Local source based cfd modeling of effusion cooling holes: Validation and application to an actual combustor test case. *ASME J Gas Turb Pwr*, 136(1):011506, 2014.

[122] B.E. Launder and D.B. Spalding. The numerical computation of turbulent flows. *Computer Methods in Applied Mechanics and Engineering*, 3(2):269 – 289, 1974.

[123] B. Sirjean, E. Dames, D. A. Sheen, H. Wang, T. F. Lu, and T. F. Law. Jetsurf 1.0-ls: Simplified chemical kinetic models for high-temperature oxidation of C5 to C12 n-Alkanes. Technical report, http://melchior.usc.edu/JetSurF1.0/JetSurF1.0-ls, 2009.

[124] M. Rachner. Die Stoffeigenschaften von Kerosin Jet A-1. Technical report, DLR, Institut für Antriebstechnik, März 1998.

[125] Ansys Fluent Ansys. *17.0 Theory Guide*. 2016.

[126] S. B. Pope. Ten questions concerning the large-eddy simulation of turbulent flows. *New Journal of Physics*, 35, March 2004.

[127] P. Domingo, L. Vervisch, and J. Réveillon. DNS analysis of partially premixed combustion in spray and gaseous turbulent flame-bases stabilized in hot air. *Combustion and Flame*, 140(3):172–195, February 2005.

[128] E. Knudsen and H. Pitsch. Large-Eddy Simulation for Combustion Systems: Modeling Approaches for Partially Premixed Flows. *The Open Thermodynamics Journal*, 4(1):76–85, January 2010.